

The Pennsylvania State University

The Graduate School

Department of Materials Science and Engineering

**ROBUST ELECTRICAL CONTACTS FOR SENSORS
AND ELECTRONICS IN SPACE FLIGHT**

A Dissertation in

Materials Science and Engineering

by

Katherine Cora Kragh-Buetow

Submitted in Partial Fulfillment
of the Requirements
for the Degree of

Doctor of Philosophy

May 2016

The dissertation of Katherine Cora Kragh-Buetow was reviewed and approved* by the following:

Suzanne E. Mohny
Professor of Materials Science and Engineering and Electrical Engineering
Dissertation Advisor
Chair of Committee
Chair, Intercollege Graduate Degree Program in Materials Science and Engineering

Patrick M. Lenahan
Distinguished Professor of Engineering Science and Mechanics

Joan M. Redwing
Professor of Materials Science and Engineering, Chemical Engineering,
and Electrical Engineering
Associate Director, Materials Research Institute

Earle R. Ryba
Professor Emeritus of Metallurgy, Department of Materials Science and Engineering

Robert S. Okojie
Research Electronics Engineer, NASA Glenn Research Center
Special Member

*Signatures are on file in the Graduate School

ABSTRACT

The continued advancement of silicon-based electronics has transformed people's lives around the world. However, silicon is not best suited for all types of devices or all applications; thus, researchers will need to continue investigating and developing new materials, processing techniques, and devices. Silicon carbide (SiC) is a wide bandgap semiconductor of great interest for high-temperature and high-power devices. Developing ohmic contacts and diffusion barriers for SiC is critically important to achieving high-temperature electronics and sensors. On the other hand, indium nitride (InN) is a narrow bandgap semiconductor with promise for optoelectronics, including photovoltaics. Both SiC and InN are non-centrosymmetric crystal structures, resulting in polar {0001} faces. Polarity has been shown to influence various properties such as growth and etching without clear trend amongst all polar materials. The influence of polarity on metal–semiconductor interfaces must be understood for understanding and optimizing electrical contacts.

Ohmic contacts to *p*- and *n*-type 4H-SiC using alloyed tungsten–nickel (W:Ni) refractory thin films were investigated. Transfer length measurement test structures on *p*-type 4H-SiC ($N_A = 3 \times 10^{20} \text{ cm}^{-3}$) epitaxial layers revealed ohmic contacts with specific contact resistances, ρ_c , of $\sim 10^{-6}$ – $10^{-5} \text{ } \Omega\text{cm}^2$ after 0.5 h annealing in argon at temperatures of 1000 °C, 1100 °C, 1150 °C, and 1200 °C. Contacts fabricated on *n*-type 4H-SiC ($N_D = 2 \times 10^{19} \text{ cm}^{-3}$) by similar methods were shown to have similar specific contact resistance values after annealing at 1000–1150 °C. Together, these findings demonstrated simultaneous ohmic contact formation for W:Ni alloys on 4H-SiC. The lowest ρ_c values

were $(7.3 \pm 0.9) \times 10^{-6} \Omega\text{cm}^2$ for *p*-SiC and $(6.8 \pm 0.9) \times 10^{-6} \Omega\text{cm}^2$ for *n*-SiC after annealing at 1150 °C. X-ray diffraction showed a cubic tungsten–nickel–carbide phase in the ohmic contacts after annealing as well as tungsten carbide after annealing at the higher temperatures. Auger electron spectroscopy depth profiles revealed a relatively homogeneous contact after annealing at 1000 °C. In samples annealed at 1100 °C or higher, depth profiles suggested the presence of distinct metal carbide regions (with some dissolved Si) above a nickel- and silicon-rich region at the interface with SiC. X-ray energy dispersive spectroscopy mapping also showed phase segregation into tungsten-rich and nickel-rich regions after annealing at 1100 °C and above. Scanning electron microscopy of cross-sectioned W:Ni/SiC indicated the ρ_c values could be up to 20% lower for *p*-SiC and up to 10% lower for *n*-SiC based on the depth of reaction into the epilayers. W:Ni alloys have shown promise as simultaneous ohmic contacts to *p*- and *n*-SiC, offering low and comparable ρ_c values that surpass those of other simultaneous ohmic contacts.

Further aging of the ohmic contacts was explored for both 1000 °C+ and 600 °C. At the higher temperatures, significant degradation in ohmic contacts was seen for all temperatures after an additional 0.5 h at peak temperature except for 1000 °C. Thermal stability was also seen for 1000 °C out to 2 h for both contacts to *n*-SiC and contacts to more lightly-doped *p*-SiC ($N_A = 1 \times 10^{20} \text{ cm}^{-3}$) with higher ρ_c values. All samples annealed at 1000 °C for 1 h total were then aged for 100 h at 600 °C in Ar with only moderate increases in ρ_c for contacts to SiC with the highest doping, and small decreases in ρ_c for contacts to more lightly-doped *p*-SiC. Diffusion barriers of co-sputtered

platinum (Pt) and carbon (C) with tantalum disilicide (TaSi_2) were explored. While the ohmic contact layer was preserved for short times at 600 °C+ and 700 °C, no immediate benefit could be identified over previously reported Pt/ TaSi_2 barriers.

Metal–InN interfaces were characterized in a side-by-side study on the polar $\{0001\}$ faces. The Ni films on (0001) and (000 $\bar{1}$) InN exhibited different reaction kinetics upon annealing at 400 °C. Structural and chemical analysis using grazing incidence X-ray diffraction, transmission electron microscopy, and X-ray energy dispersive spectrometry indicated that an interfacial reaction did not occur between the Ni film and the In-face (0001) InN layer. However, the N-face InN reacted with Ni to form a Ni_3InN_x ternary phase with an anti-perovskite structure. The Ni contacts on the In-face remained unreacted over 4 h of annealing at 400 °C while the Ni continued to react on the N-face. This same behavior was seen after 1 h annealing at 400 °C; however, oxidation of the InN and Ni became increasingly problematic. The difference in reactivity for Ni on In-face and N-face InN indicated that polarity altered the reaction and may also affect other metal–polar semiconductor interfaces.

TABLE OF CONTENTS

List of Figures	viii
List of Tables	xv
Acknowledgements	xvi
Chapter 1 Introduction	1
1.1 Motivation.....	1
1.2 Metal–Semiconductor Theory	5
1.2.1 Semiconductors	5
1.2.2 Metal–semiconductor contacts	7
1.3 Materials of Interest	11
1.3.1 Silicon Carbide	11
1.3.2 Indium Nitride	15
Chapter 2 Methods and Techniques.....	18
2.1 Sample Fabrication Techniques.....	18
2.1.1 Physical vapor deposition.....	18
2.1.2 Preparation of Indium Nitride samples.....	20
2.1.3 Preparation of Silicon Carbide samples	22
2.1.4 Annealing	30
2.2 Electrical Characterization.....	31
2.2.1 Transfer length measurement structure	32
2.2.2 Specific contact resistance extraction.....	35
2.3 Materials Characterization Techniques	37
2.3.1 X-ray diffraction	37
2.3.2 Electron microscopy	45
2.3.3 Auger electron spectroscopy	51
Chapter 3 Formation and Aging of Tungsten–Nickel Ohmic Contacts to Silicon Carbide.....	56
3.1 Literature on SiC Ohmic Contacts.....	57
3.1.1 Background on ohmic contacts to SiC	57
3.1.2 Selected review of distinct ohmic contacts to <i>n</i> -type and <i>p</i> -type SiC ..	59
3.1.3 Review of simultaneous ohmic contacts to SiC	65
3.1.4 Review of W–Ni thin films in electronics	68
3.2 Tungsten–Nickel Simultaneous Ohmic Contacts to 4H-SiC.....	70
3.2.1 Experimental procedures for contacts to <i>p</i> - and <i>n</i> -SiC.....	70
3.2.2 Electrical characterization results and discussion	74

3.2.3 Materials characterization results and discussion.....	80
3.3 Literature on Aging and Diffusion Barriers for SiC.....	101
3.4 Aging and Diffusion Barriers for W:Ni/4H-SiC	105
3.4.1 Aging of W:Ni contacts.....	106
3.4.2 Addition of Carbon in diffusion layers.....	114
3.5 Conclusions.....	120
Chapter 4 Nickel Contacts to Polar Indium Nitride.....	123
4.1 Semiconductor Polarity in the Literature.....	123
4.2 Experimental Procedures for InN	127
4.3 Ni/InN Results and Discussion.....	129
4.4 Conclusions.....	139
Chapter 5 Summary and Future Work	140
5.1 Summary.....	140
5.2 Future Work.....	145
5.2.1 Future work for contacts to Silicon Carbide.....	145
5.2.2 Future work for polar semiconductors	147
References.....	149

LIST OF FIGURES

Figure 1–1. An electron can be elevated from the valence band to the conduction band of a semiconductor, leaving behind a hole in the valence band. <i>Adapted from [14], [20].</i>	6
Figure 1–2. Energy band models with Fermi-levels and work functions for (a) a metal, (b) an <i>n</i> -type semiconductor, and (c) a <i>p</i> -type semiconductor. <i>Adapted from [14], [20].</i>	8
Figure 1–3. Energy band models for Schottky barriers formed with a metal and (a) an <i>n</i> -type semiconductor as well as (b) a <i>p</i> -type semiconductor from the energy band conditions presented in Figure 1–2. <i>Adapted from [14], [20].</i>	9
Figure 1–4. Three methods of conduction exist in ohmic contacts with increasing doping from (a) thermionic emission to (b) thermionic field emission to (c) field emission. <i>Adapted from [14].</i>	10
Figure 1–5. The most common SiC polytypes are (a) 3C, (b) 4H, and (c) 6H. The larger circles are Si atoms, and the smaller circles are C atoms. <i>Made in PowderCell [22].</i>	12
Figure 1–6. The hexagonal structure of InN. The larger circles are In atoms, and the smaller circles are N atoms. <i>Made in PowderCell [22].</i>	15
Figure 1–7. The polar faces of InN, as seen from a (1210) projection. The larger circles are In atoms, and the smaller circles are N atoms. <i>Made in PowderCell [22].</i>	17
Figure 2–1. (a) The interior of the e-beam evaporation system for evaporating metals from the crucibles at the bottom to the samples on top (behind the shutter). (b) The interior of the sputtering system for depositing metals from the targets up top (behind the shutters) to the sample stage below.	22
Figure 2–2. A Materials Research Corporation 6-in sputtering system was used for depositing sacrificial Al films.	23
Figure 2–3. A Karl Süss MJB3 Aligner was used for patterning and exposing photoresist.	24
Figure 2–4. (a) A H ₃ PO ₄ solution in a water bath was heated on a hot plate for wet etching the Al layers. The RIE chamber (b) exterior and (c) interior was used for directional dry etching of SiC and the metal layers.	25

- Figure 2–5.** (a) A Teflon sample basket in a beaker of 1:1 piranha solution on top of a Petri dish. (b) A Teflon sample basket in a beaker of 2:1 aqua regia on top of a Petri dish. 26
- Figure 2–6.** The two-chamber sputtering system was used for depositing Si/W:Ni layers in the left hand chamber, and sputtering Ti as an oxygen getter in the right hand chamber. 28
- Figure 2–7.** (a) The three-stage tube furnace was used for ohmic contact formation on SiC, and (b) the tube furnace with the gettering furnace (on left) was used for aging InN and SiC samples. 30
- Figure 2–8.** The AS-One rapid thermal annealing system with heating lamps above the carrier wafer was used in the diffusion barrier study. 31
- Figure 2–9.** The TLM structures consisted of six contacts on top of a raised mesa. Dimensions are marked with their labels: mesa width (W), contact width (Z), contact length (L), and gap spacings (d). *Adapted from* [14]. 33
- Figure 2–10.** (a) The ideal configuration of four probes for current–voltage measurements in order to extract the specific contact resistance values. Current–voltage measurements to W50:Ni50/ n -SiC were (b) nonlinear as-deposited and (c) ohmic after annealing at 1150 °C. 34
- Figure 2–11.** The schematic model of a TLM fit for R_T vs. d as shown in Eqs. 2–2 and 2–3. *Adapted from* [14]. 35
- Figure 2–12.** A visual depiction of Bragg’s law: Crystal planes parallel to the surface are spaced at d_{hkl} and have a surface normal bisecting the X-ray path (shown as the dash-dot red vector). X-rays incident (1 and 2) at the Bragg angle θ are diffracted (1' and 2') from these crystal planes at the same angle θ . The path difference between the X-rays is the line of square dots, equal to $2d\sin(\theta)$. *Adapted From* [36], [37]. 39
- Figure 2–13.** Visual depiction of the θ – 2θ symmetry of the incident and diffracted X-rays. *Adapted from* [36]. 39
- Figure 2–14.** The PANalytical X’Pert Pro MPD θ – θ system can be used in (a) Bragg–Brentano configuration and (b) grazing incidence configuration (GIXRD). 41
- Figure 2–15.** GIXRD orientation: The incident X-ray enters at a fixed angle ω , and diffracted X-rays from off-axis planes are detected at their 2θ angles. The red dot-dash vectors represent the plane normals, which are bisectors of the incident and diffracted beams. *Adapted from* [39]. 42

- Figure 2–16.** (a) The Rigaku DMAX-Rapid II microdiffractometer is shown with schematics of (b) the angle configurations relative to the area detector and (c) the Cartesian/polar coordinates of the detector. *(b) and (c) adapted from [40].* ..44
- Figure 2–17.** (a) The exterior of the FEI NanoSEM 630 used for imaging with the X-ray energy dispersive spectroscopy attachment on the far left; and (b) the interior of the same.46
- Figure 2–18.** Emission of a $K\alpha$ X-ray for XEDS: After the K electron is displaced, the L_2 electron replaces the K electron, leaving the energy difference for the emission of a $K\alpha$ X-ray. *Adapted from [14].*48
- Figure 2–19.** The JEOL 2010F TEM was used for examining InN samples. *Used with permission from Debangshu Mukherjee.*50
- Figure 2–20.** Emission of a KLL Auger electron: After the K electron is displaced, the L_2 electron replaces the K electron, leaving the energy difference for the emission of the Auger electron. *Adapted from [14].*52
- Figure 2–21.** (a) The PHI 660 scanning Auger microprobe used for AES analysis along with (b) the sunburst sample holder which must ground the area of interest (inset).53
- Figure 2–22.** Differentiated AES scans of the C (KLL) peak show the distinct peak shapes that reflect the difference in bonding between (a) a metal carbide and (b) non-carbide C.54
- Figure 3–1.** Specific contact resistance (ρ_c) values for simultaneous ohmic contacts from the literature plotted against the dopant concentrations in the SiC epilayers. Open symbols are ohmic contacts to n -SiC and filled symbols are ohmic contacts to p -SiC.68
- Figure 3–2.** The resistances were plotted vs. gap spacing with a high goodness of fit (R^2) in order to obtain the ρ_c value, as shown for W50:Ni50/ n -SiC.73
- Figure 3–3.** Specific contact resistance as a function of annealing temperature for W:Ni contacts on p -SiC with $N_A = 3 \times 10^{20} \text{ cm}^{-3}$ and n -SiC with $N_D = 2 \times 10^{19} \text{ cm}^{-3}$. The boxplot shown has the averages marked with plus signs.77
- Figure 3–4.** Simultaneous ohmic contact ρ_c values plotted against the dopant concentrations in the SiC epilayers. Values from W51:Ni49 samples annealed at 1150 °C and W50:Ni50 samples annealed at 1100 °C have been added to Figure 3–1, showing their similar ρ_c values for both conductivity types. The open symbols are ohmic contacts to n -SiC and the filled symbols are ohmic contacts to p -SiC.79

- Figure 3–5.** Microdiffractometer XRD plot for W/*p*-SiC annealed for 0.5 h at 1200 °C, showing W₅Si₃ and W₂C along with SiC and residual W. 81
- Figure 3–6.** Microdiffractometer XRD plot for W90:Ni10/*p*-SiC annealed for 0.5 h at 1000 °C, showing the presence of W_xNi_yC in addition to W₅Si₃ and W₂C. 82
- Figure 3–7.** The crystal structures for the two cubic tungsten–nickel–carbide phases: (a) W₄Ni₂C (*cF112*) and (b) W₆Ni₆C (*cF104*). The larger light blue circles are Ni (including corners), the larger darker teal circles are W, and the smaller black circles are C. *Made in PowderCell* [22]. 83
- Figure 3–8.** Calculated XRD plot demonstrating the similarity in structure of the two possible compositions for W_xNi_yC: W₄Ni₂C (*cF112*) and W₆Ni₆C (*cF104*). The peak locations (but not intensities) are horizontal displacements due to the difference in lattice parameters. *Made in PowderCell* [22]. 84
- Figure 3–9.** Microdiffractometer XRD plot for W50:Ni50/*p*-SiC annealed for 0.5 h at 1100 °C showing W_xNi_yC. 85
- Figure 3–10.** Microdiffractometer XRD plot for W51:Ni49/*p*-SiC annealed for 0.5 h at 1150 °C showing W_xNi_yC, WC, and SiC. 86
- Figure 3–11.** Binary W–Ni phase diagram with three intermetallic phases. Reprinted with permission from ASM International [130], all rights reserved, www.asminternational.org. 87
- Figure 3–12.** The W–Ni–C ternary phase diagram at 1200 °C (but typical also of 1300 °C [140]) showing three ternary carbides. Reprinted with permission from ASM International [138], all rights reserved, www.asminternational.org. 88
- Figure 3–13.** SEM image of lath- and plate-like surface morphology for W51:Ni49/*p*-SiC annealed at 1200 °C with XEDS maps showing complementary Ni- and W-rich regions. 89
- Figure 3–14.** SEM image of solely lath-like surface morphology for W50:Ni50/*p*-SiC annealed at 1200 °C with XEDS maps showing complementary Ni- and W-rich regions. 90
- Figure 3–15.** AFM of W51:Ni49/*p*-type SiC annealed at 1200 °C revealed (a) the surface topography map and (b) the map of peak current with the brighter regions being the conductive regions. 92

- Figure 3–16.** AFM of W51:Ni49/*n*-type SiC annealed at 1100 °C revealed (a) the surface topography map and (b) the map of peak current with the brighter regions being the conductive regions. 93
- Figure 3–17.** AES depth profile for as-deposited W51:Ni49/*n*-SiC. The W:Ni ratios are in agreement with the discussed film composition of W57:Ni43 but the atomic concentrations differ due to the included signal noise from C, O, and Si. 94
- Figure 3–18.** AES depth profile for as-deposited W50:Ni50/*n*-SiC. The W:Ni ratios are in agreement with the discussed film composition of W52:Ni48 but the atomic concentrations differ due to the included signal noise from C, O, and Si. 94
- Figure 3–19.** AES depth profile for W51:Ni49/*p*-SiC annealed at 1150 °C through a plate-like region, showing a tungsten carbide region over a Ni+Si region. 95
- Figure 3–20.** AES depth profile for W51:Ni49/*p*-SiC annealed at 1150 °C through a field-like region showing a metal carbide region above a Ni+Si region. 96
- Figure 3–21.** SEM images of W51:Ni49/SiC showing the surfaces with fewer features after annealing at 1000 °C. 97
- Figure 3–22.** AES depth profile for W51:Ni49/*p*-SiC annealed at 1000 °C showing a metal carbide region above the SiC epilayer. 98
- Figure 3–23.** Representation of the spatial arrangement of Si/W51:Ni49/SiC before and after annealing. The phases are shown in their relative locations but not to scale. 99
- Figure 3–24.** AES depth profile for W50:Ni50/*p*-SiC annealed at 1000 °C showing a metal carbide region with an increase in Ni adjacent to the SiC substrate. 100
- Figure 3–25.** SEM image of a polished cross-section for W50:Ni50 reacted with *p*-SiC after annealing at 1100 °C, showing the reaction depth into the mesa. 101
- Figure 3–26.** Specific contact resistances for W:Ni contacts on *p*-SiC with $N_A = 3 \times 10^{20} \text{ cm}^{-3}$ and *n*-SiC with $N_D = 2 \times 10^{19} \text{ cm}^{-3}$ after 1 h total annealing at 1000 °C. The boxplot shown has the averages marked with plus signs. 108
- Figure 3–27.** Specific contact resistances for W:Ni contacts on *p*-SiC with $N_A = 1 \times 10^{20} \text{ cm}^{-3}$ after 0.5 h total annealing at 1000–1150 °C, with similar trends

but a different scale from the matched pairs. The boxplot shown has the averages marked with plus signs.	109
Figure 3–28. Specific contact resistances for W:Ni contacts on (a) <i>n</i> -SiC with $N_D = 2 \times 10^{19} \text{ cm}^{-3}$ and (b) <i>p</i> -SiC with $N_A = 1 \times 10^{20} \text{ cm}^{-3}$ out to 2 h total annealing at 1000 °C. The boxplot shown has the averages marked with plus signs. Note: The plots in (a) and (b) have different scales.	111
Figure 3–29. Specific contact resistances for W:Ni contacts on <i>p</i> -SiC with $N_A = 3 \times 10^{20} \text{ cm}^{-3}$ and <i>n</i> -SiC with $N_D = 2 \times 10^{19} \text{ cm}^{-3}$ after 1 h total annealing at 1000 °C and then 100 h at 600 °C. The boxplot shown has the averages marked with plus signs.	113
Figure 3–30. Specific contact resistances for W:Ni contacts on <i>p</i> -SiC with $N_A = 1 \times 10^{20} \text{ cm}^{-3}$ after 1 h total annealing at 1000 °C and then 100 h at 600 °C. The boxplot shown has the averages marked with plus signs.	114
Figure 3–31. Representation of the hypothesized change in diffusion barrier structure after annealing. The C in the co-sputtered Pt+C layer would segregate to the surface and form graphene.	115
Figure 3–32. AES depth profile for the as-deposited PtC 9 layer on TaSi ₂	117
Figure 3–33. AES depth profile for PtC 9 layer/TaSi ₂ /Si/W:Ni/SiC annealed at 900 °C in the RTA for 300 s under Ar. PtSi _x has formed along with TaC _x above the region dominated by TaSi ₂ . The TaC _x has nearly replaced the Pt as the upper layer. The Si/W:Ni contact had been previous annealed at 1150 °C...	118
Figure 3–34. AES depth profile for PtC 9 layer/TaSi ₂ /Si/W:Ni/SiC annealed in the RTA for 1 h at 600 °C under Ar. PtSi _x has formed above the stable TaSi ₂ . The Si/W:Ni contact had been previous annealed at 1150 °C.....	119
Figure 4–1. Representation of the distinct material layers involved in the polar face study: Ni deposited on InN films that were grown on GaN layers of the same polarity.....	128
Figure 4–2. TEM bright-field images of Ni films on (a) In-face and (b) N-face InN with SAD of (c) In-face and (d) N-face InN for as-deposited samples. Each diffraction pattern consists of a set of diffraction spots from the single crystalline InN and diffraction rings from the polycrystalline Ni film.....	130
Figure 4–3. GIXRD plots collected from (a) In-face Ni/InN samples and (b) N-face Ni/InN samples both as-deposited and after 1 h at 400 °C.	131

- Figure 4–4.** The anti-perovskite structure of the nickel–indium–nitride ($\text{Ni}_3\text{InN}_{0.5}$) ternary phase. Green circles at the corners are In atoms, light blue circles are Ni atoms, and the smaller blue circle is a N atom. *Made in PowderCell* [22]. ... 132
- Figure 4–5.** TEM bright-field images of Ni films annealed at 400 °C for 1 h on (a) In-face and (b) N-face InN along with SAD of the (c) In-face and (d) N-face InN samples. Diffraction spots are from InN, and rings are from the Ni-bearing layers. 133
- Figure 4–6.** HAADF images for Ni films annealed for 1 h at 400 °C on (a) In-face and (b) N-face InN highlight the difference in microstructure. 134
- Figure 4–7.** HAADF images for (a) In-face and (c) N-face, with site-specific XEDS line profiles through (b) Ni/InN and (d) $\text{Ni}_3\text{InN}_x/\text{InN}$ on the respective images. Lastly, (e) the XEDS spectra from the annealed Ni films reveal only a Ni peak for the In-face sample while N and In peaks are also observed for the N-face sample. 135
- Figure 4–8.** GIXRD plot of Ni on (0001) InN annealed at 350 °C and 375 °C for 1 h in N_2 , revealing a reaction phase between the Ni and InN beginning at the higher temperature. 136
- Figure 4–9.** GIXRD plots of Ni on {0001} InN annealed (a) at 400 °C for 4 h in N_2 , and (b) 450 °C for 1 h in N_2 , revealing that In_2O_3 and NiO were among the phases formed. 137
- Figure 4–10.** HAADF images for (a) In-face and (d) N-face InN annealed at 450 °C, with site-specific XEDS line profiles through (b) Ni–In–O and (e) Ni–In–N–O on the respective images. The estimated compositions from the XEDS are seen in (c) and (f), respectively; however, the N is overstated in the films and the O overstated in the InN. 138

LIST OF TABLES

Table 1–1. Properties of Si and SiC. All Si properties from [7].	13
Table 2–1. Nominal dimensions of the TLM gap spacings for constant width of $Z = 100 \mu\text{m}$	33
Table 3–1. Variables considered in the W:Ni TLM structures on p -type 4H-SiC.	71
Table 3–2. Target and film compositions of the W:Ni alloys.	72
Table 3–3. Average specific contact resistance $\rho_c \pm$ standard error (σ/\sqrt{N}) in Ωcm^2 . Annealing time was 0.5 h in Ar. Shaded conditions show comparable values.	77
Table 3–4. Summary of phases identified from XRD. Shaded boxes are ohmic conditions.	81
Table 3–5. Average specific contact resistance $\rho_c \pm$ standard error (σ/\sqrt{N}) in Ωcm^2 after aging in Ar. Shaded conditions had minimal changes between 1 st and 2 nd anneals.	107
Table 3–6. Average specific contact resistance $\rho_c \pm$ standard error (σ/\sqrt{N}) in Ωcm^2 for $N_A = 1 \times 10^{20} \text{ cm}^{-3}$. Total annealing time was 0.5 h in Ar.	109
Table 3–7. Average specific contact resistance $\rho_c \pm$ standard error (σ/\sqrt{N}) in Ωcm^2 for $N_A = 1 \times 10^{20} \text{ cm}^{-3}$. Total annealing time was 1 h in Ar.	110
Table 3–8. Average specific contact resistance $\rho_c \pm$ standard error (σ/\sqrt{N}) in Ωcm^2 . Total annealing time was 2 h in Ar at 1000 °C.	111
Table 3–9. Average specific contact resistance $\rho_c \pm$ standard error (σ/\sqrt{N}) in Ωcm^2 . Total annealing time was 1 h at 1000 °C before 100 h of aging at 600 °C in Ar.	112
Table 3–10. Sputtering rates and thicknesses for the 9 layers of Pt+C and C. Layers are ordered from air down to TaSi ₂	117

ACKNOWLEDGEMENTS

I must start with thanking my many teachers and professors over the years who believed that I had a bright academic future. Special gratitude goes out to Mr. Brabeck, Mr. Cleland, Mrs. Garfield, Mr. Lowe, Mr. Mathers, Mr. Pausback, Mr. Pape, Mr. Riley, and Mr. Tucker for their parts in making sure I ended up (1) in college, (2) picking a challenging technical major, and (3) prepared for anything. I am also immensely grateful to numerous professors at Rose-Hulman for sharing their knowledge and passions while expecting everything. I thank Prof. D. Miller for a freshman summer internship where my biggest lesson was to change my major. Prof. Ditteon, Prof. Bunch, Prof. Granieri, Prof. Moloney, and the Profs. Kirkpatrick are thanked for helping to instill my love of research and for numbering amongst my bigger champions to attend graduate school.

I thank my advisor, Prof. Suzanne Mohny, for providing an excellent REU experience and then being willing to accept me back as a graduate student at Penn State (PSU). Without your tutelage and support, I could not have grown as a scholar-engineer and interdisciplinary scientist. I am grateful to the University Graduate Fellowship fund and the 3M fellowship program. My career is indebted to Prof. Mohny, however, for discovering the NASA Space Technology Research Fellows (NSTRF) program. I have thoroughly enjoyed my experience as part of the inaugural NSTRF class (NASA Grant #NNX11AN03H) and am incredibly appreciative of the numerous opportunities I have cherished on-site at NASA Glenn Research Center (GRC). I am grateful to Dr. Robert Okojie for being my NASA mentor, and challenging me the entire time. Thank you to my dissertation committee for supporting my research along the way.

Both PSU and NASA GRC have great people working there, and I am extremely appreciative for all the advice, training, and friendship from the personnel of both locations, even though I cannot name everyone. Thank you to Prof. Ryba, Dorothy Lukco, and Nichole Wonderling for their assistance with my writing. My enumerated thanks is shared with PSU MRI members Bangzhi, Beth J., Chad, David, Dustin, Gino, Josh M., Julie, Maria, Nichole, Tim K., Tim T., Trevor, and Xiaojun. At NASA GRC, my enumerated thanks is shared with Ariana, Azlin, Andy W., Beth, Carl, Chuck, José,

Jim, Kelley, Kimala, Michelle, Mike, Phil, Roger, and Terry for making me feel like I belonged in the cleanroom. Thank you to Dorothy for sharing your vast knowledge and allowing me to operate your equipment. A myriad of thanks to David Spry for all your advice and assistance, and being the best office-mate/colleague an intern could ever have.

I extend my infinite gratitude to members of the Mohny group, past and present, including Amber, Anna, Bob, Brian, Brittany, Carolyn, Haila, Josh Y., Joyce, Kalissa, Shih-Ying, Tim W., and Won. Special appreciation to Michael Abraham for being my timeline peer; I would have never made it this far without you. I have been blessed to know many students and personnel in (and outside of) the department. Let this be my enumerated acknowledgements of the wonderful maintenance and support staff; Carl Morandi and Jason Britson for sharing the journey; and the Datta, Randall, Redwing, and Trolier-McKinstry groups for being (late-night) lab-buddies. I thank all the undergraduates I have had the opportunity to mentor, especially Jimmy and Frances. Thank you to Ayo, Bruce, Jillian, Ramya, and Yitian for also accepting my advice.

My appreciation abounds for Garrett, Jessica, Adam, and Beth as friends in my State College world and for reminding me how much I have to learn. Thank you to the Boumas, Potalas, Turpins, Schuhs, Scarboroughs, and Whalen-Parsons for sharing the joys of life outside of academia. I will always cherish the Blues for sharing the reminders of home as my in-town family. I am grateful for other intermittent reminders of life outside the lab: the NASA prayer group, the PSU Catholic Campus Ministry, NASA lunchtime cards in 77, NASA GeT-GO, NASA Frisbee, PSU CAPS, PSU White Course community, the PSU Art Centers (CPA/CFAC), and my myriad experiences in the Penn State graduate student government. Thank you to Eliot and Azzy for your friendship, even in some of my hardest moments. Thank you to my friends from high school and college who can hopefully forgive my absentee time in the academic bubble.

Lastly, thank you to my many family members from all sides, especially my grandparents, parents, Aunt Debbie, and my sister who have supported my nomadic lifestyle as I pursue my education. Above all else, I express my extreme gratitude to my husband for supporting my dreams as his own and embodying the noblest form of love in enabling my graduate school journey. Chris, I dedicate this work to you.

Ad astra per aspera

Ad Majorem Dei Gloriam

Chapter 1

Introduction

This chapter serves to describe the motivation, theory, and materials studied in this work. The aim is to provide sufficient background to understand the chapters that follow.

1.1 Motivation

Since before the written word, humans have desired to share information and to improve their lives. In the 19th and 20th centuries, electricity transformed from a research curiosity to become a ubiquitous part of everyday life in the Western world. Electronics for research, military, and even the consumer resulted in a multitude of technological developments. With the invention of the transistor in 1947, however, the age of modern microelectronics started to take root in the Western world. The creation of metal oxide semiconductor field effect transistors (MOSFETs) and their use in integrated circuits (ICs) started the continued advancement of computer chip performance all the way into the 21st century: Moore's Law. The saying 'Moore's Law' came out of a 1965 paper [1] by the co-founder of Intel acknowledging the number of transistors on a chip was doubling every year and would likely continue. Gordon Moore further predicted that scaling would bring about home computers, and personal electronics for the masses [1]. The rate of scaling has been revised to a doubling of chip density every two years,

leading to transistors-per-chip numbering in the multi-billions today. This sustained advancement in computing power has placed personal electronics and computing power into the hands of billions. The valued devices have shifted over time, with home desktop computers and portable tape/CD players giving way to laptops, cell phones, mp3 players, tablets, and wearable computers. Sharing information has never been easier with the rise of computers and the internet; and many cherish the improvement in their professional and personal lives. These advances have been possible because semiconductor electronics researchers and manufacturers have taken Moore's Law as their mantra—smaller electronic devices, higher power density, faster computing power, and cheaper by the (mass-produced) billions.

For decades, the continued development of IC technology relied heavily on silicon-based electronics. Along the way, the danger of discontinuing Moore's law has stimulated study and development of such technologies as silicon-on-insulator (SOI), high- k dielectrics, and nonplanar transistors (e.g., FinFETs). In the same time frame, other semiconductor materials have been researched and utilized for specialized areas such as light-emitting diodes (LEDs), lasers, and photovoltaics. The continued advancement of semiconductor technology will require further development in both new semiconductor materials and novel usage of already studied materials.

One of the many sectors stimulating the development of new materials is spaceflight. Expanding exploration remains the collective dream of both government agencies such as NASA as well as private enterprises around the world. As spacecraft operation lifetimes and distances from earth increase, an area of increased demand is sensors and controls. Specifically, real-time sensor feedback at elevated temperatures has

particular interest for monitoring onboard power generation, launch, and reentry systems—with heightened necessity for high-temperature destinations such as Venus. Previous lander spacecraft to Venus have survived less than two hours, in part due to the average surface temperature of 460 °C [2]. The interest in high-temperature electronics extends beyond spaceflight, including the automotive, aeronautics, and terrestrial power generation sectors. Monitoring turbine engines, propulsion systems, and geothermal drilling calls for dependable, high-temperature electronics up to 600 °C [3], [4]. Meanwhile, future-looking hypersonic flight even has interest in sensor operation at 1000 °C for short durations [5]. Yet, silicon and SOI technologies can only operate up to 200–250 °C [3], [4], [6]. In order to achieve high-temperature operation, semiconductor research has focused on replacements to silicon using wide bandgap semiconductors such as silicon carbide (SiC). SiC sensors could detect many properties including pressure, temperature, and the presence of gases [7], [8] with the additional benefit of SiC being a radiation-resistant material well-equipped for high temperatures. High-temperature, radiation-resistant SiC ICs would also be needed to communicate between sensors and the spacecraft. Before SiC can become more widely adopted in high-temperature devices, microfabrication and packaging techniques must be developed further [3], [8]. Electrical contact materials for metallization and diffusion barriers at elevated temperatures must also be improved for reliable device operation.

Ohmic contacts are essential for delivering electrical signals with minimal energy loss; consequently, numerous research efforts have investigated metal contacts to both *n*-type and *p*-type SiC [9]–[13]. The optimum ohmic contact material will have a low contact resistance for a long period of operation, representing ease of carrier transport

over a small barrier or through a thin barrier [13], [14]. Research into contacts to *n*-type SiC has generally resulted in lower specific contact resistance values than those from *p*-type SiC [9], [10], [13]. While long-term thermal stability of ohmic contacts to *n*-type SiC has shown promising results, even in air [15]–[18], ohmic contacts to *p*-type SiC have not been as successful. As ohmic contacts to both *n*-type and *p*-type SiC are required for many SiC devices, research has turned more attention to reliable ohmic contacts to *p*-type SiC.

In this dissertation, ohmic contacts to SiC have been investigated using tungsten–nickel (W:Ni) alloys. After focusing on the ohmic contact formation to *p*-type SiC, these alloys have also been studied on *n*-type SiC. Simultaneous ohmic contacts to both conductivity types of SiC using the same material and processing steps are desired for fabrication simplicity and reliability. As a non-centrosymmetric, hexagonal form of SiC was studied, the anisotropic structure exhibits polarity along the *c*-axis. Lattice polarity has been shown to have a strong influence on various aspects of semiconductors in terms of stability and performance. The availability, however, of 4H-SiC epilayers oriented along the less-studied C-face continues to be limited. Thus, a study of polar metal–semiconductor interfaces for indium nitride (InN) will be presented instead in this dissertation. As another material whose performance does not suffer with radiation exposure [19], InN has great promise for both solar cells and gas sensors in space.

From personal electronics to high-temperature sensors, the world demand for advancement is a question of when, not if. Materials such as SiC and properties such as polarity are part of the many directions for research opportunities. Electronics have

become an indispensable way of life for most; and the future of research and development certainly must deliver on some of these expectations.

1.2 Metal–Semiconductor Theory

1.2.1 Semiconductors

As already stated, semiconductors are the basis of modern electronics. When many atoms bond together, the electron orbital energy levels join together into energy bands. The energy band structure is material specific, with generalizations based on material type. Metals have overlapping energy bands that allow free movement of the ‘seas’ of electrons. Insulators have a large range of forbidden energy states—the bandgap (E_g)—between the lower, filled valence band (E_v) and the upper, empty conduction band (E_c) [20]. Bandgaps in semiconductors have smaller, finite values in the few (< 5) eV range. Incident photons or thermal energy can enable sufficiently excited electrons to surmount the bandgap into the conduction band. When electrons are boosted into the conduction band, they leave behind positive carriers (‘holes’) in the valence band, as seen in Figure 1–1. With the band structure in mind, semiconductors have conductivity (and resistance) in between those of metals and insulators. The energy of semiconductor bands is often plotted against momentum wave vectors in reciprocal space [20]. Direct bandgap semiconductors have their conduction band minima and valence band maxima aligned at the same momentum vector. Thus, recombination of electron–hole pairs or absorption of a photon occurs without a change in momentum. These

semiconductors have promising uses for optical applications. Indirect bandgap semiconductors do not have the minima/maxima aligned; thus, electrons must undergo simultaneous momentum and energy shifts, reducing the efficiency of this transition.

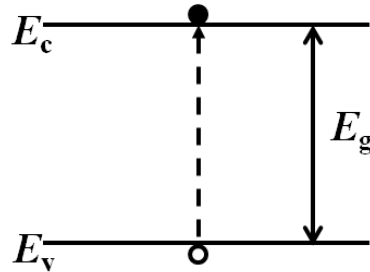


Figure 1–1. An electron can be elevated from the valence band to the conduction band of a semiconductor, leaving behind a hole in the valence band. *Adapted from* [14], [20].

Intrinsic semiconductors have electrons and holes in equal numbers. Additional charge carriers can be introduced into semiconductors by doping. Dopant atoms substitute into the existing semiconductor structure without the same number of valence electrons as the atoms in the structure. If a dopant material adds electrons (n), the ionized donor atoms (N_D) make the n -type semiconductor overall electrically neutral; and negative charge carriers are found in the conduction band. In kind, ionized acceptor atoms (N_A) capture electrons and create a p -type semiconductor with positive holes (p) in the valence band. Between the ionized atoms and the charge carriers, charge neutrality remains. A way to quantify the charge carriers in semiconductors involves the Fermi energy (E_F). The E_F level is defined from Fermi–Dirac statistics as the energy above which the energy levels are most likely empty and below which they are most likely filled. The probability of an electron existing at E_F is $\frac{1}{2}$ [20]. The extrinsic charge

carriers from dopants often dominate any intrinsic carriers except at high temperatures. The number of carriers along with temperature has important impacts on mobility (μ)—a measure of how quickly charge carriers move [20]. Semiconductor resistivity (ρ) depends on the mobility and the number of charge carriers for both electrons and holes, as seen in Eq. 1–1, where q is the fundamental charge.

$$\rho = (qn\mu_n + qp\mu_p)^{-1} \quad (1-1)$$

1.2.2 Metal–semiconductor contacts

Electrical contacts are required for all electronic and optoelectronic devices. They can be understood by considering what happens at metal–semiconductor interfaces. The physical conjoining of two materials involves the rearrangement of charge carriers, which can be understood by referring to the energy bands of the material. The metal work function (Φ_M) is the energy required for an electron to escape from E_F into vacuum (E_{vac}), as seen in Figure 1–2(a). Similarly, the definition is the same for the semiconductor work function (Φ_S). The electron affinity (χ_s) between E_c and vacuum now also adds to any energy above E_F inside E_g , ($E_c - E_F$), in determining Φ_S . As seen in Figure 1–2(b) and (c), a p -type semiconductor has a much larger Φ_S than an n -type semiconductor.

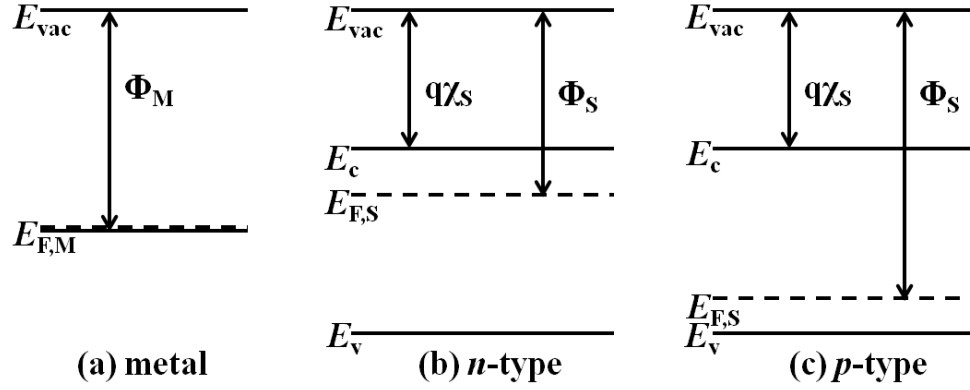


Figure 1–2. Energy band models with Fermi-levels and work functions for (a) a metal, (b) an n -type semiconductor, and (c) a p -type semiconductor. *Adapted from [14], [20].*

When two materials are brought into physical contact, their Fermi-levels must be aligned and continuous in equilibrium. The remaining energy bands will shift and bend in order to keep E_F constant. This creates a barrier between the metal and semiconductor for charge carriers. The Schottky barrier (Φ_B) inhibits electron transfer from an n -type semiconductor ($\Phi_M > \Phi_S$) and hole transfer from a p -type semiconductor ($\Phi_M < \Phi_S$), as seen in Figure 1–3(a) and (b), respectively. For the relative work function relationships opposite to those mentioned, the barrier curves down towards E_F , encouraging carrier flow. The region within the curved bands has a built-in voltage (V_{bi}) and electric field from the band bending, leaving the ionized dopants without any mobile charge carriers in this region.

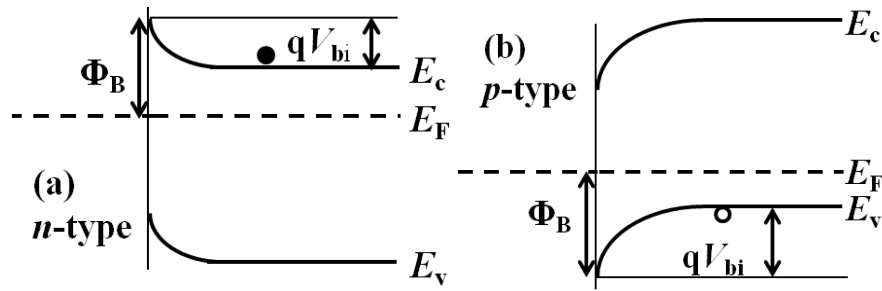


Figure 1–3. Energy band models for Schottky barriers formed with a metal and (a) an n -type semiconductor as well as (b) a p -type semiconductor from the energy band conditions presented in Figure 1–2. *Adapted from* [14], [20].

Charge carriers can pass over the Schottky barrier when they have enough kinetic energy to do so. An applied voltage that diminishes the barrier eases the passage of charge carriers, but an opposite bias would inhibit charge carriers with the enhanced barrier [20]. This kind of metal–semiconductor interface is described as a rectifying Schottky contact. Metal–semiconductor interfaces can also form ohmic contacts, where charge carriers move easily independent of the bias direction. Remembering current (I) as the movement of charge carriers, ohmic contacts obey linear I – V relationships. The creation of ohmic contacts can come about from several band alignments. Ohmic contacts exist when no barrier exists at the metal–semiconductor interface. Similarly, if the barrier is small enough and/or the electrons have sufficient energy to be transported over the barrier, thermionic emission (TE) results in an ohmic contact, as seen in Figure 1–4(a). When the doping is high enough, the barrier will have a narrow enough width that charge carriers can tunnel through during field emission (FE) seen in Figure 1–4(c). Thermionic field emission (TFE) seen in Figure 1–4(b) exists at doping levels in between

TE and FE as energetic charge carriers tunnel through a narrowing energy barrier above the flat conduction band level.

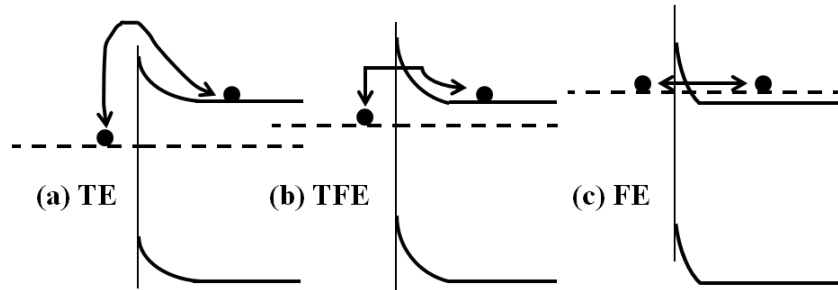


Figure 1–4. Three methods of conduction exist in ohmic contacts with increasing doping from (a) thermionic emission to (b) thermionic field emission to (c) field emission.

Adapted from [14].

The size of Φ_B , along with the doping concentration, influences the specific contact resistance (ρ_c) with various degrees of impact depending on the conduction method [21]. However, predicting Φ_B has been a matter of great complexity. The Schottky–Mott relationship shown in Eq. 1–2 between the metal work function, electron affinity, and barrier height, does not generally apply to many semiconductors—including SiC. In fact, many semiconductors are described by ‘Fermi-level pinning’, when Φ_B is nearly independent of the Φ_M for the contact. The Bardeen model attributes this behavior to interface states in the semiconductor [9], [11]. The degree of Fermi-level pinning, often discussed as $d\Phi_B/d\Phi_M$, remains modest for SiC [11]. Meanwhile the Fermi-level pinning for InN is strong, placing the Fermi-level inside the conduction band [19]. With neither Fermi-level pinning nor the Schottky–Mott relationship fully describing ohmic

contact formation to SiC, the exploration of ohmic contacts to SiC has been studied on more of a ‘trial-and-error’ basis [12].

$$\Phi_B = \Phi_M - q\chi_s \quad (1-2)$$

1.3 Materials of Interest

1.3.1 Silicon Carbide

Silicon carbide (SiC) is a wide bandgap semiconductor with properties well-suited for high-temperature and high-power devices. The structure of SiC can be any of the more than 200 polytypes, but the composition of SiC always has equal quantities of Si and C. The Si and C atoms each exhibit short bond lengths to their four nearest neighbors (1.89 Å), resulting in high hardness (Mohs hardness = 9) and near constant density [7]. The differences between SiC polytypes come from the stacking sequences to form repeating unit cells. Most SiC research has been directed towards the 3C (cubic), 4H (hexagonal), and 6H (hexagonal) polytypes shown in Figure 1–5. The stacking sequences are that 3C repeats as ABC, 4H as ABCB, and 6H as ABCACB. The 4H and 6H polytypes belong to space group 186, with $P6_3mc$ symmetry; while 3C-SiC belongs to space group 216, with $F\bar{4}3m$ symmetry. 3C-SiC is also known as β -SiC, while all other polytypes are referred to as α -SiC. Towards the end of the 19th century, mixed polytype platelets for use as abrasives were produced by the Acheson process of heating petroleum coke, silica, and graphite for days [7]. While SiC is still used as an abrasive today, SiC as a semiconductor became of interest in 1955 with the Lely process of

sublimating Si and C onto platelets from the Acheson process [7]. Small yields and limited control over orientation and polytype made SiC a very specialized research area. Significant research interest in semiconductor SiC only truly blossomed with the availability of single crystal SiC wafers in the 1980s [7].

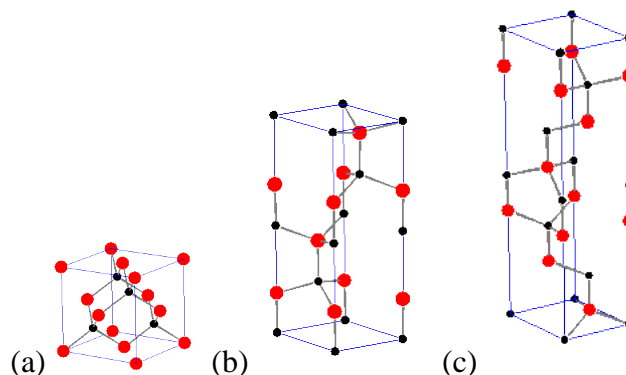


Figure 1–5. The most common SiC polytypes are (a) 3C, (b) 4H, and (c) 6H. The larger circles are Si atoms, and the smaller circles are C atoms. *Made in PowderCell* [22].

While these SiC polytypes exhibit indirect wide bandgaps, the bandgap and electronic properties vary considerably with polytype, as seen in Table 1–1. Forming SiC by a melt process can introduce defects that alter the polytype; therefore, single crystal SiC is frequently formed by seeded sublimation growth [7]. Homoepitaxial layers are then grown on the single crystal substrate, commonly by chemical vapor deposition (CVD) [4], [7], [11]. The formation of high quality, single crystal SiC is necessary for electronics research in order to have consistent behavior. Dopants can also be introduced during growth of the substrate or epitaxial layers as desired. For ohmic contacts to SiC, high doping levels have been very important. Being composed of Group IV elements, SiC has similar dopants to Si: namely, B and Al for *p*-type as well as P and N for *n*-type.

Ion implantation can also be performed for SiC. SiC growth is still very slow and time-consuming, resulting in a high expense for the semiconductor wafer alone. SiC wafers can now be produced commercially with diameters up to 6 in.

Table 1–1. Properties of Si and SiC.					
All Si properties from [7].					
<i>Properties</i>	<i>Si</i>	<i>3C-SiC</i>	<i>4H-SiC</i>	<i>6H-SiC</i>	<i>SiC Source</i>
Lattice Constant a (Å)	5.43	4.3596	3.0730	3.08063	[23]
Lattice Constant c (Å)	<i>ibid</i>	<i>ibid</i>	10.053	15.1173	[23]
Bandgap (eV)	1.12	2.39	3.263	3.023	[23]
Critical Electric Field (MV/cm)	0.25	2.5	2.2	2.5	[7]
Electron Mobility in n -type SiC (cm ² /Vs)	1350	~800	~880	~400	*SiC basal plane [24], [25]
Hole Mobility in p -type SiC (cm ² /Vs)	480	~40	~120	~100	*SiC basal plane, 3C [7] 4H/6H [24], [25]
Thermal Conductivity (W/cm K)	1.5	5	5	5	[7]

Only the 3C polytype has isotropic properties, as well as high mobility [7]; however, stacking faults can easily shift growth into another polytype with new properties. While 3C-SiC is very difficult to grow as a single crystal, polycrystalline 3C-SiC has become of great interest for micro-electrical-mechanical system (MEMS) devices [4]. Many electrical studies [9]–[12] were performed on the 6H polytype with a larger E_g ; however, the anisotropy of properties including mobility is quite large. Due to a similar E_g but only ~10% anisotropy in mobility, 4H-SiC wafers have become the preferred polytype for most electronics research since they became available [4]. The

{0001} wafers are commonly sliced off-axis to limit defects during epitaxial growth [7], with 8° towards $(11\bar{2}0)$ being common for 4H-SiC.

SiC has a low number of intrinsic carriers (n_i) compared to Si due to the high E_g , as seen in Eq. 1–3 where k_B is the Boltzmann constant. When atom vibrations from increasing temperature (T) create electron–hole pairs, the number of intrinsic carriers increases in the semiconductor. These carriers can dominate even in a doped semiconductor at high enough temperatures, which can eliminate any p – n junctions present [7]. The wide bandgap offers a high intrinsic temperature limit for SiC near 1000°C . The wide bandgap also increases the impact ionization energy for SiC, allowing a much larger electrical field before device breakdown [7]. The high thermal conductivity favors high-temperature operation before thermal-mechanical related failure.

$$n_i \propto e^{-E_g/(2k_B T)} \quad (1-3)$$

SiC is quite chemically inert, rendering most wet etchants beyond molten salts ineffective [4], [7]. Microfabrication of SiC devices commonly involves dry etching with fluorine-containing species, such as SF_6 . The F atoms attack the Si and C atoms to form gaseous species that diffuse away. SiC has been attractive due its native oxide (SiO_2) being identical to that of Si; however, the oxide grows very slowly on SiC—less than $0.1\ \mu\text{m}$ even after 10 h. This chemical inertness of SiC, however, does help extend device viability in harsh environments.

1.3.2 Indium Nitride

Indium nitride (InN) is another semiconductor that exhibits multiple polytypes. The stable polytype also has a hexagonal, non-centrosymmetric crystal structure in space group 186, with the $P6_3mc$ structure. The structure can be seen in Figure 1–6. As other Group III–nitride (III–N) semiconductors have wide bandgaps, the E_g for InN was erroneously reported for years as being of similar range at 1.9 eV [19], [26]. In truth, the supposed bandgap was attributed to an impurity absorption level; the actual InN bandgap is quite narrow, known to be ~ 0.64 eV since 2003 [19]. This E_g makes InN sensitive to infrared wavelengths. InN can still be combined with other III–N semiconductors, GaN and AlN, to tailor the E_g to many different wavelengths. The narrow E_g of InN actually expands the tunable bandgap range for compound III–N semiconductors to a near match for the solar spectrum [19].

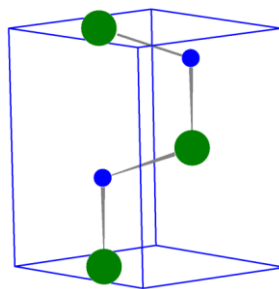


Figure 1–6. The hexagonal structure of InN. The larger circles are In atoms, and the smaller circles are N atoms. *Made in PowderCell* [22].

Undoped InN is an n -type semiconductor with E_F pinned above E_c [19]. This behavior results in all metal–semiconductor interfaces being ohmic contacts rather than Schottky contacts [19]. The availability of p -type InN is restricted due to the Fermi-level

pinning; however, possible *p*-type conductivity has been detected in Mg-doped bulk InN below the *n*-type surface [27]. Both vacancies and other gaseous impurities such as H₂ [19] have been proposed as completely compensating the *p*-type dopants.

Epitaxial InN films have been grown by metal organic CVD (MOCVD) and by molecular beam epitaxy (MBE) [26]. Crystal quality and orientation are directly influenced by the choice of substrate (commonly alumina) and the presence of any buffer layers such as GaN. The bulk electron mobility of MBE-grown InN can be $> 2000 \text{ cm}^2/\text{Vs}$ for both polarities [28], [29] at various temperatures, providing exceptionally fast carrier transport even with the large number of electrons.

While some research has focused on the semipolar and nonpolar faces [30], the polar faces of InN are the (0001) In-face and the (000 $\bar{1}$) N-face, as seen in Figure 1–7. A polarization vector forms along the *c*-axis, causing an intrinsic electric field. Some of the properties affected by the polarity along the $\langle 0001 \rangle$ directions will be discussed later. From an applications point of view, N-face InN is considered more promising due to the higher growth temperature, which suggests a higher thermal stability than In-face InN [28].

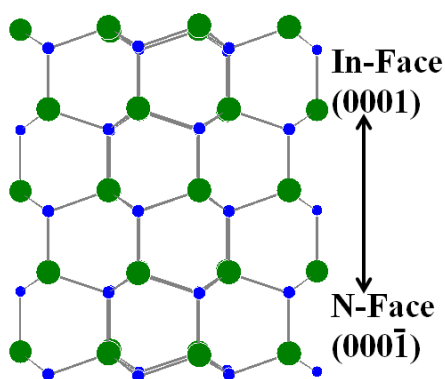


Figure 1–7. The polar faces of InN, as seen from a $(1\bar{1}2)$ projection. The larger circles are In atoms, and the smaller circles are N atoms. *Made in PowderCell* [22].

InN is not as chemically or thermally robust as SiC. Decomposition of InN starts around 500 °C, limiting its reliable use to lower temperatures [26]. InN can be both dry-etched and wet-etched using more commonplace chemicals, including hydrochloric acid (HCl). From the aforementioned sensitivity, though, InN is thought to have promise for H₂ gas sensors, as well as optoelectronic applications such as photovoltaics, fiber optics, and LEDs.

Chapter 2

Methods and Techniques

This chapter serves to describe the theory, background, and methodology for fabrication and characterization equipment. Specific work and materials details will be further discussed in subsequent chapters as they relate to the results. As a fellow in the NASA Space Technology Research Fellowship (NSTRF) program, part of this research was carried out at NASA Glenn Research Center (GRC). Indication will be made in describing specific systems as to their location at PSU or GRC.

2.1 Sample Fabrication Techniques

2.1.1 Physical vapor deposition

The heart of this dissertation is an exploration of metal–semiconductor interfaces. While the semiconductor substrates and epilayers were obtained commercially or from other researchers, the formation of thin films on SiC and InN was an integral part of this work. All thin films were deposited using physical vapor deposition (PVD) techniques. The source materials for the films are small pellets or target disks of the desired materials. These solid materials are temporarily transformed into gaseous species without chemical reaction in order to transport the material to the surface—hence, the name physical vapor deposition. Evaporation and sputtering are two PVD techniques

which are performed inside vacuum systems. Samples underwent appropriate surface preparation to remove surface contaminants that would alter the interface formed in deposition, such as organic particles, trace metals, and oxides. After appropriate surface treatment, the samples are placed inside a vacuum chamber. These chambers can then be pumped down from atmospheric pressure to high vacuum using two stages of pumping. The base pressure inside the chamber is $\sim 10^{-8}$ – 10^{-6} Torr before deposition. At this low pressure, the length atoms can travel before a collision is very long. This mean free path (λ_{mfp}) allows atoms from the source material to travel to the sample surface. The evaporated or sputtered atoms then adhere to the surface as well as the parts and walls inside the chamber [31].

Metal thin films can be evaporated from pellets or chunks of the target materials placed inside a crucible. Samples are screwed onto an inverted plate suspended from the top of the vacuum chamber. The water-cooled crucibles reside lower in the chamber. Electrons are produced from heating a filament, and then the electrons are steered using a magnetic field to arc up into the crucible. The electron beam then causes local melting of the metal, which evaporates into a gas. These atoms then spread out within the chamber, coating the sample and other items within line of sight from the source. The low chamber pressure limits reactions with any residual gases present [31], [32].

Refractory materials, alloys, and nonmetals are all more complicated to melt; hence, these materials are not commonly deposited by evaporation. Instead, the technique of sputtering utilizes a plasma to remove atoms from circular targets for depositing thin films. The sputtering targets are disks with diameters of 2, 3, or 6 in, providing an abundance of source material. In magnetron sputtering systems, these disks

are placed up against water-cooled sputtering guns with circular magnets in place to improve deposition rates. The material will be sputtered away from the target, but wearing will be preferential in a ring adjacent to the location of the magnet.

After reaching the desired base pressure, the vacuum system is backfilled with argon (Ar) gas to reach the desired operating pressure—typically in the mTorr range. A negative bias is applied to the target through the sputtering gun. The magnet keeps the electrons in proximity to the target, which in turn sustain the ions (Ar^+) in the plasma that are attracted to the negative target bias. The physical collisions of the ions send energetic atoms out of the target to cover the sample and chamber. In DC sputtering, the negative bias results in suitable yield for metals. For nonmetals, the less conductive nature of the target can cause charge build-up. An AC bias oscillating at radio frequencies (RF) helps dissipate the charge in RF sputtering, resulting in no net current through the target [31], [33]. Sputtering results in better conformal coverage than evaporation, as collisions with the Ar gas result in atoms depositing from random directions on the substrate [32].

2.1.2 Preparation of Indium Nitride samples

The indium nitride (InN) samples used in this dissertation were provided by the U. S. Army Research Laboratory (E. D. Readinger and M. Wraback). The indium nitride films were grown by plasma-assisted molecular beam epitaxy (PA-MBE) on gallium nitride (GaN) template layers upon sapphire (Al_2O_3) substrates. The GaN templates were grown 2 μm thick by metal organic chemical vapor deposition (MOCVD) for the In-face (0001) samples. The GaN templates for the N-face ($000\bar{1}$) samples were grown 0.5–

1 μm thick by PA-MBE on low-temperature GaN buffer layers [34]. The GaN templates were solvent cleaned with acetone, methanol, isopropanol, and deionized (DI) water. The templates were dipped in dilute 1:1 hydrochloric acid (HCl) prior to loading into the reactor. Prior to the In-face growth, the GaN surface was cleaned *in-situ* with a 2-min Ga flash.

The received InN surfaces were degreased before metal deposition for 5 min in acetone, 1 min in isopropanol, and 5 min in DI water. The samples were then soaked for 2 min in dilute HCl, mixed by volume to be 1:10 ratio of HCl to water. This concentration had been shown not to significantly etch away or roughen the surface of InN. The samples were then rinsed for 2 min in DI water before being blown dry with nitrogen (N_2) gas. The samples were loaded into an Edwards Auto 306 Vacuum System at PSU seen in Figure 2–1(a) for electron beam (e-beam) evaporation. Nickel (Ni) films were deposited at a rate of 1 $\text{\AA}/\text{s}$ after reaching a base pressure of $\sim 10^{-6}$ Torr. Additional Ni films for higher temperatures and longer durations were deposited at PSU in a Denton 502-A DC Magnetron Sputtering System seen in Figure 2–1(b). These films were sputtered at 5.5 mTorr at 1.2 $\text{\AA}/\text{s}$ after reaching a base pressure $< 10^{-7}$ Torr.



Figure 2–1. (a) The interior of the e-beam evaporation system for evaporating metals from the crucibles at the bottom to the samples on top (behind the shutter). (b) The interior of the sputtering system for depositing metals from the targets up top (behind the shutters) to the sample stage below.

2.1.3 Preparation of Silicon Carbide samples

Four *p*-type 4H-SiC epilayers with different doping levels were fabricated into transfer length measurement (TLM) structures with varying W:Ni alloys according to the following methods at GRC. Variations are included at the end for *n*-type samples as well as additional *p*-type samples that were fabricated with only ohmic alloy compositions. All samples consisted of doped epilayers grown on semi-insulating (SI) SiC substrates obtained commercially from Cree, Inc.

2.1.3.1 Mesa formation

Quarter wafers were diced into squares $\sim 1 \text{ cm}^2$ using a water-cooled dicing saw. Due to the transparent nature of SiC, current–voltage tests were performed on the surfaces of the diced pieces to confirm the doped epilayer location. These samples were

cleaned in acetone and isopropanol before being blown dry with N_2 . The samples were then loaded into a 6-in sputtering system seen in Figure 2–2 built from Materials Research Corporation parts. The 6-in targets allow for large uniformity in the films deposited over many small samples at once. After reaching a base pressure of $\sim 10^{-7} - 2 \times 10^{-6}$ Torr, the system was used to deposit 3 μm of aluminum (Al) as a sacrificial layer. The operating pressure was ~ 8 mTorr, sputtering at 100 W over ~ 5 h.



Figure 2–2. A Materials Research Corporation 6-in sputtering system was used for depositing sacrificial Al films.

Each Al-coated piece was placed on a photoresist spinner and covered in 1–2 drops of hexamethyldisilane (HMDS) as an adhesion promoter. These samples were then spun at 3000 rpm for ~ 20 s. The samples were then covered in 2–4 drops of Shipley S1813 positive photoresist before being spun at 3000 rpm for 40 s. The samples were then placed in a Petri dish and hard baked at $90^\circ C$ for 5 min in a N_2 oven. The resist was then patterned using contact photolithography. The mask for the mesa layers was placed in the Karl Süss MJB3 Aligner seen in Figure 2–3. This mask was aligned to each sample on a vacuum chuck before being exposed in contact for 12 s at 8 mWcm^{-2} . The

exposed samples were all placed in MF-319 developer for 2 min before a 5-min DI water rinse and being blown dry with N_2 gas.

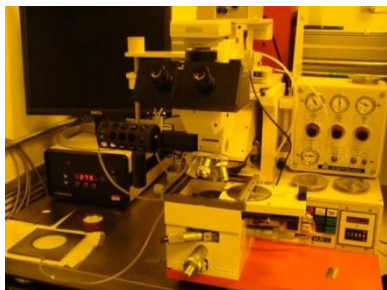


Figure 2–3. A Karl Süss MJB3 Aligner was used for patterning and exposing photoresist.

A beaker of phosphoric acid (H_3PO_4) was placed on top of Teflon bubbling balls in a water bath. The phosphoric acid was heated in this arrangement to $50\text{ }^{\circ}\text{C}$, with the temperature regulated by the thermocouple seen in Figure 2–4(a) plugged into the hot plate. The hardened photoresist acted as a mask for etching the Al sacrificial layer. The samples were each etched in the H_3PO_4 for 5–9 min until the hydrogen gas bubbles ceased forming around the sample. The solution was only used while the temperature was stable, between $48\text{--}54\text{ }^{\circ}\text{C}$, in order to not vary the etch rate significantly. All pieces were rinsed in DI water and blown dry with N_2 gas. The photoresist was examined in a filtered optical microscope to ensure fidelity of the lithographic transfer. The photoresist was then stripped in acetone.

The samples were then loaded into the reactive ion etcher (RIE) seen in Figure 2–4(b) and (c). This system is pumped out to a vacuum of $\leq 10^{-5}$ Torr. The process gas of 25 sccm Ar and 15 sccm SF_6 at 25 mTorr was then introduced into the chamber. A RF power supply formed a plasma within the chamber from the processing gas. The ionized

gas is even more reactive in etching the Al and SiC. The showerhead formation seen in Figure 2–4(c) causes the gas to be highly directional into the samples, and minimizes the side etching of the SiC areas protected by the Al. RIE etching was conducted at 400 W_{RF} for ~1 h to etch mesas ~3 μm into the SiC. Current–voltage probes applied to adjacent mesas proved the junction isolation by the lack of measurable current flow. The remaining Al sacrificial layer was then etched in another hot H₃PO₄ bath until all hydrogen bubble formation had ceased.

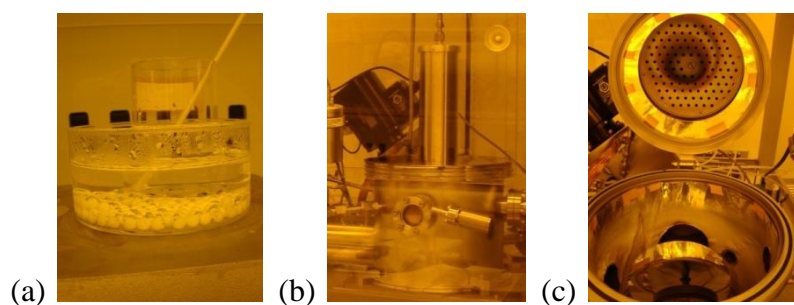


Figure 2–4. (a) A H₃PO₄ solution in a water bath was heated on a hot plate for wet etching the Al layers. The RIE chamber (b) exterior and (c) interior was used for directional dry etching of SiC and the metal layers.

2.1.3.2 Contact formation

The SiC surfaces were once again degreased with acetone and isopropanol before being blown dry with N₂ gas. These surfaces then underwent a ‘piranha clean’ to remove organic contaminants. The piranha solution used here consisted of a 1:1 volume ratio of sulfuric acid (95–98% H₂SO₄) and 30% hydrogen peroxide (H₂O₂). The steps below were used to prepare ~150 mL of piranha solution, sufficient for most small pieces. Appropriate personal protective equipment for all acid work included Trionic® gloves, an acid apron, and face shield. The arrangement shown in Figure 2–5(a) for piranha

solution limits any lab damage from the exothermic reaction as well as reduces the difficulty in retrieving the samples.

1. Pour 75 mL of H_2O_2 into a 400 mL beaker. Rest the beaker on top of an inverted Petri dish in the acid hood so the exothermic reaction does not damage the hood surface.
2. Pour 75 mL of H_2SO_4 into a second 400 mL beaker.
3. Place the SiC sample(s) in a Teflon basket.
4. Pour the H_2SO_4 into the H_2O_2 beaker. Then rinse the empty acid beaker.
5. Lower the Teflon basket into the piranha solution for 15 min. Use Teflon tweezers, if necessary, to help prevent samples from floating.
6. Lift the Teflon basket into the DI water tub rinse with active water flow for 10+ min after piranha clean. Blow the samples dry with N_2 gas.
7. Allow the piranha solution to be fully spent before collecting the waste in a bottle with a perforated cap for off-gassing.

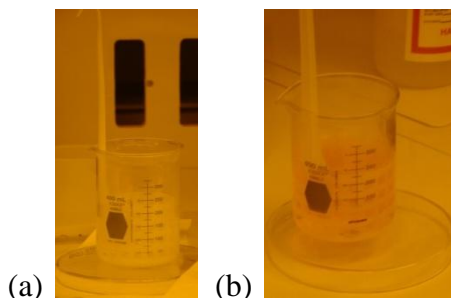


Figure 2–5. (a) A Teflon sample basket in a beaker of 1:1 piranha solution on top of a Petri dish. (b) A Teflon sample basket in a beaker of 2:1 aqua regia on top of a Petri dish.

The dried samples then underwent a 30–60 s dip in 49% hydrofluoric acid (HF) in a Teflon beaker. The HF etched away any silicon dioxide (SiO_2) formed on the surface of the SiC. The samples then underwent a 10+ min DI tub rinse. After being blown dry with N_2 gas, the samples were then loaded into a sputtering system.

A custom two-chamber ‘Gemini’ RF/DC magnetron sputtering system (3-in targets) was used for contact metallization. The two-chamber system was pumped to a base pressure of $\sim 10^{-8}$ – 10^{-7} Torr. The system then underwent a 1 h bake-out at 300 °C before cooling for another hour. Titanium (Ti) was DC-sputtered in the right hand chamber of the system seen in Figure 2–6 as an active getter of oxygen from the gas in the chamber. The isolation valve between the two chambers was half-closed during deposition to limit the movement of Ti atoms. The left-hand chamber in Figure 2–6 has two guns oriented opposite one another, with the mount for the sample in between the guns in place of a shutter. After 5 min of Ti sputtering, the W or W:Ni target was pre-sputtered for 5 min at 10.2 mTorr. This pressure was selected to minimize film stress from analysis done during process development. The RF sputtering power and time were kept constant between all the W/W:Ni metal targets at 200 W_{RF} and ~ 18 min 5 s. The resultant film thicknesses were closer to 1600–1800 Å rather than the goal of 2000 Å, as measured from both etch-back samples and along the cross-section of a wafer. The power–time conditions were maintained for consistency in all deposited samples. After extinguishing the plasma around the metal target and igniting the other RF gun, the sample mount was reoriented to deposit Si. A thin Si cap (~ 70 Å) was deposited for 1 min 42 s at 200 W_{RF} and 4.5 mTorr. The chamber was allowed to cool to room temperature before extracting the samples.

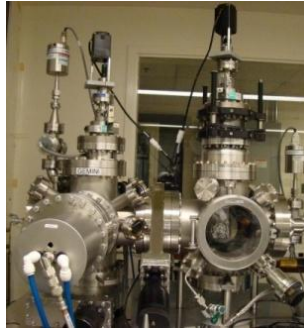


Figure 2–6. The two-chamber sputtering system was used for depositing Si/W:Ni layers in the left hand chamber, and sputtering Ti as an oxygen getter in the right hand chamber.

Another layer of 3 μm of Al was deposited in the 6-in sputtering system upon the metallized mesas. This sacrificial layer was patterned according to the same photolithography procedure as the mesas. The contact mask was aligned to the marks from the mesa layer before exposure. After development, another hot H_3PO_4 bath etched the Al layer; and the photoresist was then stripped. The RIE plasma consisted of 140 sccm Ar and 5 sccm SF_6 with a chamber pressure of 25 mTorr powered at 300 W_{RF} . This combination etched the Si/W:Ni layers without considerable etching of the SiC over times varying from 27–37 min. The RIE etch was performed incrementally until the areas between the mesas and those between the contacts were cleared of metals. After an isolation check, the Al was stripped in a final hot H_3PO_4 bath. The samples of SiC ($\sim 1 \text{ cm}^2$) were then diced into smaller pieces for annealing.

2.1.3.3 Variations for the n-type samples

The *n*-type samples and some *p*-type samples ($N_{\text{A}} = 1 \times 10^{20} \text{ cm}^{-3}$) underwent a piranha clean, followed by a deliberate oxidation before initial dicing to protect the

surface from the adhesive and metal contaminants. These samples were first thermally oxidized in a tube furnace for 3 h at 1150 °C. However, the chemical robustness of SiC creates only a very thin SiO₂ film, around 40 nm. Further SiO₂ was deposited by using tetraethyl orthosilicate (TEOS), which self-decomposes into SiO₂ without additional consumption of the SiC layer. The TEOS procedure is an automated process resulting in growth of ~1 µm from a full day run. After dicing, the SiO₂ was then stripped for 30 min in 6:1 buffered oxide etchant (BOE).

These surfaces were cleaned with a piranha clean, an 'aqua regia' clean, and an HF dip before Al deposition for mesa formation. The red aqua regia clean seen in Figure 2–5(b) was performed to remove any trace metal contaminants. The aqua regia was mixed as a 2:1 solution of hydrochloric and nitric acids, HCl:HNO₃. The HNO₃ was added to the HCl, and the samples were lowered in the Teflon basket for 10–15 min. The samples were rinsed in the DI tub rinse for 10+ min before the HF dip. The aqua regia solution was allowed to be fully spent before collecting the waste in a bottle with a perforated cap for off-gassing.

The photolithography spinner was replaced, with the new spin settings at 6000 rpm for 60 s after application of the HMDS, followed by a 4 min bake at 90 °C in air. The photoresist was spun at 3000 rpm for 60 s before being baked at 90 °C. After mesa formation, these samples underwent another piranha clean and HF dip before a dry oxidation for 1.5 h at 1150 °C to clean the surface. This dry oxide was stripped before loading the two-chamber sputtering system for contact metallization.

2.1.4 Annealing

After fabrication, all samples underwent annealing for ohmic contact formation (SiC) and/or thermal stability (SiC and InN). Annealing for ohmic contact formation on SiC occurred in a dedicated Thermcraft, Inc., three-stage tube furnace at GRC seen in Figure 2–7(a). The SiC samples were placed on a carrier sled in the center of Stage 2. Samples were loaded at 150 °C under 5 slpm of ultra-high purity Ar gas. Ti slugs on separate boat(s) were upstream of the samples for additional oxygen gettering of the Ar gas. Reaching peak annealing temperatures of 1000 °C, 1100 °C, 1150 °C, and 1200 °C consisted of 0.75–1 h of ramp time before 0.5 h at peak temperature. The samples were extracted from the furnace at 150 °C after cooling for several hours, with a cross-over to N₂ gas below 600 °C.

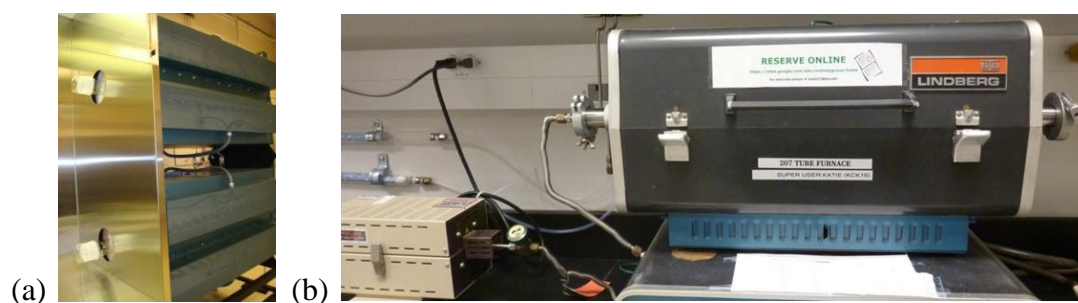


Figure 2–7. (a) The three-stage tube furnace was used for ohmic contact formation on SiC, and (b) the tube furnace with the gettering furnace (on left) was used for aging InN and SiC samples.

The InN and SiC samples were aged in a Lindberg tube furnace at PSU seen in Figure 2–7(b). This tube furnace has a gettering furnace upstream of the samples to

remove oxygen from the ultra-high purity Ar or N₂ gas. For the shorter runs aging the InN samples, the tube was loaded into the furnace after reaching peak temperature and extracted upon completion. The longer runs aging the SiC samples began and ended with the tube already inside the furnace.

Additional layers on SiC were studied using an AS-One rapid thermal annealing (RTA) system at GRC shown in Figure 2–8. Samples are placed on a carrier SiC wafer. This system has a roughing pump attached to achieve a vacuum in the mTorr range before a gas purge with N₂ or Ar. The system can then ramp to temperature in minutes with the heating lamps. This computer-controlled system has temperature feedback from the system pyrometer as well as monitoring of the gas flow and pressure. The system is both water- and gas-cooled to return to room temperature.



Figure 2–8. The AS-One rapid thermal annealing system with heating lamps above the carrier wafer was used in the diffusion barrier study.

2.2 Electrical Characterization

While many electrical measurements can be made, the simultaneous ohmic contact study was focused specifically on the specific contact resistance. Forming ohmic

contacts to SiC has been a difficult proposition as, quite often, metals form rectifying contacts [9], [10].

2.2.1 Transfer length measurement structure

Linear transfer length measurement (TLM) test structures were used to evaluate the electrical properties of the ohmic contacts to SiC. The TLM electrical structure consisted of six rectangular pads placed at different distances apart, as seen in Figure 2–9. These contacts reside on a raised mesa of the doped epilayer; and the mesas are electrically isolated from each other. The TLM mask had three different sets of dimensions for contact spacing and length, with five mesas in each set on the mask. The first gap (d_{12}) in the TLM patterns had nominal spacing of 35, 30, and 25 μm , with subsequent gaps spaced at $2 \times$, $3 \times$, $4 \times$, and $5 \times d_{12}$. The nominal contact lengths (L) were 50, 45, and 40 μm , along with nominal widths (Z) of 100 μm . These values are summarized in Table 2–1 for the three dimensions. After completed samples were diced, an ideal sample had 15 TLM mesas—five of each size set. The actual number of TLM structures on pieces utilized for characterization varied from 8–21. The gap spacings and contact dimensions were measured in field-emission scanning electron microscopes (FESEMs) to ensure accurate fits, even with process variations. At least three measurements for each dimension per sample were collected and then averaged.

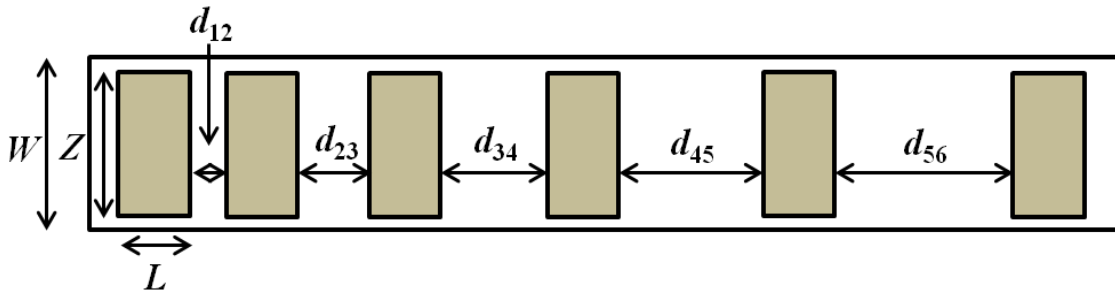


Figure 2–9. The TLM structures consisted of six contacts on top of a raised mesa.

Dimensions are marked with their labels: mesa width (W), contact width (Z), contact length (L), and gap spacings (d). *Adapted from* [14].

Table 2–1. Nominal dimensions of the TLM gap spacings for constant width of $Z = 100\ \mu\text{m}$.			
	$L = 40\ \mu\text{m}$	$L = 45\ \mu\text{m}$	$L = 50\ \mu\text{m}$
d_{12}	35 μm	30 μm	25 μm
d_{23}	70 μm	60 μm	50 μm
d_{34}	105 μm	90 μm	75 μm
d_{45}	140 μm	120 μm	100 μm
d_{56}	175 μm	150 μm	125 μm

Current–voltage measurements were obtained between two consecutive contacts in order to obtain the resistance (R_T), per Ohm’s law (Eq. 2–1). These measurements were collected using a four-probe configuration, with the current sourcing conditions limited to $\pm 0.01\ \text{A}$. In order to minimize any artifacts due to the metal sheet resistance [35], the probes were placed as close to collinear as possible. The voltage probes were closest to the gap, and the current probes were placed at the far ends of the contact lengths, as seen in the idealized schematic of Figure 2–10(a). Nonlinear measurements were not strictly rectifying, but exhibited curvature in both current directions, as seen in

Figure 2–10(b). These nonlinear measurements have not been quantified in this dissertation or any journal. Resistances were obtained only from linear measurements with good fits ($R^2 > 0.99$), as seen in Figure 2–10(c). For current–voltage measurements from the *p*-SiC samples, the current–voltage measurements showed minor deviations from linearity, especially at higher currents. These deviations can come from artifacts and vibrations in the measurement set-up. For these conditions, the R_T values were extracted from ± 0.002 A within the full current–voltage range with strict adherence to good fits.

$$R_T = V/I \quad (2-1)$$

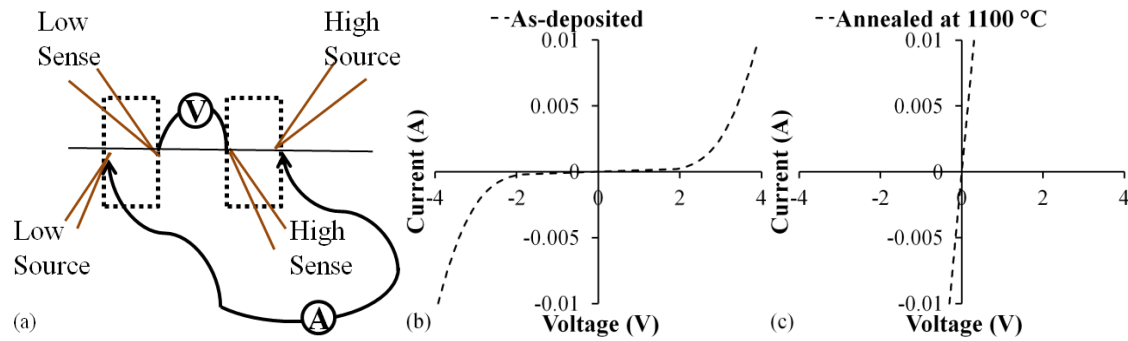


Figure 2–10. (a) The ideal configuration of four probes for current–voltage measurements in order to extract the specific contact resistance values. Current–voltage measurements to W50:Ni50/*n*-SiC were (b) nonlinear as-deposited and (c) ohmic after annealing at 1150 °C.

2.2.2 Specific contact resistance extraction

The resistance values were plotted against gap spacing (R_T vs. d) as seen in Figure 2–11. A linear fit ($R^2 > 0.99$) resulted in the extraction of the transfer length (L_T) and sheet resistance (R_{sh}) according to Eq. 2–2; and from these parameters and Eq. 2–3, the specific contact resistance (ρ_c) was calculated [14]. The semiconductor sheet resistance R_{sh} , or resistivity divided by thickness, was extracted from the slope. The size-dependent value of the contact resistance (R_c) was extracted from the y-axis intercept. The transfer length L_T , or length through the contact where the current flows between the metal and the semiconductor, was extracted from the x-axis intercept [14]. The ρ_c is a size-independent measure of the contact resistance, which is important for comparing values from different test structures and studies.

$$R_T = \frac{R_{sh}}{Z} d + 2R_c \approx \frac{R_{sh}}{Z} (d + 2L_T) \quad (2-2)$$

$$\rho_c = R_{sh} (L_T)^2 \quad (2-3)$$

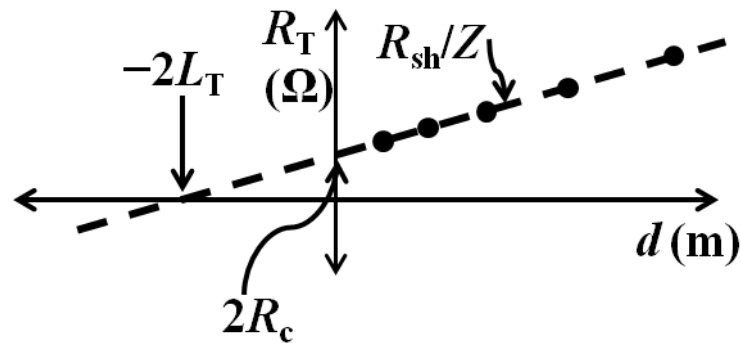


Figure 2–11. The schematic model of a TLM fit for R_T vs. d as shown in Eqs. 2–2 and 2–3. Adapted from [14].

These equations are valid as long as the length of the contacts is much greater than the transfer length ($L \geq 1.5 L_T$). When the L is not much greater than L_T , the ρ_c calculated by Eq. 2–3 must be multiplied by $\tanh(L/L_T)$ to account for the length ratio no longer resulting in the hyperbolic tangent being near unity. The lowest detectable ρ_c according to the linear TLM method is detailed by Eq. 2–4, being limited by the thickness (t) of the epilayer and the sheet resistance (e.g., doping) of said layer [14].

$$\rho_c \geq 0.2 R_{sh} (t)^2 \quad (2-4)$$

Any linear fits with $R^2 < 0.99$ were not included in the reported data. Some fits and ρ_c extractions were performed with only four points instead of five due to damage, debris, and strong visible displacement from linearity. Another irregular situation occurred when L_T values were very close to or below zero, even for data that exhibited a good linear fit ($R^2 > 0.99$). The quantity L_T cannot physically be negative, nor can ρ_c . In these cases, the linear fitting parameters used in the regressions modeled in Figure 2–11 were used with their uncertainties to obtain the maximum ρ_c value. Linear regression is strongest with the more known variable as the dependent variable; hence, the data were re-plotted as d vs. R_T . The uncertainty (s_m and s_b) in the least squares fitting parameters from Eq. 2–5 was obtained from the LINEST extraction in Microsoft Excel. The uncertainties were subtracted from the fit parameters (e.g., $m - s_m$) to find the maximum ρ_c that could be confidently reported from the measurements with a positive L_T , even if the actual ρ_c was lower.

$$m = \frac{Z}{R_{sh}} \text{ and } b = \frac{-2R_c Z}{R_{sh}} \quad (2-5)$$

2.3 Materials Characterization Techniques

The materials characterization techniques used in these studies provide a variety of information in different ways. The methods and their benefits (and limitations) will be discussed in the context of the information they provide: structure, morphology, and composition.

2.3.1 X-ray diffraction

X-ray diffraction (XRD) is a nondestructive technique used for phase identification based on crystal structure. Crystals have a repeating arrangement of atoms (a unit cell) in three-dimensional space. This long-range order can be defined not only by the geometrical shape (the lattice) used to define the unit cell but also the symmetry found in the arrangement of atoms. The lattice parameters include the lengths of the unit cell vectors (a , b , and c) as well as the angular relationship between the three vectors (α , β , and γ). The various two-dimensional sheets of atoms inside the lattice are termed crystal planes. Miller indices (hkl) are used to name each crystal plane by the reciprocals of the plane/cell vector intersections. A specific plane is named (hkl), while the family of planes that are integer permutations and negatives of each other is termed $\{hkl\}$. The interplanar spacing, or distance between each plane in a family, is termed d (d_{hkl}). XRD detects the peak locations in d^* -space corresponding to X-rays diffracting off crystal planes according to the symmetry of the structure [36]. The d_{hkl} can be calculated from

the lattice parameters, e.g., using Eqs. 2–6 and 2–7 for orthorhombic and hexagonal structures, respectively.

$$\text{orthorhombic } \frac{1}{d_{hkl}} = \frac{h^2}{a^2} + \frac{k^2}{b^2} + \frac{l^2}{c^2} \quad (2-6)$$

$$\text{hexagonal } \frac{1}{d_{hkl}} = \frac{4}{3} \left(\frac{h^2 + hk + k^2}{a^2} \right) + \frac{l^2}{c^2} \quad (2-7)$$

The fundamental principle of XRD comes from Bragg's law (Eq. 2–8). Incident X-rays (1 and 2) interact with planes of atoms, resulting in diffracted X-rays (1' and 2') at the same angle relative to each plane of atoms, as seen in Figure 2–12. The parallel planes belonging to the same family $\{hkl\}$ result in the X-rays in position 2 traveling further than those in position 1, with a path spacing of $2d\sin(\theta)$ as shown by the line of blue squares. Constructive interference between the diffracted X-rays occurs when $2d\sin(\theta)$ is equal to an integer number of wavelengths ($n\lambda$). The integer wavelength condition results in a diffraction peak or 'reflection' in the XRD pattern. XRD patterns are commonly plotted with 2θ on the x -axis, based on the receiving geometry angle being 2θ from the incident direction as seen in Figure 2–13. The intensity of a peak for randomly oriented samples is related to the square of the structure factor F_{hkl} , which is calculated in Eq. 2–9 from the position of each atom in the unit cell (uvw) [36].

$$n\lambda = 2d_{hkl} \sin \theta \quad (2-8)$$

$$F_{hkl} = \sum_{n=0}^{n=\text{atoms}} f_n (e^{2\pi i \cdot (hu_n + kv_n + lw_n)}) \quad (2-9)$$

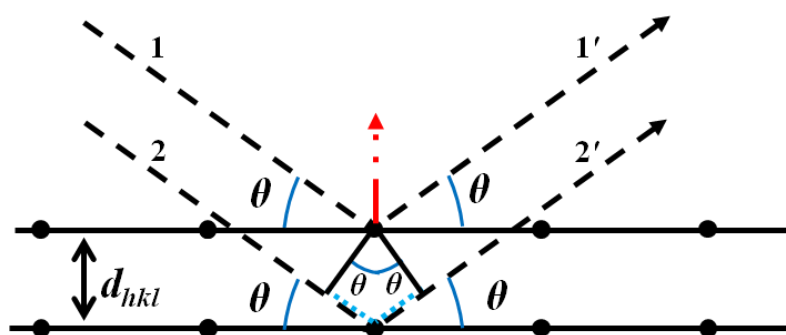


Figure 2–12. A visual depiction of Bragg's law: Crystal planes parallel to the surface are spaced at d_{hkl} and have a surface normal bisecting the X-ray path (shown as the dash-dot red vector). X-rays incident (1 and 2) at the Bragg angle θ are diffracted (1' and 2') from these crystal planes at the same angle θ . The path difference between the X-rays is the line of square dots, equal to $2d\sin(\theta)$. Adapted From [36], [37].

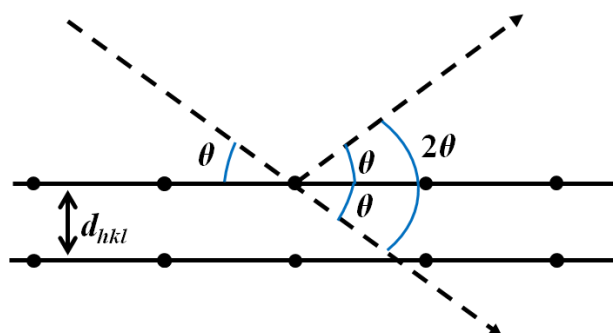


Figure 2–13. Visual depiction of the θ – 2θ symmetry of the incident and diffracted X-rays. Adapted from [36].

For all experiments performed here, the X-rays were generated from a copper source. The detectors are sensitive to X-ray collection for both angular position (2θ) and intensity (I) data collection. Researchers have expanded the available types and configurations of sources, optics, and detectors used in XRD for different sample types

and the information acquired. Three configurations of XRD available at PSU are discussed below.

2.3.1.1 Bragg–Brentano X-ray diffraction

Conventional powder XRD uses the Bragg–Brentano geometry, modeled after Bragg’s law pictured in Figure 2–12. The X-rays exit the Cu source and pass through Soller slits, which are thin parallel foils spaced at 0.04 rad to help limit the spread of the beam. The X-rays then pass through the programmable divergent slit (PDS), the beam mask (5 or 10 mm), and the fixed anti-scattering slit (0.5° or 1°). The Soller slits and beam mask limit the axial divergence of the beam on the sample. The PDS and the anti-scatter slit limit the beam spread on the sample in the direction perpendicular to the beam axis. The X-rays are then incident upon the sample at an incident angle (θ) and reflected at the same angle (θ). The receiving angle between the sample and the detector is θ , but the angle between the incident X-ray and the detector is 2θ , as seen in Figure 2–13. The diffracted X-rays pass through receiving optics consisting of a programmable anti-scatter slit, a second set of 0.04 rad Soller slits, and a 0.02 mm Ni filter before entering a linear PIXcel 1D detector [38]. The Ni filter minimizes the intensities of any Cu $K\beta$ reflections before the detector digitally records the intensities of the diffracted X-rays.

For Bragg–Brentano geometry, a PANalytical X’Pert Pro Multi-Purpose Diffractometer (MPD) was used (Figure 2–14(a)). The generator settings used for the Cu radiation are 45 kV and 40 mA. The MPD generator emits Cu $K\alpha_1$ and $K\alpha_2$ lines, with wavelengths of 1.54059 Å and 1.54443 Å, respectively. In this theta–theta (θ – θ) system, the incident beam (and optics) moves upward along a fixed arc, the goniometer circle.

Consequently, the detector (and receiving optics) also moves along the goniometer circle at the same speed and θ angles to collect any diffracted X-rays from the incident angles. The goniometer circle remains fixed in size; however, the ‘focusing circle’ between the source, sample, and detector does decrease in size at increasing θ angles. The thin film samples were placed on a single-crystal quartz (6° off the c -axis) low-background holder ($\sim 1 \text{ in}^2$), which does not significantly contribute further to the pattern. The height of the sample (and stage) must be precisely adjusted with a dial gauge before an XRD scan in order to fulfill the geometrical requirements of XRD.

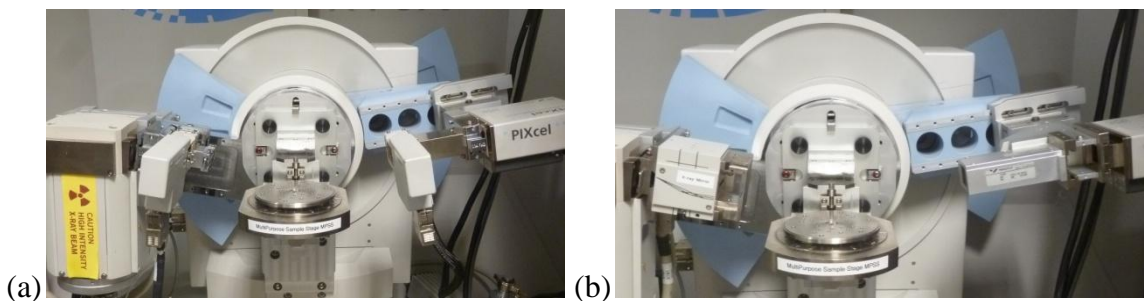


Figure 2–14. The PANalytical X’Pert Pro MPD θ – θ system can be used in (a) Bragg–Brentano configuration and (b) grazing incidence configuration (GIXRD).

2.3.1.2 Grazing incidence X-ray diffraction

Thin film specimens often allow for X-ray penetration deep into the sample, which results in the substrate peaks being much larger than those from a thin film. Bragg–Brentano geometry also only allows for the detection of planes which are parallel to the sample surface [37], [38]. In a powder sample, one expects $>10^6$ particles for random orientation and signals [38]. In thin films, often with preferred orientation, not enough grains have planes oriented parallel to the surface for detection; but an

asymmetric diffraction arrangement can detect these planes [39]. The same MPD system also has optics seen in Figure 2–14(b) which can be used for Grazing Incidence X-ray Diffraction (GIXRD). As seen in Figure 2–15, GIXRD allows for diffraction from planes not oriented parallel to the surface. In GIXRD geometry, the generated X-rays are diffracted by a parabolic mirror with multilayer graded coatings. The mirror and a 0.5° divergence slit shape the X-rays into nearly parallel beams incident upon the sample at a fixed, incident angle (ω). The shallow ($< 5^\circ$) ω angles allow the X-rays to pass laterally through the film(s) for longer distances, resulting in smaller penetration depths into the sample. A 0.27 mm parallel plate collimator (PPC) is placed before the PIXcel 1D detector, and this configuration can then be swept through the 2θ collection arc to record X-ray intensities from a variety of planes. The sample height upon the low-background holder must still be set precisely in GIXRD in order to fulfill the necessary geometry.

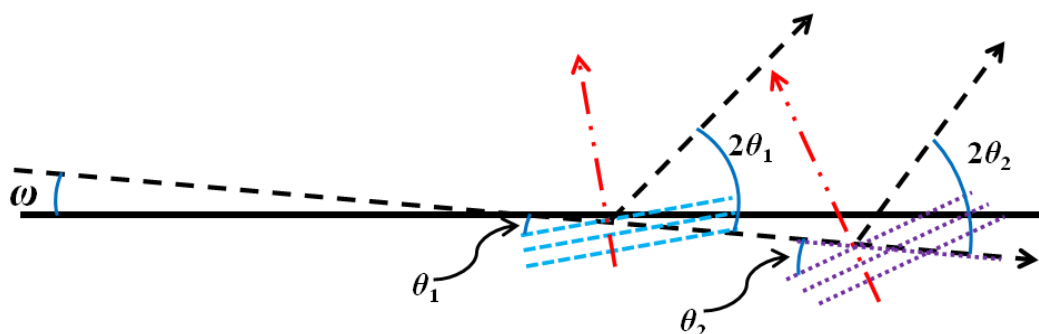


Figure 2–15. GIXRD orientation: The incident X-ray enters at a fixed angle ω , and diffracted X-rays from off-axis planes are detected at their 2θ angles. The red dot-dash vectors represent the plane normals, which are bisectors of the incident and diffracted beams. *Adapted from [39].*

2.3.1.3 Microdiffraction

Another XRD configuration is microdiffraction, performed in this study with the Rigaku DMAX-Rapid II microdiffractometer seen in Figure 2–16(a). The microdiffractometer generator conditions for Cu radiation are 50 kV and 40 mA. The X-rays emitted from the Cu source pass through a monochromator and a collimator before reaching the sample. The resultant X-rays from the Rigaku are considered to have a wavelength averaged between $K\alpha_1$ and $K\alpha_2$ (1.5418 Å). The X-rays, collimated to a small spot size (0.3 mm), are thus focused on a small area of the sample. Thin film samples are mounted on a Si low-background holder dotted with dish soap. The sample holder forms a fixed χ_g angle of 45° between the vertical axis of the cylindrical image plate and the normal of the sample/holder. During an XRD scan, the sample can be fixed, rotated around its own axis (ϕ), or rocked left and right around the vertical (ω) axis past the collimated beam [40]. The angle configuration can be seen in Figure 2–16(b).

Using a camera, the sample position is adjusted relative to the collimator to set the sample to the detector distance before an XRD scan. The adjustments result in the convergence of the sample, the ω rotation axis, the ϕ rotation axis, and the beam to avoid large sample movements during angular rotation (a eucentric point) [41]. Using ω angular oscillation, the sampling statistics can be improved for very small samples by increasing the area exposed to the beam [40]. The SiC samples were typically oscillated on the ω -axis through 8–10° with a fixed ϕ for 10 min. The experimentally determined outer bounds for ω oscillation were 12° and 37°, with typically two scans collected within these limits. A faster scan was collected at $\phi = 90^\circ$ from the initial mounting to confirm that no phase was missed due to geometry limitations.

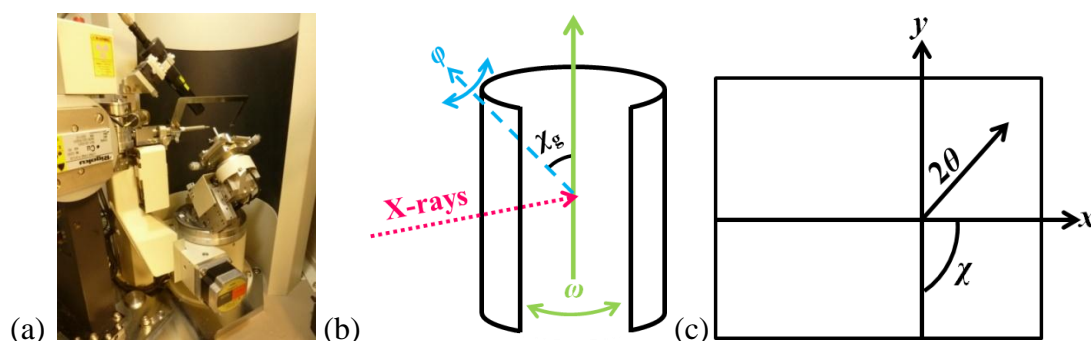


Figure 2–16. (a) The Rigaku DMAX-Rapid II microdiffractometer is shown with schematics of (b) the angle configurations relative to the area detector and (c) the Cartesian/polar coordinates of the detector. (b) and (c) adapted from [40].

The detector for the DMAX Rapid II consists of a curved image plate forming 210° of a vertical cylinder, as seen in Figure 2–16(a) and (b) [42]. Linear detectors in most diffractometers only collect a thin slice of the diffracted Debye cone of X-rays. The large-area detector on the microdiffractometer allows for collecting arcs or complete rings by intersecting the whole Debye cone [40], [41]. The rings may appear as brief arcs for low intensity reflections, an insufficient number of sampled grains, or preferred orientation [37], [39]. The mentioned cases all enhance the value of the large area detector. The X-rays reaching the detector interact with the BaFBr:Eu phosphor coating, and the intensity detection from the whole plate is read out in a rastering pattern by a laser at the end of the scan [40], [43]. A beam stop is in place during the scan to limit the direct X-ray beam permanently imprinting on the detector.

Points on the flat ‘unrolled’ image from the detector can be indexed to (x, y) positions or $(2\theta, \chi)$ in polar coordinates as seen in Figure 2–16(c). The reflection arc intensities can then be integrated [40], [44] from 2θ max/min to χ max/min angles on the

plate to obtain I vs. 2θ plots. The AreaMax 2.0 software limits areas from the reflection geometry, and a 0.02° step size is used. The reflection geometry with the cylindrical detector undergoes a defocusing effect which can cause a loss in resolution at higher 2θ angles [40].

Phase identification from all XRD I vs. 2θ patterns was performed using Jade2010 Analysis software by MDI of Livermore, CA, as well as the International Centre for Diffraction Data (ICDD) PDF 4+ database and the Inorganic Crystal Structure Database (ICSD). Additional diffraction patterns and crystal variations were also explored using Powder Cell for Windows v. 2.4 [22].

2.3.2 Electron microscopy

Electron microscopy involves probing a sample with high-energy electrons and collecting the perturbed electrons that have interacted with the sample. This interaction can take place over exposed surfaces, as in scanning electron microscopy; or by passing through a thinned sample, as in transmission electron microscopy.

2.3.2.1 Scanning electron microscopy

With the ever diminishing size of samples and their features, use of a scanning electron microscope (SEM) has become imperative for imaging. Imaging using an SEM is a nondestructive technique, but the sample must be vacuum compatible. Inside the SEM, electrons are emitted from a source and then accelerated to high voltages (~ 1 – 10 kV) under high vacuums. These electrons are strongly collimated and shifted with

magnetic lenses before reaching the sample surface. With the long λ_{mfp} , the electrons will not have other interactions before reaching the sample and being collected by the detector. Secondary electrons are emitted strictly from the surface, less than 50 nm in depth [14]. Images formed by secondary electrons provide good resolution of the morphology and for measuring features. Backscattered electrons originate from deeper into the surface of the sample but provide a visual contrast from different elements. Both SEMs used at PSU have field-emission (FE) sources for excellent resolution. Thin film samples are mounted in the SEM under copper tape or upon carbon tape for the LEO 1530 FESEM and the FEI Nova NanoSEM 630, respectively. The LEO has automatic beam deceleration, whereas this feature can be manually employed on the NanoSEM xT microscope control software when necessary. The NanoSEM seen in Figure 2–17 can also be backfilled with water vapor to a low-vacuum mode to help prevent drift from charging samples.

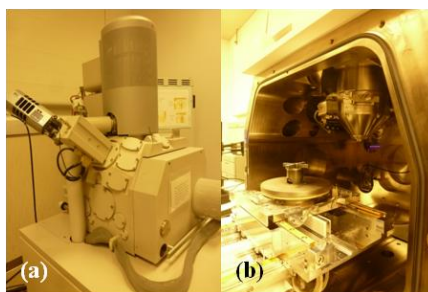


Figure 2–17. (a) The exterior of the FEI NanoSEM 630 used for imaging with the X-ray energy dispersive spectroscopy attachment on the far left; and (b) the interior of the same.

2.3.2.2 X-ray energy dispersive spectroscopy

The NanoSEM can also be used for X-ray energy dispersive spectroscopy (XEDS) using AZtec Software. XEDS involves accelerated electrons ejecting core electrons. In order to relax, another electron from a higher energy level drops into place and a characteristic X-ray is emitted. The transition shown in Figure 2–18 resulted in a $K\alpha$ X-ray due to the energy transition between the L and K energy levels. The dominant transition studied varies with the elements ($K\beta$ and $L\alpha$ X-rays and so forth). The accelerated electrons must have enough energy to excite the atom and cause the characteristic X-ray emission—e.g., the electrons have higher energies than the characteristic X-rays. From these X-rays, the elemental composition present can be determined in a qualitative manner or a more quantitative manner with prepared standards. For some compositions, the X-rays spectral lines from the elements will overlap, making an accurate (semi-)quantification of their presence impossible. The X-rays originate from depths up to microns inside the sample, depending on the incident energy and the sample material; thus, XEDS is not a surface-sensitive technique. XEDS can be performed in point or area mode, as well as elemental mapping. XEDS can also be performed in a transmission electron microscope, with greater spatial certainty [14].

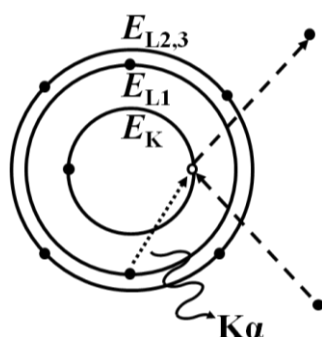


Figure 2–18. Emission of a $K\alpha$ X-ray for XEDS: After the K electron is displaced, the L_2 electron replaces the K electron, leaving the energy difference for the emission of a $K\alpha$ X-ray. *Adapted from [14].*

2.3.2.3 Transmission electron microscopy

A transmission electron microscope (TEM) can provide information about structure, composition, and morphology for thin, electron-transparent cross-sections of samples. Preparing samples for the TEM is unfortunately both destructive and often time-consuming as the samples must be prepared by mechanical polishing and/or using a focused ion beam (FIB) in order to be sufficiently thin (< 100 nm). In mechanical polishing, two thin pieces are cut from the sample using a diamond saw. These slices are then mated together (or one specimen piece to a slice of Si) and adhered with silver epoxy. After the epoxy has cured, the samples are mounted on a polishing tripod or disk apparatus with wax. These samples are then polished on a rotating wheel with diamond papers (South Bay Technology) of varying grit sizes. Starting with the roughest papers, material is removed from the sample in a lapping motion. The diamond papers used ranged from 30 to $0.5\ \mu\text{m}$. Polishing progresses from higher to lower grit specifications as the sample thins, thus producing a well-polished sample surface. The sample is then

attached with epoxy to a TEM grid, 3 mm in diameter. The grids are made of Mo to avoid stray Cu peaks in XEDS. The sample and grid are reattached to the tripod with wax for polishing the other side to a small thickness ($\sim 1 \mu\text{m}$) with a smooth surface. The very thin sample and grid can then be placed in an ion mill. The samples are then chilled and bombarded with Ar ions to produce a small finite hole. In the area around the hole, the sample will be electron transparent for study in the TEM.

Alternatively, when site specific cross-sections are desired, the cross-section can be obtained using a FIB, such as the FEI Quanta 200 3D Dual Beam at PSU. A protective material (C or Pt) is deposited over the area of interest. The ion beam (normally Ga) is then used to sputter away the material around the area of interest. Ultimately, the sample is tilted to cut out the thinned cross-section with the ion beam. An Omniprobe can then be used to lift the cross-section and attach it to a TEM grid with the Pt. Whether mechanical polishing or using the FIB, one must be aware of the damage being caused to the exact sample under examination. Mechanical polishing with progressively finer papers can remove much of the damage caused by rougher papers; however, the ion beam damage from the FIB is harder to remove and may cause amorphization or other undesired effects in samples.

After sample preparation, the TEM grid is loaded into the TEM in stages in order to not disrupt the ultra-high vacuum level. Similar to an SEM, the ultra-high vacuum offers freedom from contamination and a long λ_{mfp} for electrons to interact with the sample. The TEM used in this work was the JEOL 2010F at PSU shown in Figure 2–19, with a minimum resolution of 2 \AA . Electrons from a field-emission gun are accelerated through 200 kV before encountering multiple magnetic lenses and apertures. The beam

must be focused on the electron transparent part of the sample with the sample height adjusted to find the eucentric point. Aligning the electrons to form a parallel beam produces images with diffraction contrast and selected area electron diffraction (SAD) patterns. Through the use of various apertures and lens strength, the direct beam that passed through the sample with minimal interaction and the other electrons diffracted from the sample form a SAD pattern in reciprocal space. In imaging mode, an aperture selects one of the beams from the SAD pattern. Selecting the direct beam forms a bright-field (BF) image, while selecting one of the diffracted beams forms a dark-field (DF) image [45].



Figure 2–19. The JEOL 2010F TEM was used for examining InN samples. *Used with permission from Debangshu Mukherjee.*

The beam can also be tilted while still parallel to the optic axis in order to use scanning transmission electron microscopy (STEM) mode. Images collected in STEM mode can be more sensitive to Z-contrast (elemental) alone using high-angle annular dark-field (HAADF) mode. The scanning nature of STEM also provides the best possibility for atomic resolution. As previously stated, XEDS can also be used in a TEM; specifically, in STEM mode, XEDS can be collected at a specific point or through a

scanning line on imaged areas with a smaller beam size. The 2010F TEM automatically corrects for drift with a reference image during the XEDS scans. The 2010F has a minimum nominal probe size of 1 nm for STEM mode. As samples are both extremely thin and being probed in cross-section, the question of origin depth for XEDS signals can be eliminated in a TEM.

2.3.3 Auger electron spectroscopy

Auger electron spectroscopy (AES) is a destructive, surface-sensitive technique used to study atomic composition. AES involves bombarding a sample with an electron beam that displaces core-shell electrons in the sample up to 1 μm deep. Each resulting core-shell hole is then filled by the transition of another electron to a lower band; and the atom emits a third (Auger) electron from a higher energy level with the energy difference (Figure 2–20). The transitions are named according to the energy shells of the three electrons involved (the displaced electron, the replacement electron, and the Auger electron), such as KLL or LMM. The quantifiable kinetic energy of the emitted Auger electrons can be linked to specific elements. The incident electrons also allow for imaging the sample by secondary electrons in order to find an area of interest. The Auger electrons come strictly from the surface (~ 5 nm) of the sample, since only the electrons that can escape without energy loss or inelastic scattering can be measured [14], [46].

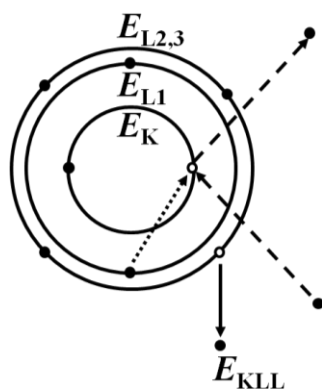


Figure 2–20. Emission of a KLL Auger electron: After the K electron is displaced, the L_2 electron replaces the K electron, leaving the energy difference for the emission of the Auger electron. *Adapted from [14].*

Once loaded into the chamber, the samples are tilted 30° towards the Ar ion gun. The incident accelerated electrons and the analyzer are both located vertically above the sample. After locating the area of interest on the sample using a low beam voltage, the electron beam voltage is then increased depending on what elemental energies need to be detected. Sample current is then used to determine the area of analysis; a lower sample current results in a smaller beam size, but also the need for more data collection scans. A survey scan can provide indication of the elements present, scanning from 30–2030 eV with increments of 0.5 eV/step. An electron energy analyzer collects the Auger electrons according to the intensity signal ($N(E)$) at each kinetic energy. Since Auger peaks are small peaks superimposed on a large background of other energy transitions, the spectra are usually differentiated to show the prominent Auger peaks as $Ed(N(E))/dE$ vs. E .

AES was performed with the RBD Instruments, Inc., refurbished PHI 660 scanning Auger microprobe at GRC seen in Figure 2–21(a). The area of interest was

placed underneath the sunburst holder shown in Figure 2–21(b). For the TLM samples, a finger of the sunburst must be in contact with the TLM mesa which will be investigated by AES, as seen in Figure 2–21(b). After the samples have been grounded and mounted, they were placed in a load lock before insertion into the ultra-high vacuum chamber ($\sim 10^{-9}$ Torr).

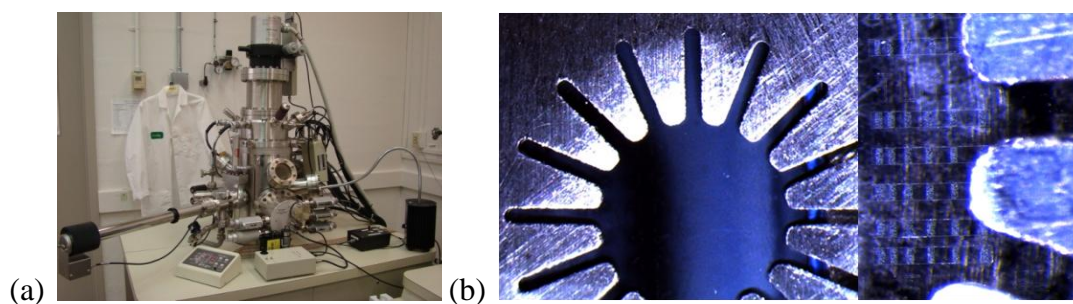


Figure 2–21. (a) The PHI 660 scanning Auger microprobe used for AES analysis along with (b) the sunburst sample holder which must ground the area of interest (inset).

Alternating between electron collection and surface sputtering with an ion beam, depth profiles of the atomic compositions are constructed. For the PHI system, the samples were sputtered using a 3-keV Ar beam for 60 s at a constant rate, corresponding to ~ 100 Å being removed for each cycle. The incident electrons (10 keV) from a LaB₆ filament then displace core-shell electrons to create Auger electrons. During depth profiles, only the elemental regions of interest are analyzed. Combining the peak-to-peak signal of the differentiated peaks ($d(N(E))/dE$) as well as the sensitivity factor of the elements can provide the elemental concentrations of the sample. For some elements, the shape or shift of the peaks can be used to describe the character of the chemical bonding, such as for the C (KLL) peaks seen in Figure 2–22. Auger analysis involves trade-offs

between time, accuracy, area, and intensity. Thus, AES is best used as a semi-quantitative technique due to preferential sputtering and the mixing of various elements [46], [47]. The software used for control and analysis consisted of AugerScan and AugerMap, both from RBD Instruments.

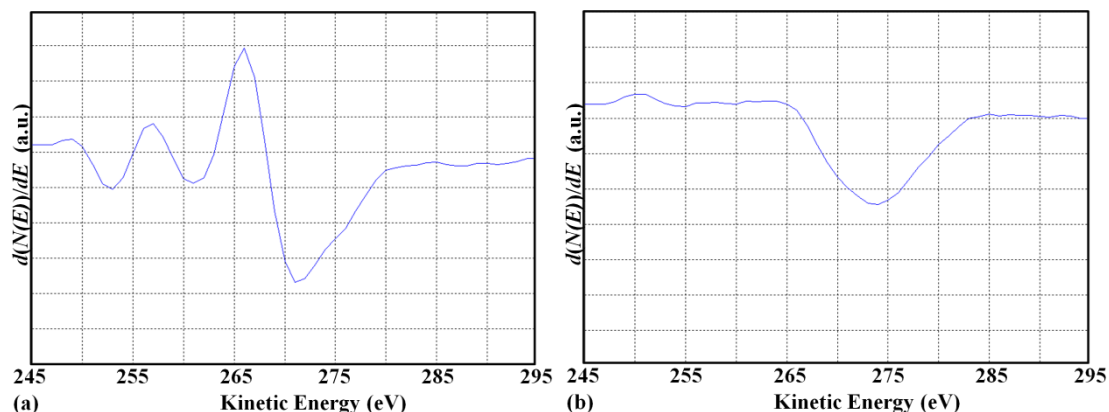


Figure 2–22. Differentiated AES scans of the C (KLL) peak show the distinct peak shapes that reflect the difference in bonding between (a) a metal carbide and (b) non-carbide C.

In addition to pure W as a control, three metal combinations were chosen from Ni-rich W:Ni compositions. The W90:Ni10 and W50:Ni50 targets had been previously obtained from Kurt J. Lesker Company. The W51:Ni49 target previously obtained from Angstrom Sciences was originally believed to be W75:Ni25. This unintentional mistake can be attributed to multiple confusions, including various targets ordered in the same time frame as well as repackaging of all targets for cleanroom cleanliness. Realizing the correct compositions came later in the experimental process. Thin films were sent for independent characterization by X-ray energy dispersive spectroscopy (XEDS) and Rutherford Backscattering Spectroscopy (RBS). RBS involves destructive analysis by

accelerated He ions interacting with the nuclei of the atoms present [31]. The process is quantitative without standards, and especially strong for binary compounds in determining their ratios. X-ray energy dispersive spectroscopy (XEDS) was performed with a 5-keV electron beam and pure metal standards on the deposited films to estimate their compositions within a couple of atomic percent.

The XEDS and RBS analyses were comparable, with a higher emphasis placed on the XEDS results in handling the presence of more than two atomic species (e.g., unexpected oxygen). The manufacturing variations alone between the targets from Kurt J. Lesker Company and Angstrom Sciences resulted in a small spread in composition between the W51:Ni49 and W50:Ni50 film compositions. XEDS analysis of thin films from the W51:Ni49 target showed the actual thin film composition to be W57:Ni43. The W50:Ni50 target resulted in a W52:Ni48 film composition. Films from the W90:Ni10 target were also tested, resulting in a film composition of W93:Ni7. The XEDS results show reasonable agreement with the quoted target compositions. The films from the W51:Ni49 target were found to be a few at.% more W-rich than those from the W50:Ni50 target. The AES sensitivity factors for the tungsten–nickel alloy layers were adjusted from this standard analysis for all W:Ni scans.

Chapter 3

Formation and Aging of Tungsten–Nickel Ohmic Contacts to Silicon Carbide

This chapter discusses ohmic contacts to 4H-silicon carbide, focusing experimentally on simultaneous ohmic contacts using tungsten–nickel alloys. The promising ohmic contact formation results of this chapter have been published in K. C. Kragh-Buetow, R. S. Okojie, D. Lukco, and S. E. Mohny, “Characterization of Tungsten–Nickel Simultaneous Ohmic Contacts to *p*- and *n*-type 4H-SiC,” *Semicond. Sci. Technol.*, vol. 30, 105019 (2015), which should be cited as appropriate. The assistance of Dorothy Lukco is greatly appreciated for her tutelage and guidance in conducting Auger electron spectroscopy.

The quantitative electrical characterization of W:Ni alloy ohmic contacts on *p*-type and *n*-type 4H-SiC is presented. Materials characterization of the crystalline tungsten–nickel–carbide phase and the distinctive surface morphology that formed in these ohmic contacts are also discussed. Further electrical characterization is offered for aging at both 1000 °C+ and 600 °C. Materials characterization is also presented for the possibility of co-sputtered Pt and C on TaSi₂ as diffusion layers.

3.1 Literature on SiC Ohmic Contacts

3.1.1 Background on ohmic contacts to SiC

The demand for electronics and sensors operating at elevated temperatures continues to increase, with interest that includes a variety of industries: automotive, space, power generation, and energy. As previously discussed in Chapter 1, the wide bandgap semiconductor silicon carbide (SiC) has been researched to fulfill many of these expectations. Before SiC can become more widely adopted in high-temperature devices, electrical contact materials for metallization as well as diffusion barriers for elevated temperatures must be improved. The optimum ohmic contact material will have a low contact resistance for a long period of operation, representing ease of carriers moving over a small barrier or through a thin barrier [13], [14]. Ohmic contacts, however, can also be a cause of failure at high temperatures. Consequently, numerous research efforts have investigated metal contacts for *p*-type and *n*-type SiC, mostly with a separate approach to each doping type [4], [9]–[13]. Most contact research has been done on hexagonal polytypes [9], [10], with comparable results generally found for 4H- and 6H-SiC.

High doping levels as well as high-temperature annealing, often at temperatures near or above 900 °C, have both been important for achieving ohmic contacts [9], [10]. As SiC sublimates above 2830 °C, the thermal stability of the metal (and not SiC itself) is an important part of ongoing materials research in ohmic contacts. As previously discussed in Section 1.2, neither the Schottky–Mott relationship nor Fermi-level pinning

has been shown to fully determine ohmic contact formation to SiC. The exploration of metals as ohmic contacts has been consequently conducted on more of a ‘trial-and-error’ basis, using various materials for both *n*-type and *p*-type SiC [12]. Research into contacts on *n*-type SiC has generally resulted in lower specific contact resistance (ρ_c) values than those for *p*-type SiC, with Ni-based contacts to *n*-type SiC most frequently reported in the literature alongside reports of Al-based (e.g., Ti/Al) contacts to *p*-type SiC [4], [9], [10], [13]. The lower resistances found in ohmic contacts to *n*-SiC have caused researchers to focus more attention on reliable ohmic contacts to *p*-type SiC. Due to concerns such as oxidation and volatilization while using Al-based contacts at high temperatures, other materials have also been studied to achieve low ρ_c values ($\sim 10^{-6} \Omega\text{cm}^2$) for *p*-type SiC [10]. In addition to improving the Ni-based contacts for *n*-type SiC and Al-based contacts for *p*-type SiC, researchers have investigated numerous other metals, silicides, carbides, and nitrides with varying results for each conductivity type [9]–[12].

Once cobalt disilicide was found to be ohmic on *n*-type and *p*-type SiC in separate studies [48], [49], the possibility of simultaneous ohmic contact formation using the same contact materials has been pursued. This dissertation sought to investigate tungsten–nickel (W:Ni) alloys as simultaneous ohmic contacts as well as explore the reliability and diffusion barrier challenges that would enable high-temperature SiC devices. W- and Ni-bearing contacts along with outstanding results will be the focus of the subsequent SiC literature sections. Additional history about simultaneous ohmic contact studies will also be included.

3.1.2 Selected review of distinct ohmic contacts to *n*-type and *p*-type SiC

3.1.2.1 Review of Tungsten-bearing ohmic contacts to SiC

Interest in W on SiC started with the high melting point of W at 3400 °C being well-matched to the thermal stability of SiC. Thin films of W upon *n*-3C-SiC, annealed at 850 °C, were reported to form WC and WSi₂ at the interface with $\rho_c \approx 0.24 \text{ } \Omega\text{cm}^2$ [50], [51]. Lower ρ_c values were achieved for W on *n*-3C-SiC after annealing at 300 °C, with $\rho_c \approx 10^{-3} \text{ } \Omega\text{cm}^2$ [52]. Another study on annealing W/*n*-3C-SiC for 1 min between 600–1100 °C indicated the formation of W₅Si₃ and W₂C by X-ray diffraction when the annealing temperature was above 950 °C [53]. The influence of SiC polytype (and bandgap), however, must be considered when translating these results from 3C- to 4H- and 6H-SiC.

Annealing W on both *n*- and *p*-6H-SiC up to 800 °C was found to sustain Schottky contact behavior with no reaction products [54]. W and WN on *n*-4H-SiC were annealed for 4 min at 800 °C, also with rectifying behavior even after 100 h of aging [55]. When W was annealed on *n*⁺-6H-SiC at 1070 °C, the resulting electrical contacts were ohmic with $\rho_c \approx 10^{-6} \text{ } \Omega\text{cm}^2$ [56]. Co-sputtering W and Si resulted in WSi₂ formation and ohmic contacts on *n*-6H-SiC after annealing at 1000 °C with $\rho_c \approx 10^{-5} \text{ } \Omega\text{cm}^2$; the resistance of these contacts increased only one order of magnitude over 150 h at 400 °C in air [57]. W films deposited using a focused ion beam resulted in ohmic contacts to *p*-6H-SiC without annealing, with $\rho_c \approx 10^{-4} \text{ } \Omega\text{cm}^2$; however, Ga was thought to be incorporated into the substrate [58]. Samples from the aforementioned W and WN study were annealed for 4 min at 1200 °C, resulting in the formation of both

W_2C and W_5Si_3 phases as well as the creation of ohmic contacts to n -4H-SiC.

Construction of W–Si–C ternary phase diagrams for 3C-SiC at 1100 °C [53] and for 6H-SiC at 1300 °C [59] had shown W_2C and W_5Si_3 not to be stable phases with SiC. Other researchers generated phase diagrams showing the stable silicide changes from WSi_2 to W_5Si_3 around 700 °C; and W_2C replaces WC as the stable carbide around 1800 °C [60]. Most recently, similar results were obtained for n -4H-SiC, with WC and W_5Si_3 being the stable phases after annealing at 1400 °C [61]. Ohmic contact formation only occurred after annealing at 1400 °C, with the $\rho_c \approx 10^{-5} \Omega\text{cm}^2$ being attributed to WC spiking into the SiC, as seen during interfacial analysis [61].

3.1.2.2 Review of Nickel-bearing ohmic contacts to SiC

Studies of Ni-contacts to n -type SiC have explored electrical properties and the phases formed after annealing at a variety of temperatures [9]–[13], [62]. Ni contacts annealed at 950 °C on 6H-SiC [63] and 4H-SiC [64] reacted to form Ni_2Si with $\rho_c \approx 10^{-6} \Omega\text{cm}^2$; however, substantial carbon accumulation and voiding was observed. Ni/Si layers deposited to encourage Ni_2Si formation had less C accumulation and voids after annealing than pure Ni thin films [64], [65]. Ni_2Si formation was even considered the key factor in achieving ohmic contacts [64] before Ni_2Si was shown to be formed at 600 °C with rectifying properties [66], [67]. A synchrotron study of Ni/ n -4H-SiC also showed the formation at 950 °C of Ni_2Si , $Ni_{31}Si_{12}$, and $NiSi$ [67]. The same study [67] postulated that C out-diffusion from silicide formation resulted in C vacancies acting as donors in SiC ($E_c - 0.5$ eV) and thinning the Schottky barrier to allow current transport by field emission. Removing the Ni_2Si ohmic contact on C-face n -4H-SiC and depositing

a fresh metallization without annealing was found not to alter the electrical properties, thus supporting the C vacancy hypothesis [62]. The use of Ni/Si layered ratios to encourage NiSi₂ formation on Si-face 4H-SiC does not result in ohmic behavior, and ratios that encourage Ni₂Si formation have lower ρ_c with a Si layer deposited first [68].

Further theories have discussed Ni ohmic contact formation to no conclusion. Tanimoto *et al.* [69] found a thin layer of NiSi at the Ni₂Si/*n*-4H-SiC interface after annealing at 1000 °C, with a strong dependence of ρ_c on annealing temperature. Doubting the validity of the C vacancy hypothesis, they suggested that temperatures above 900 °C encourage NiSi formation that lowers the contact resistance [69]. The cause of voiding has been proposed to be the reaction from Ni₃₁Si₁₂ to Ni₂Si [70], [71], making options for reducing the number of voids limited. Investigating a hypothesis that graphite formation at the interface causes ohmic contacts, a C layer was intentionally placed between Ni/Si layers but resulted in no improvement [72].

From the aforementioned studies and beyond, the lowest ρ_c values reported in the literature are $\sim 1 \times 10^{-6} \Omega\text{cm}^2$. The lowest asserted ρ_c value of $< 1 \times 10^{-6} \Omega\text{cm}^2$ was formed after annealing Au/Ni/C-face *n*-6H-SiC at 1000 °C for 5 min in 1995 [73]. The SiC epilayer had exceptionally high *n*-type doping ($N_D = 4.5 \times 10^{20} \text{ cm}^{-3}$) from liquid phase epitaxy [73]. Lower ρ_c values $\sim 10^{-7} \Omega\text{cm}^2$ were reported that same year for Ni annealed to form Ni₂Si on 6H-SiC with more moderate doping; however, the researchers cautioned the accuracy of their methods to $< 5 \times 10^{-6} \Omega\text{cm}^2$ [63]. Such ρ_c values were recently matched in a NiSi interface study at $\sim 1.1 \times 10^{-6} \Omega\text{cm}^2$ for annealed Ni/*n*⁺-4H-SiC with a Ta/TaN/Al-Si protective layer [69]. Other notable results include Ni/*n*-SiC forming contacts with $\rho_c \approx 2.8 \times 10^{-6} \Omega\text{cm}^2$ that showed excellent thermal stability out to

100 h at 500 °C in N₂ [64]. Pt/Ti/WSi/Ni on *n*-4H-SiC demonstrated sustained ohmic behavior (values unreported) through 100 cycles of pulsed thermal testing and 100 h of static thermal testing, both at 650 °C in N₂ [74]. Meanwhile, Ni ohmic contacts with adhesion and capping layers of Pt/TaSi_x resulted in ρ_c rising from 10⁻⁵ Ωcm² to 10⁻⁴ Ωcm² after 300 h+ annealing at 600 °C in air—as long as thicker Pt/TaSi₂ layers were used to prevent oxidation [17].

Other multi-metal schemes of note with Ni on *n*-SiC include Au/Ni:V7%/n-4H-SiC that resulted in $\rho_c \approx 10^{-6}$ –10⁻⁵ Ωcm² after annealing at 1100 °C [75], and Ni/V bilayers that resulted in $\rho_c \approx 10^{-5}$ Ωcm² [76]. Most recently, a six layer stack of Ni, Si, and Zr on *n*-4H-SiC resulted in an amorphous Ni–Zr layer that limits diffusion with $\rho_c \approx 10^{-6}$ Ωcm² for 100 h at 500 °C in Ar [77]. While W reacts with SiC to form silicides and carbides, Ni forms silicides and leaves free carbon. Researchers have viewed the presence of C as both helpful for its conductive nature (graphite) and detrimental as a site for voiding [10]–[12]. An advantage of the metals favored for *p*-SiC (e.g., Al–Ti) has been the ability of Ti to form C-containing phases, limiting atomic diffusion.

3.1.2.3 Review of Titanium-bearing ohmic contacts to SiC

Interest in Al, the common *p*-type dopant for SiC, as a contact material was tempered by its low melting point; thus, Al was an undesirable material unless alloyed with another metal to increase the melting point [9]. The use of Ti with Al seems to provide more reliable ohmic contacts to *p*-type SiC, resulting in a plethora of research into Ti–Al [9], [10], [13]. The first quantitative evaluation of Ti–Al on *p*-6H-SiC reported $\rho_c \approx 10^{-5}$ Ωcm² at $N_A = 2 \times 10^{19}$ cm⁻³ after annealing at 1000 °C [78]. Further

work on Al 90 wt. %:Ti contacts resulted in $\rho_c \approx 10^{-5}$ – $10^{-6} \Omega\text{cm}^2$; however, etch pits were revealed underneath the contacts after the metallization was etched away [79]. Pure Ti contacts demonstrated a highly reproducible $\rho_c \approx 10^{-5} \Omega\text{cm}^2$ without pitting underneath the contacts [79]. Pure Ti contacts were also reported to be stable in the $\rho_c \approx 10^{-5} \Omega\text{cm}^2$ range over 250 h at 500 °C, while Al 90 wt. %:Ti contacts ceased to be ohmic after 24 h [80]. Layers of 375 nm Al/80 nm Ti on *p*-4H-SiC resulted in $\rho_c \lesssim 1 \times 10^{-6} \Omega\text{cm}^2$ after annealing at 1000 °C [81]. The study of Al 70 wt. %:Ti demonstrated a smoother surface, a smaller ρ_c range near $10^{-5} \Omega\text{cm}^2$, and enhanced spiking of the Al into the *p*-SiC as compared to the Al 90 wt. %:Ti alloy [82], [83].

X-ray diffraction studies of Al 69 wt. %:Ti layers on *p*-4H-SiC confirmed the formation of Ti_3SiC_2 , Ti_5Si_3 , and Al_3Ti [84]. The ohmic contact formation was attributed to minimal lattice mismatch between SiC and Ti_3SiC_2 . Notably, Ti_3SiC_2 has a narrower bandgap that could lower the energy barrier to SiC when encountered sequentially [84]. Transmission electron microscopy for annealed 190 nm Al/50 nm Ti/*p*-4H-SiC has shown Ti_3SiC_2 to be a strongly oriented, epitaxial film and the only phase in direct contact with SiC [85]. In many of these studies, Al was thought to elevate the *p*-type doping in the SiC at the interface to assist in Ti–Al ohmic contact formation. This theory was rejected by a study using Auger electron spectroscopy and secondary ion mass spectroscopy that found no Al near the interface [86]. A detailed transmission electron microscopy and density functional theory study [87] further supported the narrow bandgap of Ti_3SiC_2 [84], [85] at the *p*-SiC interface as the explanation for ohmic contact formation. In order to test the role of Ti_3SiC_2 in direct physical contact to 4H-SiC, Ti_3SiC_2 was epitaxially grown on *n*- and *p*-SiC and found to be rectifying [88].

Surprisingly, annealing the $\text{Ti}_3\text{SiC}_2/\text{SiC}$ resulted in ohmic contacts only for $n\text{-SiC}$; the lack of ohmic contact formation to $p\text{-SiC}$ has created further need to explain contact formation [88]. Two separate materials studies investigated the formation sequence of Ti_3SiC_2 by Al–Ti composition and annealing variations [89] and by sputtering Ti at elevated temperatures [90]. Evidence of ohmic behavior was reported only for as-deposited $\text{Ti}_3\text{SiC}_2/n\text{-SiC}$ [90].

Ni/Ti is another layered metal contact being researched for $p\text{-SiC}$ ohmic contacts. Ni/Ti bilayers annealed at 700 °C resulted in Ni_2Si formation and $\rho_c \approx 10^{-5} \Omega\text{cm}^2$ for $p\text{-4H-SiC}$ [91]. Ni with a Ti adhesion layer similarly produced $\rho_c \approx 10^{-5} \Omega\text{cm}^2$ for highly-doped $p\text{-4H-SiC}$ after annealing at 750 °C [92]. Variations on Ni/Ti have also been looked at for $n\text{-SiC}$. Ti/Ni/Ti/ $n\text{-SiC}$ was annealed for 2 min at 1000 °C and formed into TiC and Ni_2Si with $\rho_c \approx 10^{-4} \Omega\text{cm}^2$ [93]. Different layers and ratios of Ti/Ni on $n\text{-SiC}$ resulted in phase formations of Ti_5Si_3 , TiC, and Ni_2Si , as identified using X-ray diffraction [94], with layer order being irrelevant [95]. Several further studies of Ni/Ti on both $n\text{-6H-}$ and $n\text{-4H-SiC}$ have used X-ray diffraction for varying annealing conditions and found the only crystalline phase to be Ni_2Si , although with depth profile evidence of TiC [96]–[99].

Combined schemes of Ti/Al and Ni/Ti have also been studied as Ni/Ti/Al layers on $p\text{-SiC}$. Al/Ti/Ni on $p\text{-4H-SiC}$ had been shown to have similar Ti_3SiC_2 formation to Al/Ti contacts with $\rho_c \approx 7 \times 10^{-5} \Omega\text{cm}^2$ [85]. Various Ni/Ti/Al layer thicknesses were evaporated onto $p\text{-4H-SiC}$ and annealed for 90 s at 800 °C; the best ρ_c obtained was $\approx 1.5 \times 10^{-5} \Omega\text{cm}^2$ [100]. Another study fabricated as-deposited Ni/Al/Ti/Ni ohmic contacts on a vapor–liquid–solid grown $p\text{-SiC}$ layer; the minimum ρ_c was $\approx 1.3 \times 10^{-6} \Omega\text{cm}^2$ after

annealing at 800 °C [101]. Recently, Al/Ti/Ni contacts on *p*-4H-SiC were shown to be thermally stable with $\rho_c \approx 10^{-5} \Omega\text{cm}^2$ after 100 h annealing at 600 °C in N₂ and only a modest increase in surface roughness [102].

3.1.3 Review of simultaneous ohmic contacts to SiC

In the above literature review, most of the focus has been on one conductivity type: *n*-type for Ni and W; and *p*-type for Ti–Al and Ni–Ti–Al. While Ti–Ni and a brief W study [58] achieved ohmic contacts to both *n*- and *p*-SiC, the processing conditions were generally not comparable. This dichotomy in promising results has lead to fabricating separate ohmic contact metals to bipolar devices. These separate approaches further complicate the process flow with the need to protect the first contacts during fabrication of the second set—such protective materials then must be removed later without contact damage. With separate materials and annealing temperatures, process flow must involve considerable complexity. Alternatively, being able to use the same contact material for both *p*-type and *n*-type SiC would provide a valuable reduction in the number of microfabrication steps [103].

Simultaneous ohmic contacts to both *n*-type and *p*-type SiC have been studied occasionally, with dedicated research interest in the 21st century. Brief mentions of ohmic contact formation to both doping types can be found in 1958 for W annealed at 1900 °C [104], in 1969 for a Cu–Ti eutectic after a capacitor was discharged [105], and in 1995 for Ti/Al [73]—all without ρ_c quantification. Once CoSi₂ was found to be ohmic on *n*- and *p*-6H-SiC ($N_D = 1.4 \times 10^{19} \text{ cm}^{-3}$, $\rho_c \approx 10^{-5} \Omega\text{cm}^2$; $N_A = 2 \times 10^{19} \text{ cm}^{-3}$, $\rho_c \approx$

$10^{-6} \Omega\text{cm}^2$) in separate studies during the 1990s [48], [49], simultaneous ohmic contact formation on SiC became deliberately pursued. Co-evaporation of TiC contacts at 500 °C onto 4H-SiC resulted in as-deposited ohmic contacts to both *p*- and *n*-SiC ($N_A > 10^{20} \text{ cm}^{-3}$; $N_D = 1.3 \times 10^{19} \text{ cm}^{-3}$) without the need for another high-temperature, post-deposition anneal [106]. After the pre-anneal during deposition, the as-deposited ρ_c to *p*-SiC was $\sim 10^{-4} \Omega\text{cm}^2$, while ρ_c to *n*-SiC was $\lesssim 10^{-6} \Omega\text{cm}^2$; however, these values converged to $\rho_c \approx 10^{-5} \Omega\text{cm}^2$ after annealing for 180 s in H_2/Ar at 950 °C [106].

More concentrated interest in simultaneous ohmic contact formation resulted in $\rho_c \approx 10^{-4} \Omega\text{cm}^2$ on *p*-4H-SiC ($N_A \approx 10^{21} \text{ cm}^{-3}$) and $\rho_c \approx 10^{-6} \Omega\text{cm}^2$ on *n*-4H-SiC ($N_D \approx 10^{19} \text{ cm}^{-3}$) for Ni annealed at 1050 °C [103]. Another study of Ni annealed at 1000 °C resulted in contacts to *p*-SiC ($N_A \approx 2 \times 10^{20} \text{ cm}^{-3}$) with $\rho_c \approx 10^{-3} \Omega\text{cm}^2$ and to *n*-SiC ($N_D \approx 2 \times 10^{20} \text{ cm}^{-3}$) with $\rho_c \approx 10^{-6} \Omega\text{cm}^2$ [81]. Using sputtered TiW as ohmic contacts resulted in $\rho_c \approx 10^{-5} \Omega\text{cm}^2$ to both doping types ($N_D = 1.3 \times 10^{19} \text{ cm}^{-3}$; $N_A = 6 \times 10^{18} \text{ cm}^{-3}$); although a large variability exists in ρ_c for small changes in surface acceptor concentrations [107]. Different layer thicknesses of Al/Ti/Ni were tested at a fixed Ni/(Ni+Ti) ratio = 0.39; however, only 39 at.% Al resulted in simultaneous ohmic contacts on *p*-SiC ($N_A = 4.5 \times 10^{18} \text{ cm}^{-3}$; $\rho_c \approx 10^{-3} \Omega\text{cm}^2$) and *n*-SiC ($N_D = 1.0 \times 10^{19} \text{ cm}^{-3}$; $\rho_c \approx 10^{-4} \Omega\text{cm}^2$) after annealing at 800 °C [108].

With the common use of Ti/Al for *p*-SiC and Ni for *n*-SiC, two separate studies intentionally explored these materials for the opposing conductivity types in 2006. While the use of Au/Ti/Al/Ti on *n*-6H-SiC resulted in $\rho_c \approx 10^{-6} \Omega\text{cm}^2$, no matching *p*-type results were presented [109]. Ni films were studied on both epitaxial and implanted *p*-4H-SiC with widely varying $\rho_c \approx 10^{-6} - 10^{-4} \Omega\text{cm}^2$ for high doping [110]. These two

studies are included in this section reviewing simultaneous contacts; however, these studies did not present results for intentional side-by-side comparison with similar processing like the other studies of simultaneous ohmic contacts.

Simultaneous ohmic contact formation for Al/50 nm Ni on 4H-SiC occurred only for a limited range of Al thicknesses that corresponded to a small $\text{Ni}_2\text{Si}(\text{Al})$ grain size [111]. A further study by the same group clarified the acceptable compositional range to be 3 at.% Al in Ni/Al with $\rho_c \approx 10^{-4} \Omega\text{cm}^2$ for both doping types ($N_D = 1.3 \times 10^{19} \text{ cm}^{-3}$; $N_A = 7.2 \times 10^{18} \text{ cm}^{-3}$) [112]. In 2010 ohmic contacts using W:Ni alloys in a 1:1 atomic ratio exhibited specific contact resistances of $\rho_c \approx 10^{-5} \Omega\text{cm}^2$ on n -6H-SiC ($N_D > 2 \times 10^{19} \text{ cm}^{-3}$) and $\rho_c \approx 10^{-4} \Omega\text{cm}^2$ on both p -6H-SiC ($N_A > 1 \times 10^{20} \text{ cm}^{-3}$) and n -4H-SiC ($N_D > 2 \times 10^{19} \text{ cm}^{-3}$), with qualitative proof for p -4H-SiC ($N_A > 2 \times 10^{19} \text{ cm}^{-3}$) as well [113]. After annealing varying Si/Al/Ti thicknesses at 1020 °C, optimized ohmic contacts were achieved on both p -SiC ($N_A = 2.4 \times 10^{19} \text{ cm}^{-3}$; $\rho_c \approx 10^{-4} \Omega\text{cm}^2$) and n -SiC ($N_D = 2.6 \times 10^{19} \text{ cm}^{-3}$; $\rho_c \approx 10^{-6} \Omega\text{cm}^2$) [114]. Ni/Ti bilayers on both doping types ($N_{D,\text{MAX}}$ and $N_{A,\text{MAX}} = 1.0 \times 10^{20} \text{ cm}^{-3}$) demonstrated smoother morphology than Ni contacts while also being less sensitive to interfacial oxidation when forming ohmic contacts by annealing, albeit with $\rho_c \approx 10^{-3} \Omega\text{cm}^2$ on p -4H-SiC [115]. More recently, annealed Ni/SiC contacts that formed Ni_2Si remained stable ohmic contacts when aged for 95 h in N_2 at 400 °C with $\rho_c \approx 10^{-4} \Omega\text{cm}^2$ ($N_D = 3 \times 10^{20} \text{ cm}^{-3}$) for n -4H-SiC and $\rho_c \approx 10^{-3} \Omega\text{cm}^2$ ($N_A = 1 \times 10^{20} \text{ cm}^{-3}$) on p -4H-SiC [116]. Al/Ti/Ni was also recently revisited with different thicknesses after annealing at 950 °C, which resulted in $\rho_c \approx 10^{-5} \Omega\text{cm}^2$ ($N_D = 1 \times 10^{19} \text{ cm}^{-3}$; $N_A = 2 \times 10^{19} \text{ cm}^{-3}$), albeit with some spread in values [117].

These results from the side-by-side studies have been plotted for the average ρ_c values (median for [115]) vs. the best reported value for doping concentration in Figure 3–1. In many of these previous studies, the ρ_c values between p -SiC (filled symbols) and n -SiC (open symbols) are clearly disparate, as seen in Figure 3–1. These results leave a desire still for simultaneous contacts with comparable electrical behavior for 4H-SiC.

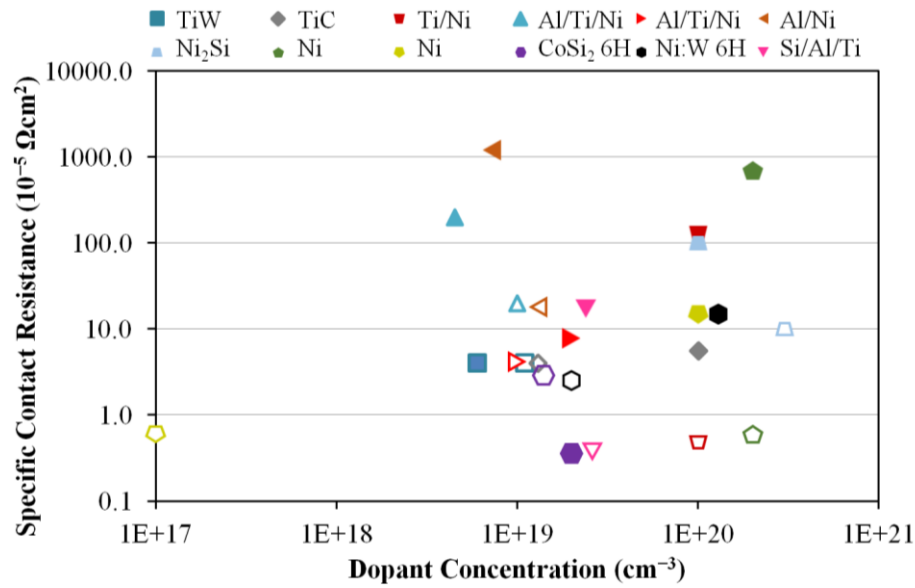


Figure 3–1. Specific contact resistance (ρ_c) values for simultaneous ohmic contacts from the literature plotted against the dopant concentrations in the SiC epilayers. Open symbols are ohmic contacts to n -SiC and filled symbols are ohmic contacts to p -SiC.

3.1.4 Review of W–Ni thin films in electronics

This work sought to expand the W:Ni simultaneous ohmic contact study from 6H-SiC [113] to 4H-SiC and to better understand the contact behavior, especially for p -SiC. The W:Ni contacts are a desirable bimetal combination that could possibly serve as a refractory metal alloy for high-temperature applications without involving Al. The

formation of high work function W_xC_y on p -type and Ni_xSi_y on n -type SiC was postulated to explain the W:Ni ohmic behavior for both conductivities [113]. This research also presents materials characterization of the phases formed. Previous research on electronic devices using W and Ni thin films has been limited, as reviewed below.

Alloyed W:Ni thin films can be found in the earlier literature on Si technology. Amorphous $Ni_{36}W_{64}$ thin films being researched as diffusion barriers displayed crystalline phase formations of NiSi and NiSi₂ at 500 °C and WSi₂ at 625 °C [118]. A different study into W–Ni ion mixing between 650–850 °C on Si substrates indicated formation of WSi₂ and an unknown ternary phase from W-rich co-sputtered alloys [119]. Contrasting Ni and W sequential layers on Si and SiO₂ that were annealed at the same temperatures demonstrated the formation of nickel silicides and tungsten silicides on Si but no silicide formation on SiO₂ [120].

Thin film research involving both W and Ni on SiC has been primarily carried out at two locations: the NASA Glenn Research Center (GRC) and the University of Dayton/Wright Patterson Air Force Base (UD/WP). The UD/WP group often included additional metals in the W–Ni layers in their research. Prior research into solely W–Ni thin films on SiC mentioned formation of ohmic contacts using W/Ni/ α -SiC for both n -SiC [121] and p -SiC [122] without clear indication of ρ_c values. The W/Ni/ p -SiC was further noted as stable over 1098 h at 400 °C [122]. W/Al/Ni/ p -SiC was annealed in the same study with $\rho_c \approx 10^{-4} \Omega\text{cm}^2$ for 1098 h [122]. Further demonstration of excellent thermal stability was later seen for W/Al/Ni annealed over 1000 h at 600 °C in vacuum [123]; however, these contacts degraded much faster in air for various capping layers [123]. Various thicknesses of W/AlNi/Ti/ p -4H-SiC were also explored to form contacts

with $\rho_c \approx 10^{-4} \Omega\text{cm}^2$ [124], [125]. On *n*-6H-SiC, Ni/Ti/W contacts were reported to exhibit $\rho_c \approx 10^{-3} \Omega\text{cm}^2$ through 100 h at 400 °C [126]. Annealed Ni/Cr/W contacts formed Ni₂Si and Cr₃C₂ with $\rho_c \approx 10^{-4} \Omega\text{cm}^2$, even after 3000 h of annealing in vacuum at 650 °C [127]. The previously mentioned Pt/Ti/WSi/Ni ohmic contacts on *n*-SiC [74] at the Army Research Lab were also promising but unquantified. The NASA GRC group was responsible for the aforementioned W:Ni/6H-SiC simultaneous study [113]. In another GRC paper, a W:Ni composition was ohmic over 15 h of aging at 1000 °C on *n*-4H-SiC and *n*-6H-SiC ($N_D \approx 5\text{--}7 \times 10^{18} \text{ cm}^{-3}$) with $\rho_c \approx 5 \times 10^{-4} \Omega\text{cm}^2$ [5].

3.2 Tungsten–Nickel Simultaneous Ohmic Contacts to 4H-SiC

In this section, the experimental results are presented from the study of simultaneous contacts to *p*- and *n*-SiC. W:Ni thin films on both *p*- and *n*-4H-SiC display simultaneous ohmic contact behavior with commensurate ρ_c values. The comparable ρ_c values $\sim 10^{-6}\text{--}10^{-5} \Omega\text{cm}^2$ for W:Ni alloys to both *p*- and *n*-4H-SiC are also lower than other studies for simultaneous contacts seen in Figure 3–1 on both conductivity types. Both structural and compositional materials characterization were performed on the phases formed after annealing.

3.2.1 Experimental procedures for contacts to *p*- and *n*-SiC

Inspired by the first look at W:Ni alloys for *p*- and *n*-type 6H-SiC [113], the preliminary investigations of this work sought to quantitatively measure the ρ_c for W:Ni

ohmic contacts on *p*-type 4H-SiC. As previously discussed, low resistance ohmic contacts on *p*-type 4H-SiC remain of significant scientific interest for devices. Linear transfer length measurement (TLM) test structures were fabricated to study the W:Ni ohmic contacts on 4H-SiC. The variables studied, and listed in Table 3–1, included doping level (and epilayer thickness), W:Ni composition, and annealing temperature. Semi-insulating Si-face (0001) 4H-SiC wafers were obtained from Cree, Inc. (Durham, North Carolina) with *p*-type homoepitaxial layers grown by chemical vapor deposition. The epilayers had acceptor concentrations ranging from 2×10^{19} – 3×10^{20} cm⁻³ as seen in Table 3–1. The nominal metal compositions (atomic percent) consisted of W, W90:Ni10, W51:Ni49, and W50:Ni50. Pure W was included in the *p*-SiC study as a control for studying the influence of Ni on ohmic contact formation.

Table 3–1. Variables considered in the W:Ni TLM structures on <i>p</i> -type 4H-SiC.		
<i>p</i> -type Epilayer Concentration (N_A) and Thickness	Nominal Target Composition	Annealing Temperature
2×10^{19} cm ⁻³ ; 3.9 μ m	W	1000 °C
$> 2 \times 10^{19}$ cm ⁻³ ; 2 μ m	W90:Ni10	1100 °C
7×10^{19} cm ⁻³ ; 2 μ m	W51:Ni49	1150 °C
3×10^{20} cm ⁻³ ; 0.5 μ m	W50:Ni50	1200 °C

TLM test structures were fabricated in ~ 1 cm² pieces with each of the four metal compositions on each of the four epilayers. The contact metals were sputtered from pure W and W:Ni alloy targets, with all purities listed by the manufacturers as 99.9% or higher. After sputtering the W or W:Ni films (~ 180 nm) for constant power and time, a

thin Si cap (7 nm) was sputtered before breaking vacuum to limit premature oxidation. Samples consisting of blanket, unpatterned thin films were also prepared for materials characterization with the same Si caps in place as on the TLM contacts. The blanket thin film samples were deposited on the SiC epilayer that was 2 μm with $N_A > 2 \times 10^{19} \text{ cm}^{-3}$.

X-ray energy dispersive spectroscopy (XEDS) was performed on several as-deposited films, using standards to estimate their film compositions within a couple of atomic percent. The nominal W51:Ni49 films were found to be a few at.% more W-rich than the nominal W50:Ni50 films, as seen in Table 3–2. The most promising results in this work stem from these two compositions with near atomic parity, W51:Ni49 and W50:Ni50. These two compositions will be referred to by their nominal atomic compositions, while acknowledging the small differences that arise from the spread in film compositions. Thus, only W51:Ni49 and W50:Ni50 contacts were separately fabricated on pieces of a semi-insulating Si-face (0001) SiC wafer with 2 μm of n -type epilayer with $N_D = 2 \times 10^{19} \text{ cm}^{-3}$. The electrical results on each epilayer were quite comparable despite the ~5 at.% spread between measured film compositions, which provide support for the robustness of the processes discussed in ohmic contact formation.

Table 3–2. Target and film compositions of the W:Ni alloys.		
<i>Nominal Target Atomic Composition</i>	<i>Nominal Target Weight Composition</i>	<i>Actual Film Atomic Composition</i>
W90:Ni10	W97:Ni3	W93:Ni7
W51:Ni49	W75:N25	W57:Ni43
W50:Ni50	W76:Ni24	W52:Ni48

The 16 TLM squares ($\sim 1 \text{ cm}^2$) on p -SiC were diced into quarters for annealing at four temperatures: 1000 °C, 1100 °C, 1150 °C, and 1200 °C. The sample variables enumerated in Table 3–1 resulted in 64 initial TLM samples. Annealing of the samples was conducted in a dedicated tube furnace, using ultra-high purity Ar gas at 5 slpm. Peak annealing temperatures of 1000 °C, 1100 °C, 1150 °C, and 1200 °C were achieved after 0.75–1 h of ramp time and lasted 0.5 h in duration. The samples were loaded and extracted at 150 °C, with a cross-over to 5 slpm ultra-high purity N_2 gas upon cooling below 600 °C.

The TLM structures were used for electrical and material characterization, with details given in Sections 2.2 and 2.3. Current–voltage measurements were obtained between two consecutive TLM contacts pads using a four-probe configuration in order to obtain resistance, with sourcing conditions limited to $\pm 0.01 \text{ A}$. A linear fit ($R^2 > 0.99$) of resistance vs. gap spacing as seen in Figure 3–2 provided the transfer length (L_T) and sheet resistance (R_{sh}), from which the specific contact resistance $\rho_c = R_{sh}L_T^2$ was calculated [14].

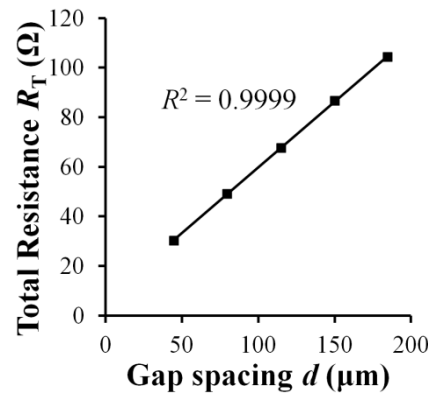


Figure 3–2. The resistances were plotted vs. gap spacing with a high goodness of fit (R^2) in order to obtain the ρ_c value, as shown for W50:Ni50/ n -SiC.

Multiple techniques were used to characterize the annealed W:Ni alloys on SiC, as detailed in Section 2.3. X-ray diffraction (XRD) using the Rigaku DMAX-Rapid II microdiffractometer enabled structural identification of the phases present in the annealed blanket thin film samples. XEDS on the annealed TLM contacts was conducted using the FEI NanoSEM 630 FESEM at 5 kV with image-locking to limit spatial drift as well as AZtec software in point and ID, and map modes. Using a RBD Instruments refurbished PHI 660 scanning Auger microprobe, Auger electron spectroscopy (AES) depth profiles were collected with a 10-keV electron beam. Samples were sputtered for 60 s at a constant rate, corresponding to removal of ~ 100 Å before sweeping C (KLL), O (KLL), Si (LMM), Ni (LMM), and W2 (MNN) Auger elemental windows.

3.2.2 Electrical characterization results and discussion

The electrical current–voltage (I – V) measurements from the as-deposited TLM patterns mostly displayed rectifying behavior between the adjacent contacts. For the W90:Ni10 composition on the 0.5 μm epilayer with the highest p -type acceptor concentration of $3 \times 10^{20} \text{ cm}^{-3}$, only the sample annealed at 1000 °C displayed ohmic behavior; the remaining W90:Ni10 samples and all of the W samples were rectifying post-anneal. For the highest p -type doping concentration, the nominal W51:Ni49 and W50:Ni50 contacts displayed ohmic behavior at all four annealing temperatures. The lowest p -type doping concentration of $2 \times 10^{19} \text{ cm}^{-3}$ demonstrated ohmic behavior as well for the W51:Ni49 samples composition after all temperatures. The addition of

10 at.% Ni to W did not strongly affect the electrical results or the identified phases when compared to W, making the W51:Ni49 and W50:Ni50 compositions of greater interest.

Duplicate samples were fabricated only for the W51:Ni49 and W50:Ni50 compositions on all four *p*-type epilayers in order to clarify these results. In the second set of *p*-SiC samples, the as-deposited TLM structures were not ohmic. The ohmic results from the annealed samples with $N_A = 2 \times 10^{19} \text{ cm}^{-3}$ were not reproducible. Only the TLM structures made from the highest *p*-type doping concentration demonstrated ohmic behavior post annealing. These ρ_c values for the highest *p*-type doping concentration were compared with those from the *n*-SiC as an evaluation of W:Ni alloys on 4H-SiC as simultaneous ohmic contacts. The *n*-SiC contacts, like the second set of *p*-SiC contacts, were ohmic only post-annealing.

Initial extractions of ρ_c from the *p*-SiC TLM structures showed huge spreads (e.g., over two orders of magnitude in values) on the epilayers with the highest doping. These huge spreads demonstrated the importance of minimizing any artifacts due to the metal sheet resistance [35]. The probes must be placed as close to collinear as possible, with the voltage probes nearest to the gap and the current probes at the far ends of the contact lengths (Figure 2–10(a)). Great care was taken in re-measuring the *p*-SiC samples as well as measurements of all other samples. The ρ_c values reported for contacts to *p*-SiC annealed at 1000 °C and 1200 °C come from the second set of samples. The *p*-SiC samples from the second set annealed at 1100 °C and 1150 °C unfortunately experienced oxidation; while these contacts were still ohmic, the fits for extracting ρ_c were no longer (sufficiently) linear. Thus, the ρ_c values from the re-measured first set are used here.

Two sets of TLM samples had been fabricated for *n*-SiC; however, one sample for each

composition demonstrated widespread small surface defects over most of the sample.

The ρ_c values for *n*-SiC are reported from the cleaner surface for the samples annealed at 1000 °C and 1100 °C, although most values were comparable. Only TLM structures from the cleanest location on the ‘spotted’ samples were annealed at 1150 °C, and these values are presented with full confidence.

The resulting measurements for the simultaneous ohmic contacts to *p*- and *n*-SiC displayed a modest range in values. The range for most of the post-annealed ohmic contacts is $\rho_c \approx 10^{-6}$ – 10^{-5} Ωcm^2 for 8–15 test structures per sample, as can be seen in the boxplot of Figure 3–3. The ρ_c values exhibit a finite spread, shown as the box ranging between the 1st and 3rd quartiles (25th and 75th percentiles) with the median value as the line in the box. Lines extend to the maximum and minimum values, which are smaller here than $1.5 \times$ the interquartile range (e.g., the box length). The average values are superimposed as plus signs. The average ρ_c with the standard error, herein defined as standard deviation (σ) divided by the square root of the number of samples (N), can be seen for each sample in Table 3–3.

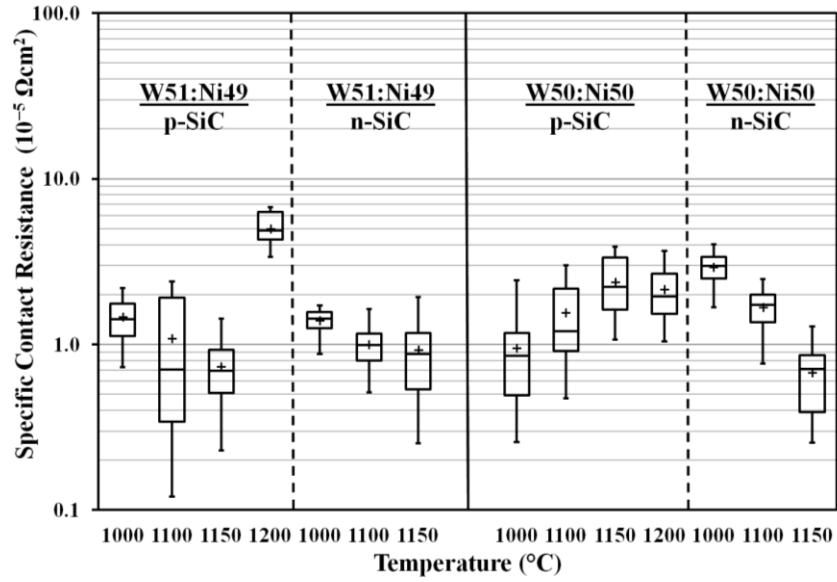


Figure 3–3. Specific contact resistance as a function of annealing temperature for W:Ni contacts on *p*-SiC with $N_A = 3 \times 10^{20} \text{ cm}^{-3}$ and *n*-SiC with $N_D = 2 \times 10^{19} \text{ cm}^{-3}$. The boxplot shown has the averages marked with plus signs.

Table 3–3. Average specific contact resistance ρ_c \pm standard error (σ/\sqrt{N}) in Ωcm^2 . Annealing time was 0.5 h in Ar. Shaded conditions show comparable values.				
	W51:Ni49	N	W50:Ni50	N
1000 °C	$(1.5 \pm 0.1) \times 10^{-5} \text{ p}$	13	$(9.5 \pm 1.6) \times 10^{-6} \text{ p}$	13
	$(1.4 \pm 0.1) \times 10^{-5} \text{ n}$	15	$(2.9 \pm 0.2) \times 10^{-5} \text{ n}$	14
1100 °C	$(1.1 \pm 0.3) \times 10^{-5} \text{ p}$	11	$(1.5 \pm 0.2) \times 10^{-5} \text{ p}$	13
	$(1.0 \pm 0.1) \times 10^{-5} \text{ n}$	15	$(1.7 \pm 0.1) \times 10^{-5} \text{ n}$	15
1150 °C	$(7.3 \pm 0.9) \times 10^{-6} \text{ p}$	13	$(2.4 \pm 0.4) \times 10^{-5} \text{ p}$	8
	$(9.2 \pm 1.3) \times 10^{-6} \text{ n}$	14	$(6.8 \pm 0.9) \times 10^{-6} \text{ n}$	13
1200 °C	$(5.0 \pm 0.3) \times 10^{-5} \text{ p}$	13	$(2.1 \pm 0.3) \times 10^{-5} \text{ p}$	11

For the nominal W51:Ni49/*p*-SiC, the samples annealed at 1100 °C and 1150 °C demonstrated lower ρ_c values compared to the other temperatures. The nominal W50:Ni50 contacts to *p*-SiC show a small upward trend in ρ_c with increasing temperature. The lowest average ρ_c for contacts to *p*-SiC was $(7.3 \pm 0.9) \times 10^{-6} \Omega\text{cm}^2$, occurring with the W51:Ni49 composition annealed at 1150 °C. The ohmic contacts to *n*-SiC showed a decreasing average ρ_c with increasing annealing temperature for both compositions. The lowest average ρ_c value for contacts to *n*-SiC was $(6.8 \pm 0.9) \times 10^{-6} \Omega\text{cm}^2$, occurring with the W50:Ni50 composition also annealed at 1150 °C. The ρ_c values for these compositions on both doping types exhibit highly comparable values in the high $10^{-6} \Omega\text{cm}^2$ to low $10^{-5} \Omega\text{cm}^2$ ranges. The formation of low ρ_c ohmic contact values occurs for both compositions, even with the modest variations in the actual W:Ni ratios in the deposited films. For each pair of W51:Ni49 samples as well as the W50:Ni50 pair annealed at 1100 °C (shaded in Table 3–3), the ρ_c is nearly the same on both doping types, unlike many previous simultaneous ohmic contact studies mentioned in Section 3.1.3. The matched ρ_c values from the W51:Ni49 samples annealed at 1150 °C and the W50:Ni50 samples annealed at 1100 °C have been added to the plot of simultaneous ohmic contacts in Figure 3–4. As conductivity pairs, the W:Ni contacts on 4H-SiC have the lowest ρ_c values that are also comparable values. The W51:Ni49 samples annealed at 1000 °C and 1150 °C have been omitted to not clutter the chart with their placements in between the plotted values from this dissertation.

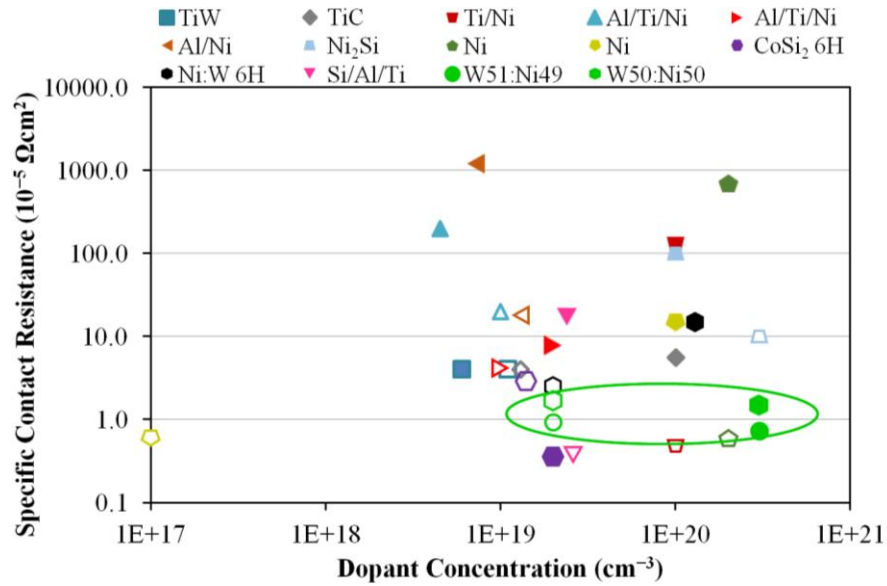


Figure 3–4. Simultaneous ohmic contact ρ_c values plotted against the dopant concentrations in the SiC epilayers. Values from W51:Ni49 samples annealed at 1150 °C and W50:Ni50 samples annealed at 1100 °C have been added to Figure 3–1, showing their similar ρ_c values for both conductivity types. The open symbols are ohmic contacts to *n*-SiC and the filled symbols are ohmic contacts to *p*-SiC.

At all doping levels, some samples that displayed ohmic behavior failed to provide linear R_T vs. d plots. As mentioned previously for some of the contacts to *p*-SiC, these samples demonstrated the difficulty and importance of preventing oxygen exposure, especially in samples annealed at 1200 °C. With the presence of oxygen, possibly due to insufficient Ti gettering of the Ar gas, the formation of nickel tungstate (NiWO_4) was identified by Bragg–Brentano XRD and GIXRD in the blanket thin film samples. This finding was especially common for the more W-rich films from the nominal W51:Ni49 composition when exposed to oxygen. The formation of the nickel tungstate is likely the

reason behind the much higher ρ_c values for W51:Ni49/*p*-SiC annealed at 1200 °C seen in Figure 3–3 and Table 3–3, making this condition an outlier amongst the largely similar ρ_c values. Because of this difficulty in annealing without oxidation for *p*-SiC, the *n*-SiC samples were not annealed at 1200 °C.

3.2.3 Materials characterization results and discussion

3.2.3.1 X-ray diffraction

The phases formed upon annealing between the W or W:Ni alloys and the SiC substrates were studied with XRD, using the microdiffractometer on blanket thin film samples. Only W and SiC were identified from as-deposited samples with XRD (not shown). The clearly identified phases for annealed W or W:Ni/*p*-SiC are summarized in Table 3–4, with discussion to follow. The samples that formed ohmic contacts have the shaded background in Table 3–4. Upon annealing temperatures of 1100 °C and above, the diffraction patterns from the W samples displayed the formation of W₅Si₃ and then W₂C at 1150–1200 °C, as seen in Figure 3–5. These results were in agreement with previous results found by Kakanakova-Georgieva *et al.* [55] for W on *n*-4H-SiC annealed at 1200 °C and were similar to the results of Baud *et al.* [53] for W on *n*-3C-SiC annealed above 950 °C. The phases identified in W90:Ni10 samples were similar to those from the W samples, displaying W₅Si₃ and W₂C, as well as several peaks for a tungsten–nickel–carbide ternary phase, as shown in Figure 3–6 by the peaks marked with circles. The plot shown in Figure 3–6 is representative of W90:Ni10 samples at all annealing conditions.

Table 3–4. Summary of phases identified from XRD.				
Shaded boxes are ohmic conditions.				
	1000 °C	1100 °C	1150 °C	1200 °C
W	W	W, W ₅ Si ₃	W, W ₅ Si ₃ , W ₂ C	
W90:Ni10	W, W ₅ Si ₃ , W ₂ C, W _x Ni _y C	W, W ₅ Si ₃ , W ₂ C, W _x Ni _y C		
W51:Ni49 & W50:Ni50	W _x Ni _y C		W _x Ni _y C, WC	

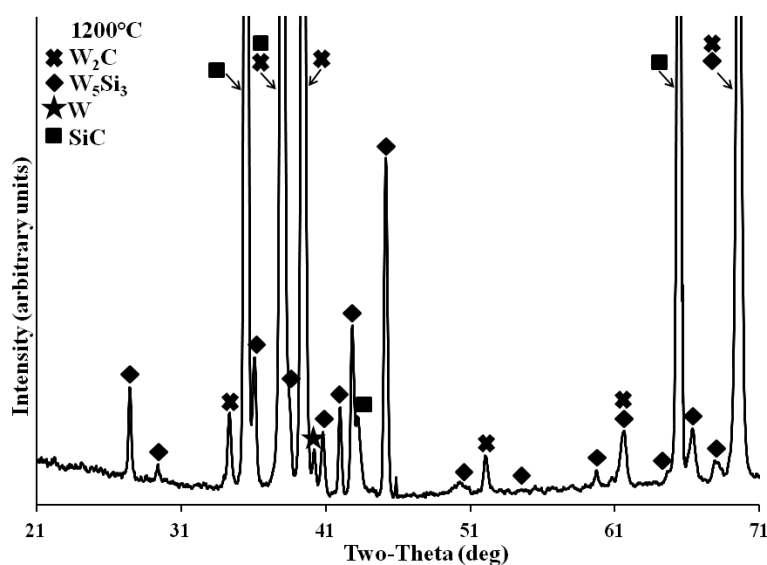


Figure 3–5. Microdiffractometer XRD plot for W/*p*-SiC annealed for 0.5 h at 1200 °C, showing W_5Si_3 and W_2C along with SiC and residual W.

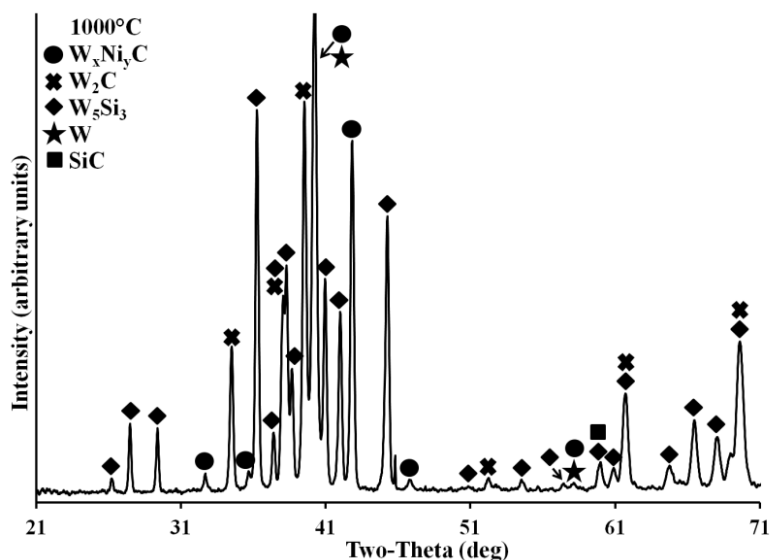


Figure 3–6. Microdiffractometer XRD plot for W90:Ni10/*p*-SiC annealed for 0.5 h at 1000 °C, showing the presence of W_xNi_yC in addition to W_5Si_3 and W_2C .

The W51:Ni49 and W50:Ni50 diffraction patterns from samples annealed at all temperatures featured at least one cubic phase with the space group $Fd\bar{3}m$ and composition W_xNi_yC [128]. Two possible compositions of W_xNi_yC with slightly different lattice parameters have previously been reported in the literature [128]. W_4Ni_2C ($cF112$) and W_6Ni_6C ($cF104$) have similar crystal structures with lattice constants of 11.23 Å and 10.90 Å, respectively. These structures share Wyckoff positions with W on 48f, and with W and Ni sharing occupancy on 32e and 16c in W_4Ni_2C , rather than Ni alone as in W_6Ni_6C . Only the C atoms change locations completely, and this change has little influence on the XRD peak intensities. These highly similar crystal structures for W_4Ni_2C and W_6Ni_6C can be seen in Figure 3–7. Simulated diffraction patterns from the two compositions are shown in Figure 3–8, demonstrating the relative peak positions are

lateral displacements due to the different lattice parameters. The intensities vary due to the structure factor difference between W and Ni. Distinguishing between these two structures has proven difficult. The lattice parameter suggested by the XRD patterns falls between the two, and it might be shifted due to strain or variation in the composition of the thin film phase relative to the bulk. Therefore, W_xNi_yC will be used in this work to designate the experimental structure that corresponds to one of these phases.

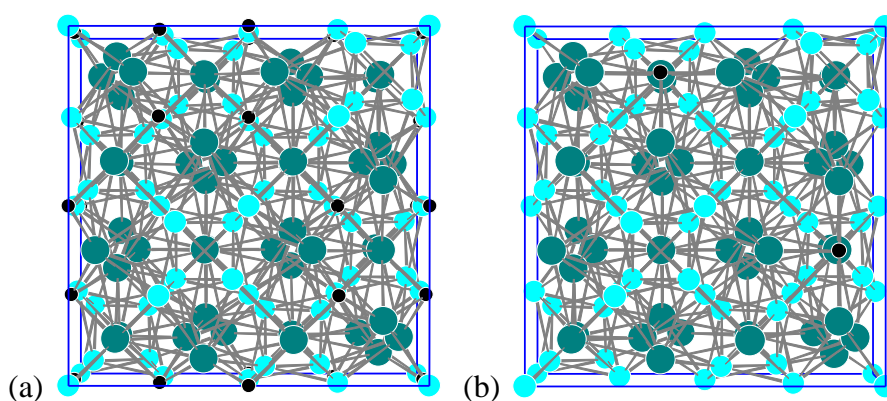


Figure 3–7. The crystal structures for the two cubic tungsten–nickel–carbide phases: (a) W_4Ni_2C ($cF112$) and (b) W_6Ni_6C ($cF104$). The larger light blue circles are Ni (including corners), the larger darker teal circles are W, and the smaller black circles are C. *Made in PowderCell* [22].

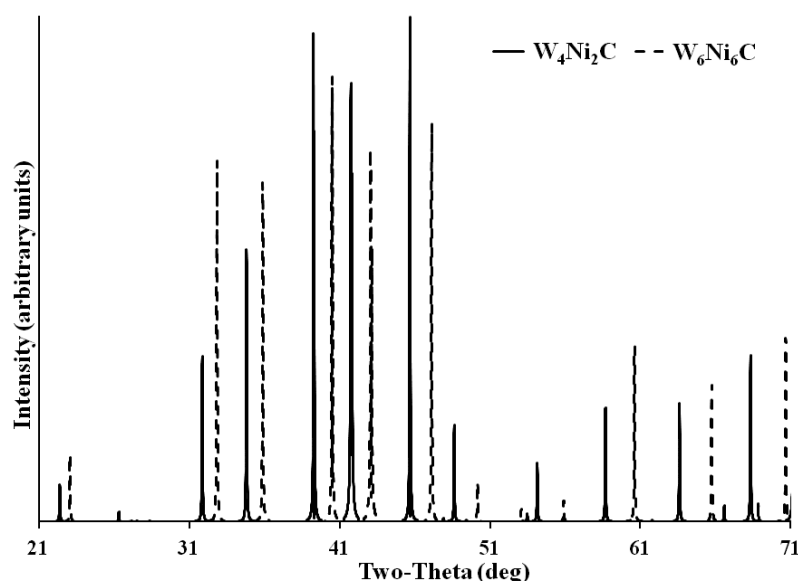


Figure 3–8. Calculated XRD plot demonstrating the similarity in structure of the two possible compositions for W_xNi_yC : W_4Ni_2C (*cF112*) and W_6Ni_6C (*cF104*). The peak locations (but not intensities) are horizontal displacements due to the difference in lattice parameters. *Made in PowderCell* [22].

In the XRD plot shown in Figure 3–9, typical of W51:Ni49 and W50:Ni50 samples annealed at 1000 °C and 1100 °C, the peaks all correspond to the W_xNi_yC phase. The diffraction patterns for samples annealed at 1150 °C and 1200 °C, as seen in Figure 3–10, indicate the clear presence of the hexagonal WC phase in addition to W_xNi_yC . Some of the spectra collected from samples annealed at 1000 °C and 1100 °C also show one or two peaks that can tentatively be assigned to the WC phase. While XRD was primarily carried out on blanket thin films on *p*-SiC, a few samples on *n*-SiC also support the formation of the W_xNi_yC phase at 1100 °C and 1150 °C, as well as WC at 1150 °C. The presence of carbides would suggest the presence of a phase containing silicon to

complete the mass balance [5], [113]. The XRD plots in Figures 3–6, 3–9, and 3–10 do not show any intense unidentified peaks, suggesting that a silicide phase may be amorphous or poorly crystallized. Although not detected by XRD, the presence of a silicide remains a possibility alongside the clearly observed phases listed in Table 3–4 for W51:Ni49 and W50:Ni50 samples. The microdiffractometer geometry can sometimes produce substrate peaks that dominate the plot, such as the SiC peaks shown in Figure 3–5 and 3–10.

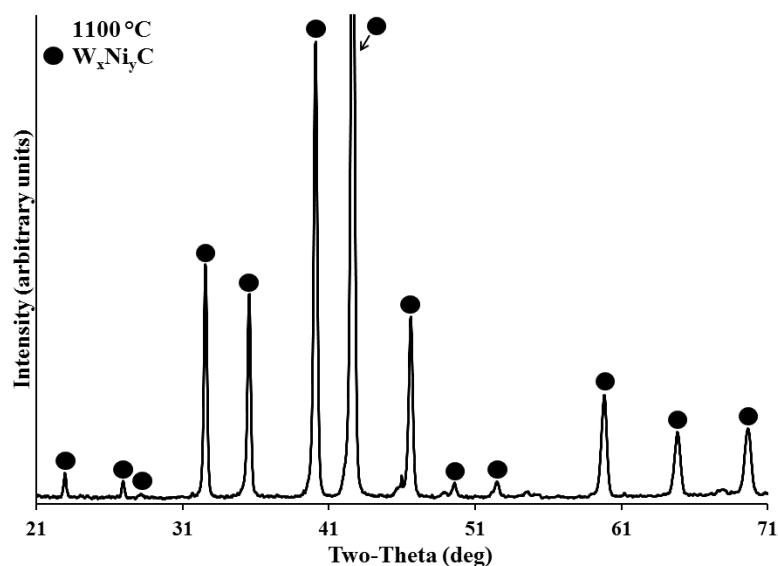


Figure 3–9. Microdiffractometer XRD plot for W50:Ni50/*p*-SiC annealed for 0.5 h at 1100 °C showing W_xNi_yC .

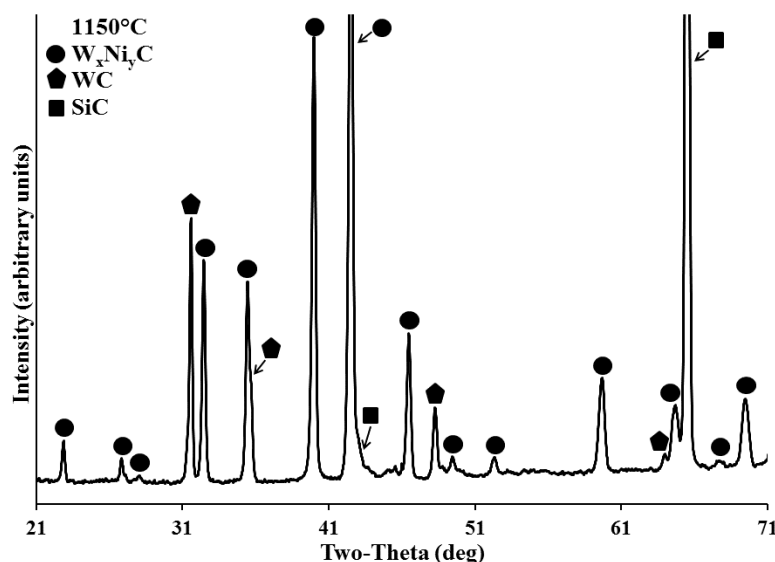


Figure 3–10. Microdiffractometer XRD plot for W51:Ni49/*p*-SiC annealed for 0.5 h at 1150 °C showing W_xNi_yC , WC, and SiC.

Previous literature on W:Ni alloys includes studies of both metallurgical sintering and electrodeposition of W–Ni coatings. The accepted W–Ni phase diagram shown in Figure 3–11 has three intermetallic phases: Ni_4W , Ni_2W , and NiW [129], [130]. Several studies sought to confirm all three phases but instead reported only the intermetallic compound Ni_4W , from quenching a variety of compositions [131], arc-melting [132], and electrodeposition [133]. Another arc-melting study of W and Ni pellets, annealed at 950 °C for 32 days, demonstrated again the formation of Ni_4W and $Ni(W)$ or $W(Ni)$; thus, the researchers proposed that carbon contamination in previous studies resulted in W_6Ni_6C being identified as NiW and W_4Ni_2C as NiW_2 [134]. Two recent studies found W_xNi_yC formation despite no intentional C contributions in both W–Ni sputtered on MgO as radiation resistant alloys [135] as well as electroplated and sputtered W–Ni on

oxidized Si annealed at 700 °C [136]. With SiC in this work as an obvious carbon source, the formation of W_xNi_yC here instead of a W–Ni binary phase makes sense.

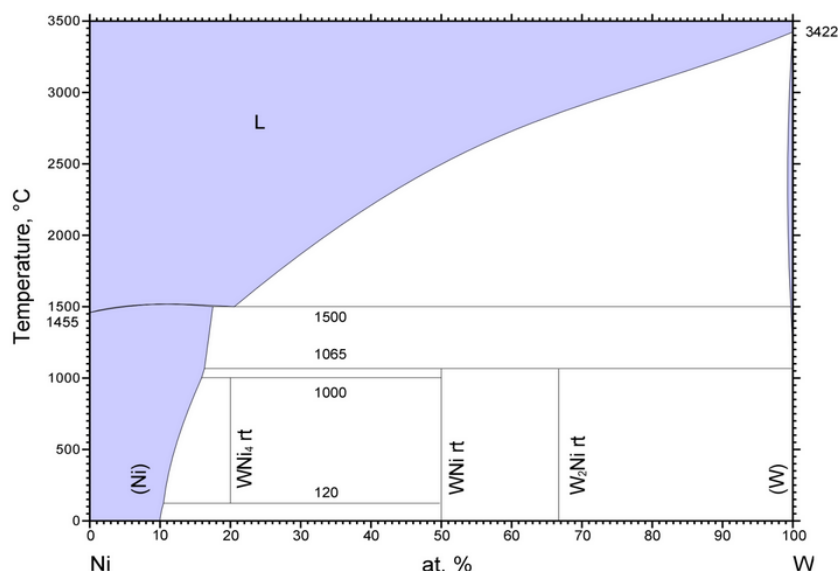


Figure 3–11. Binary W–Ni phase diagram with three intermetallic phases. Reprinted with permission from ASM International [130], all rights reserved, www.asminternational.org.

While researchers studying W–Ni alloys often viewed ternary carbides as undesirable, other studies have researched the W–Ni–C system for high-hardness coatings, focusing on mechanical and structural properties [128]. The phase equilibria and thermodynamics of W–Ni–C and WC–Ni systems have been studied since the 1930s, with the accepted W–Ni–C ternary phases [128] being two cubic η -carbides, W_4Ni_2C and W_6Ni_6C , as well as the hexagonal κ -carbide W_3NiC (not observed in this dissertation). In a 1956 powder sintering study [137], W_xNi_yC phases were studied as part of an isothermal phase diagram determination at 1200 °C. The W–Ni–C ternary phase

compositions were corrected by later researchers [128], as can be seen in the ternary phase diagram shown in Figure 3–12 [138]. Researchers studying the powder metallurgy of these alloys later noted the presence of cubic W_xNi_yC phases at 900 °C, 1100 °C, and 1300 °C [139]. In a 1975 arc-melting study [140], the isothermal W–Ni–C ternary phase diagram at 1300 °C was determined with careful notation of phases that agreed with Figure 3–12 at 1200 °C. Within the annealing conditions of 1000–1200 °C used in the present study, both cubic W_xNi_yC phases should be stable, based on the preceding discussion. The cubic (η) W_xNi_yC phase observed by XRD in this work has not been previously observed or discussed in thin film studies of W–Ni on SiC.

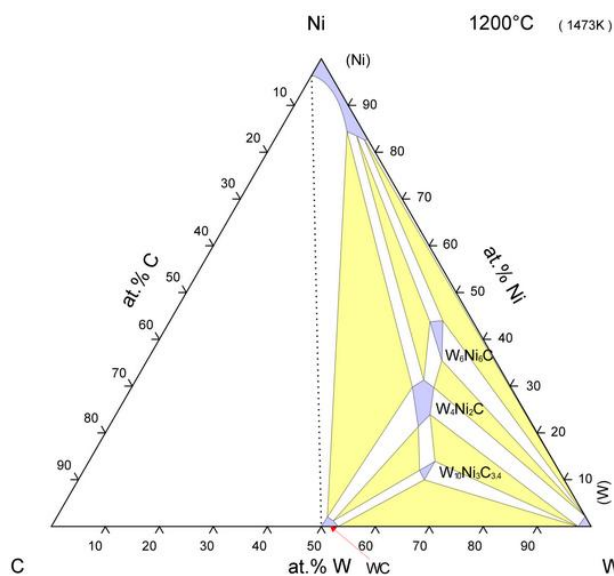


Figure 3–12. The W–Ni–C ternary phase diagram at 1200 °C (but typical also of 1300 °C [140]) showing three ternary carbides. Reprinted with permission from ASM International [138], all rights reserved, www.asminternational.org.

3.2.3.2 Scanning electron microscopy and X-ray energy dispersive spectroscopy

A distinctive surface morphology was noted in the FESEM for the W51:Ni49 and W50:Ni50 ohmic samples annealed at 1100 °C and above. The morphology for nominal W51:Ni49 on *p*-SiC tended to exhibit a densely packed formation of numerous ‘lath’ shapes along with larger ‘plates’ and featureless ‘field’ regions in between the plates and laths, as seen in Figure 3–13. As also seen in Figure 3–13, some plates have large triangular shapes, which can form into amalgamations of triangular plates (not shown). These triangular plates were more scarce in the nominal W50:Ni50/*p*-SiC samples, as seen in Figure 3–14. Several samples have much larger fields between more sparse laths and/or plates. On *n*-SiC, the morphology also consisted of laths on fields with at least some plates for both compositions.

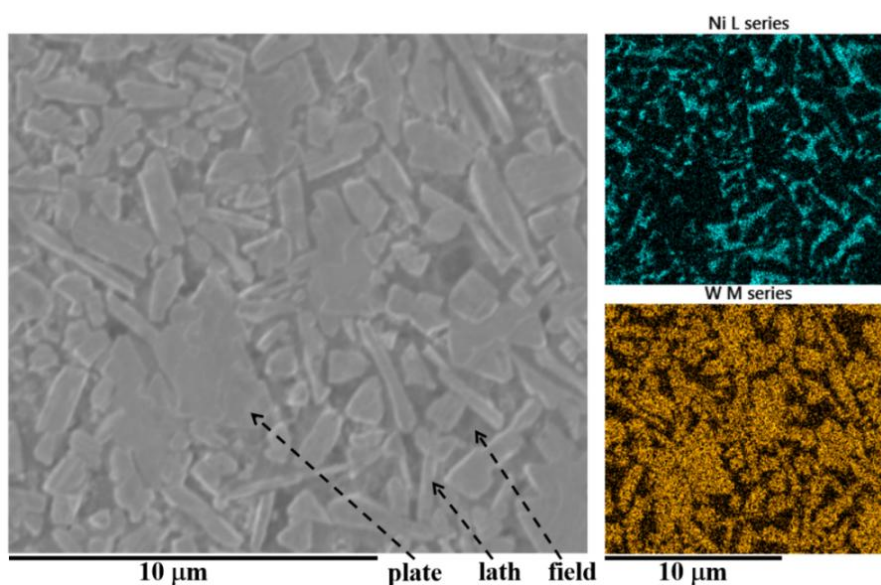


Figure 3–13. SEM image of lath- and plate-like surface morphology for W51:Ni49/*p*-SiC annealed at 1200 °C with XEDS maps showing complementary Ni- and W-rich regions.

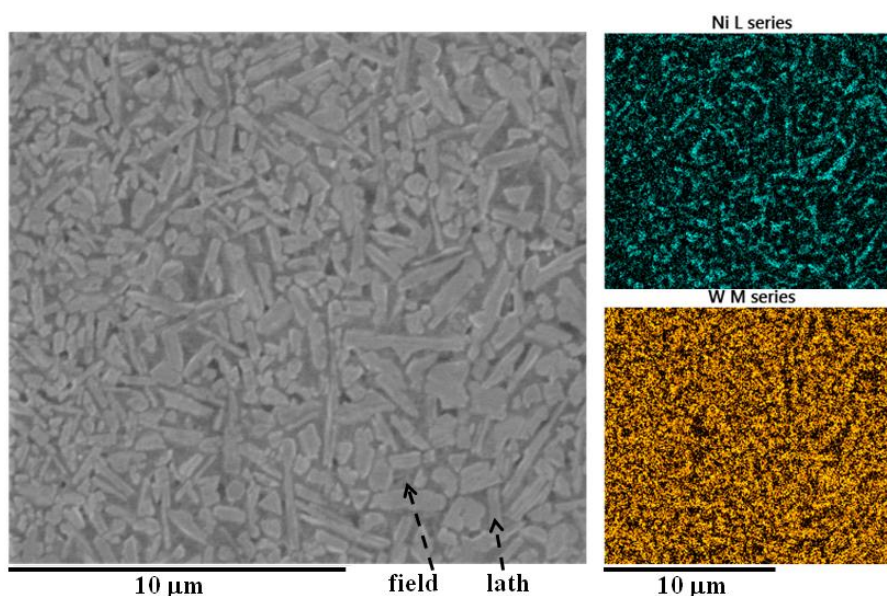


Figure 3–14. SEM image of solely lath-like surface morphology for W50:Ni50/*p*-SiC annealed at 1200 °C with XEDS maps showing complementary Ni- and W-rich regions.

Examination with XEDS revealed compositional differences between the regions. When analyzed with 5-keV electrons to minimize penetration depth, the fields showed more Ni. The distinctive morphology, especially the plates and laths, contained relatively more W. The Ni and W maps shown for Figure 3–13 and 3–14 illuminate that the W-rich morphology and the Ni-rich regions around them are spatially complementary. These maps have confirmed that metal (either Ni or W) was continuous across the contacts. The Si K and W M peaks overlap each other in XEDS, which makes distinguishing between the two difficult. Furthermore, the detection of Si could be from the SiC substrate through the thin metal film, from Si that is now within the thin film itself, or the Si cap on top of the thin film. With Si occurring everywhere in the samples, the Si maps (not shown) displayed signals across nearly the whole mapping area.

3.2.3.3 Tunneling atomic force microscopy

The distinct surface morphology raised questions about current conduction through the different phases in the samples, particularly across the metal–semiconductor interface. With W:Ni/SiC contacts annealed above 1000 °C containing multiple phases, one might imagine that the pathway for current transport into the SiC could be mainly through one phase or the other. This behavior could even vary with conductivity type. For example, one phase might present a lower Schottky barrier height to n -SiC, while the other might present a lower barrier height to p -SiC, thus promoting the simultaneous ohmic contact formation.

Atomic force microscopy (AFM) was briefly pursued at PSU to study the surface morphology with the help of Tim Tighe. A fine tip was rastered across a surface in tapping mode. The feedback from the cantilevered tip was then translated into a map of surface topography. Using Bruker's PeakForce tunneling AFM (TUNA), a current was also passed and measured from the tip to the sample—which necessitated grounding the ends of the mesas in the TLM structures with silver paint. With TUNA, more conductive regions may be identified simultaneously while mapping the surface topography, which can then be plotted with NanoScope Analysis software. In testing W51:Ni49/ p -SiC, more current was passed through the W-rich plate- and lath-like structures, as can be seen in Figure 3–15(b). These plate- and lath-like structures were also the taller features in the sample, as seen in the topography map Figure 3–15(a).

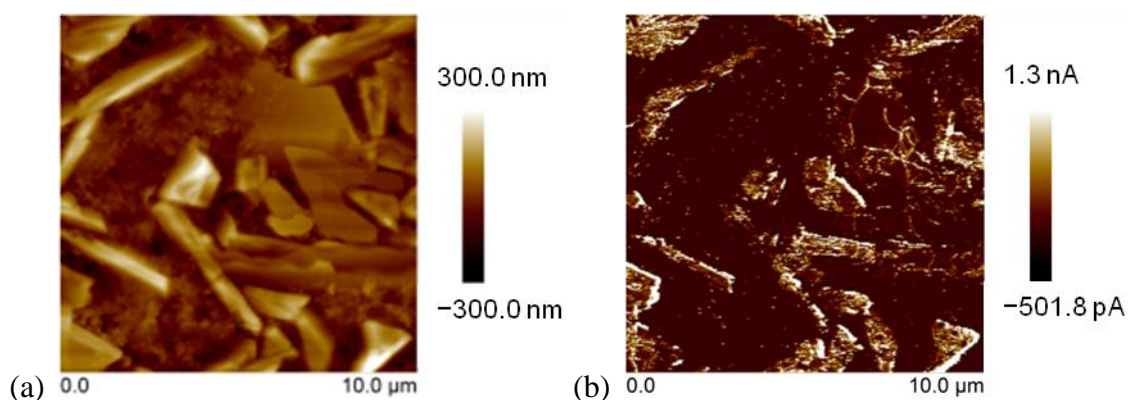


Figure 3–15. AFM of W51:Ni49/*p*-type SiC annealed at 1200 °C revealed (a) the surface topography map and (b) the map of peak current with the brighter regions being the conductive regions.

In a W51:Ni49/*n*-SiC sample, the Ni-rich field regions showed higher conductivity as seen in Figure 3–16(b). These results seem logical according to the history of Ni ohmic contacts to *n*-SiC recounted in Section 3.1.2, although no strong evidence of W ohmic contacts to *p*-SiC has been put forward. The topography map in Figure 3–16(a) for *n*-SiC, however, seems to indicate the field regions are taller than the plate- and lath-like structures. Without examining more samples, the taller regions may be more conductive as an artifact of TUNA. Thus, this apparent phase preference may be a premature conclusion.

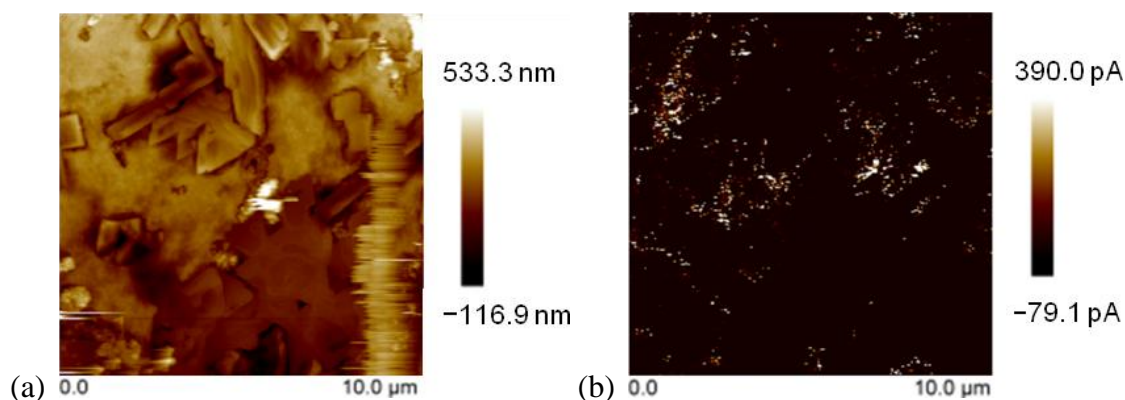


Figure 3–16. AFM of W51:Ni49/*n*-type SiC annealed at 1100 °C revealed (a) the surface topography map and (b) the map of peak current with the brighter regions being the conductive regions.

3.2.3.4 Auger electron spectroscopy

AES depth profiles were obtained from the as-deposited W and W:Ni films on SiC. These profiles indicated a minimal presence of oxygen in the metal-bearing layer and at the metal–SiC interface. Depth profiles from as-deposited W51:Ni49 and W50:Ni50 are seen in Figures 3–17 and 3–18, respectively. The atomic concentration values for W and Ni shown in Figures 3–17 and 3–18 are not identical to the W:Ni alloy ratios of Table 3–2 since they are normalized to include the AES signal noise from C, O, and Si. However, the ratios between the W and Ni concentrations do align with the compositions shown in Table 3–2 and discussed in Section 3.2.1, with W51:Ni49 films being more W-rich by ~5 at.% as compared to W50:Ni50 films.

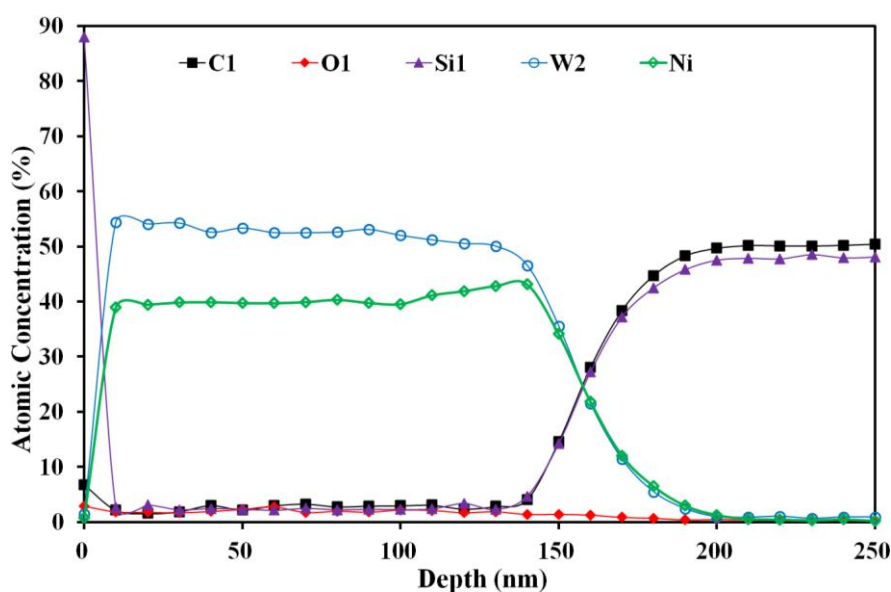


Figure 3–17. AES depth profile for as-deposited W51:Ni49/*n*-SiC. The W:Ni ratios are in agreement with the discussed film composition of W57:Ni43 but the atomic concentrations differ due to the included signal noise from C, O, and Si.

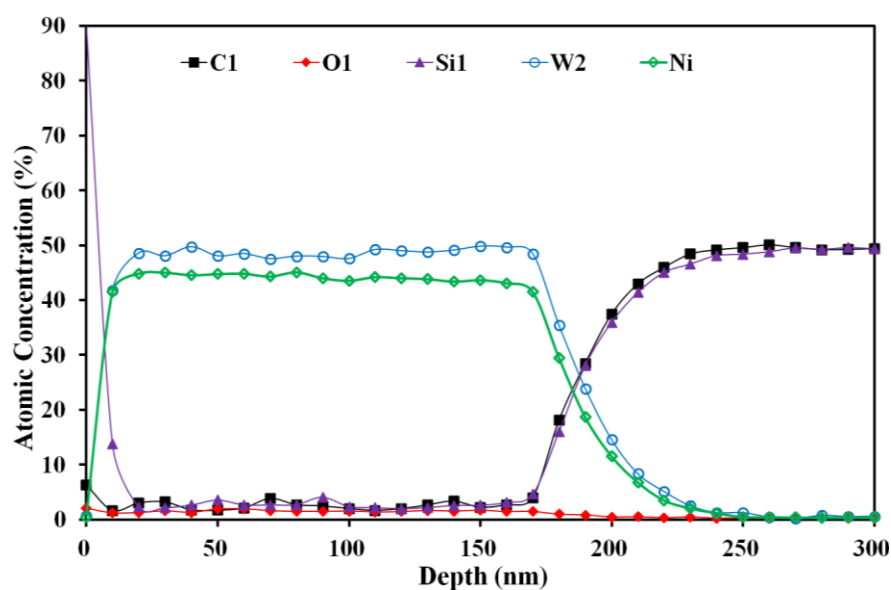


Figure 3–18. AES depth profile for as-deposited W50:Ni50/*n*-SiC. The W:Ni ratios are in agreement with the discussed film composition of W52:Ni48 but the atomic concentrations differ due to the included signal noise from C, O, and Si.

AES depth profiles through the distinct features in the surface morphology linked the Ni- and W-rich regions seen in XEDS to the phases identified using XRD. As seen in the depth profile of Figure 3–19 through a plate-like feature, the metal film underneath a thin oxidized Si cap has reacted to form a tungsten carbide. In comparison, the depth profile seen in Figure 3–20 through a field region revealed C near the surface alongside the oxidized Si cap, followed by a metal carbide region containing W, Ni, C, and Si. Beneath both regions, a Ni-rich region contained Si and C but limited W. The Auger peak shapes for C (e.g., Figure 2–22) in both Figures 3–19 and 3–20 were characteristic of a metal carbide in the upper layers for both features, but showed non-carbide C in the Ni-rich region closer to the SiC interface.

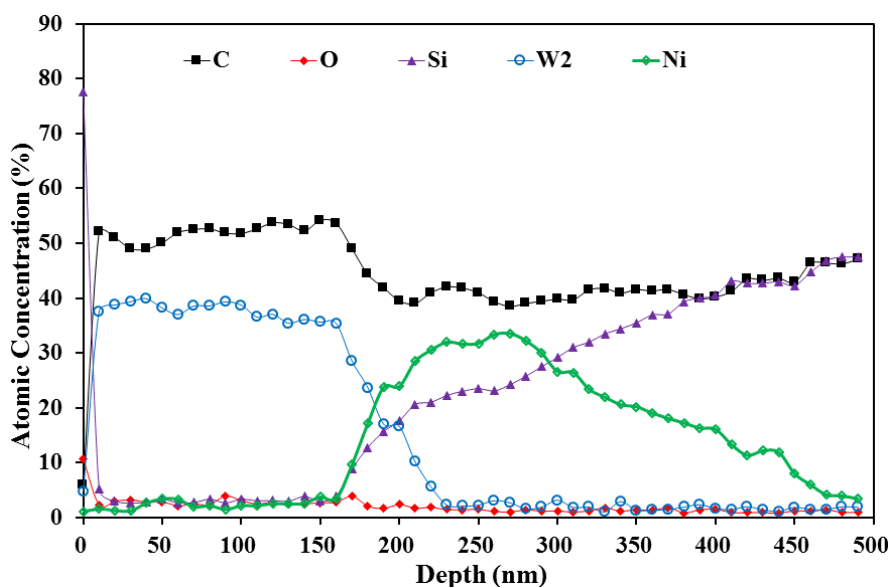


Figure 3–19. AES depth profile for W51:Ni49/*p*-SiC annealed at 1150 °C through a plate-like region, showing a tungsten carbide region over a Ni+Si region.

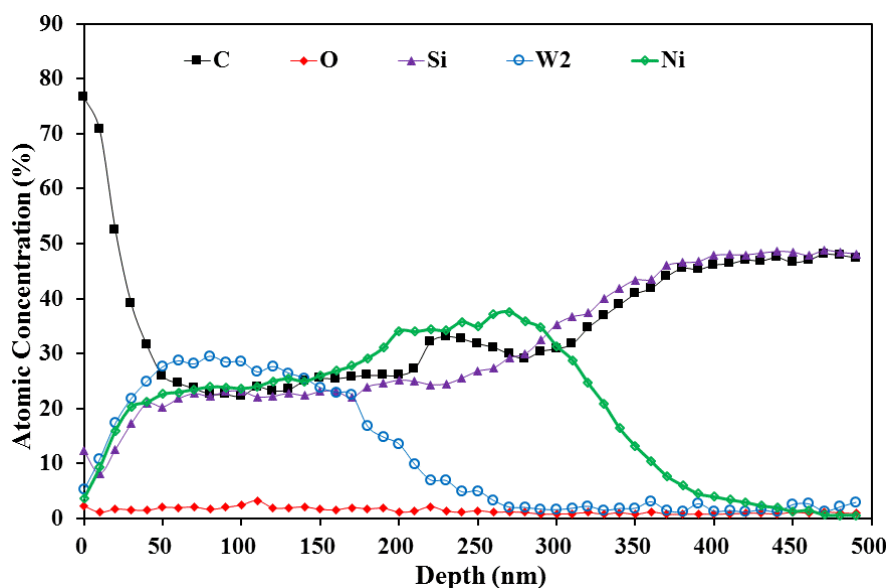


Figure 3–20. AES depth profile for W51:Ni49/*p*-SiC annealed at 1150 °C through a field-like region showing a metal carbide region above a Ni+Si region.

Sensitivity factors for C (KLL) Auger peaks were calculated from peak-to-peak values, which can vary with bonding chemistry. In this case, the factors were not adjusted to correct for the presence of a metal carbide, which gave rise to some error in the W to C ratio in the tungsten carbide region. However, considering the XRD data and the semi-quantitative nature of AES, the clearest conclusion is that the plate-like morphology corresponds to WC. The field regions of the surface morphology correspond to W_xNi_yC with dissolved Si. This morphology and phase identity fit with a similar SEM image of WC plate-like shapes separating out from W_4Ni_2C after melting a wear-resistant, complex Ni-based alloy at 1200 °C [141]. The Ni+Si+C region could be an amorphous or poorly crystallized nickel silicide, either of which would explain the lack of identifiable peaks by XRD. The C could be either dissolved in the silicide or graphite

alongside the silicide. Previous studies into the Ni–Si–C system [142], [143] have shown the coexistence of graphite along with several Ni-rich silicides even at 1170 °C.

The W51:Ni49 and W50:Ni50 thin films annealed at 1000 °C exhibited a featureless appearance (e.g., a field-like region), as seen in Figure 3–21, rather than the segregated surface morphology seen in Figures 3–13 and 3–14. A further AES depth profile in Figure 3–22 showed primarily $W_xNi_yC(Si)$ below the Si cap and above the SiC epilayer, supporting the phase identification given in Table 3–4. As seen in Figures 3–20 and 3–22, W_xNi_yC can apparently dissolve a significant amount of Si, which may be present in the structure in substitutional or interstitial sites. Notably, AES depth profiles for $W_xNi_yC(Si)$ such as Figure 3–22 matched the plots in the prior paper on W:Ni/6H-SiC, which had postulated a mixture of carbides and silicides at the same level [113]. Without structural data from the 6H-SiC study, the AES in the present study would suggest identification in that study as $W_xNi_yC(Si)$ instead. The prior W:Ni aging study [5], however, reported the presence of WC and Ni_xSi_y , although with different film thicknesses and higher ρ_c values than those found in this work.

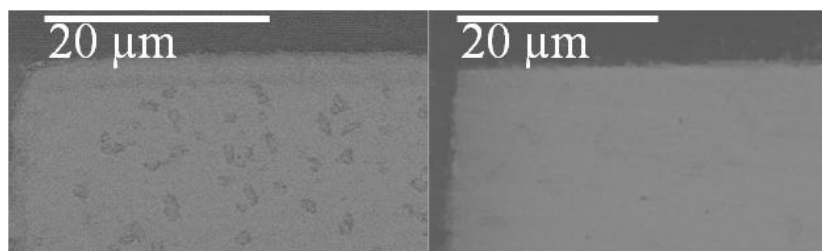


Figure 3–21. SEM images of W51:Ni49/SiC showing the surfaces with fewer features after annealing at 1000 °C.

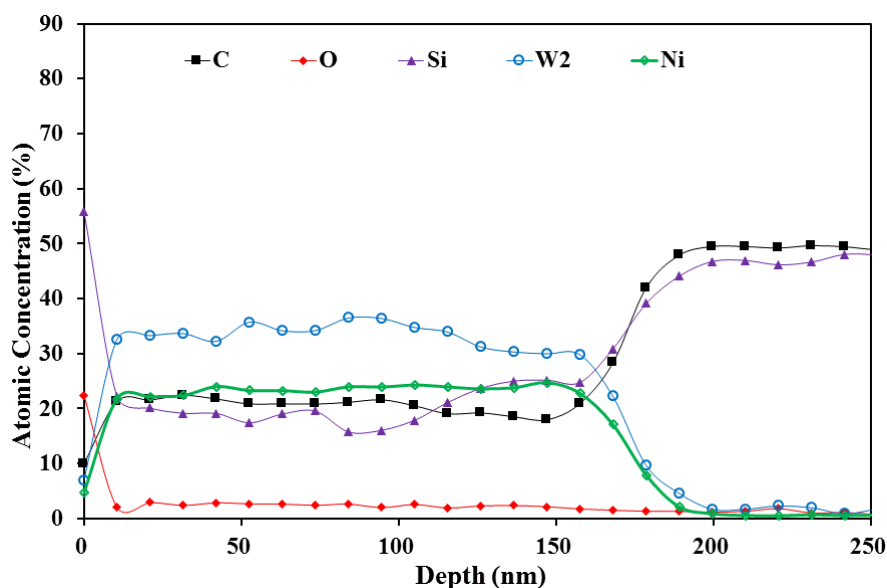


Figure 3–22. AES depth profile for W51:Ni49/*p*-SiC annealed at 1000 °C showing a metal carbide region above the SiC epilayer.

Depending on the location of the Si, the lattice parameter of the W_xNi_yC could expand or contract, which would support the observation by XRD that the lattice parameter did not perfectly match either of the two known cubic ternary phases. On a qualitative level, the AES profiles would support the presence of comparable amounts of W and Ni, favoring identification of W_xNi_yC as W_6Ni_6C . On the other hand, the W–Ni–C ternary phase diagram [138] seen in Figure 3–12 shows no tie-line between WC and W_6Ni_6C —only between WC and W_4Ni_2C [128]. The tie-line between WC and W_4Ni_2C along with the aforementioned similar morphology image [141] support the W_xNi_yC identification as W_4Ni_2C with a reduced lattice parameter from the Si.

These AES depth profiles presented in Figures 3–19, 3–20, and 3–22 were all performed for W51:Ni49/*p*-SiC. The temperature evolution would suggest the formation

of $W_xNi_yC(Si)$ first, shown here as low as 1000 °C. The WC and Ni_xSi_y formed at higher annealing temperatures. The WC and $W_xNi_yC(Si)$ then are pushed outwards toward the surface of the sample, as Ni_xSi_y with C was formed nearer to the metal–SiC interface. A summary of the geometric arrangement of these phases with annealing can be seen in Figure 3–23. In a few AES depth profiles performed on W50:Ni50/*p*-SiC, the sample annealed at 1000 °C showed a modest uptick in Ni+Si presence closer to the metal–SiC interface as seen in Figure 3–24. Even with earlier formation of Ni_xSi_y , the general phase evolutions would appear still valid.

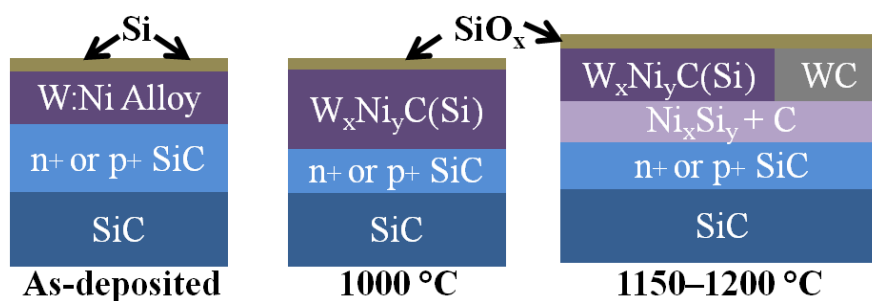


Figure 3–23. Representation of the spatial arrangement of Si/W51:Ni49/SiC before and after annealing. The phases are shown in their relative locations but not to scale.

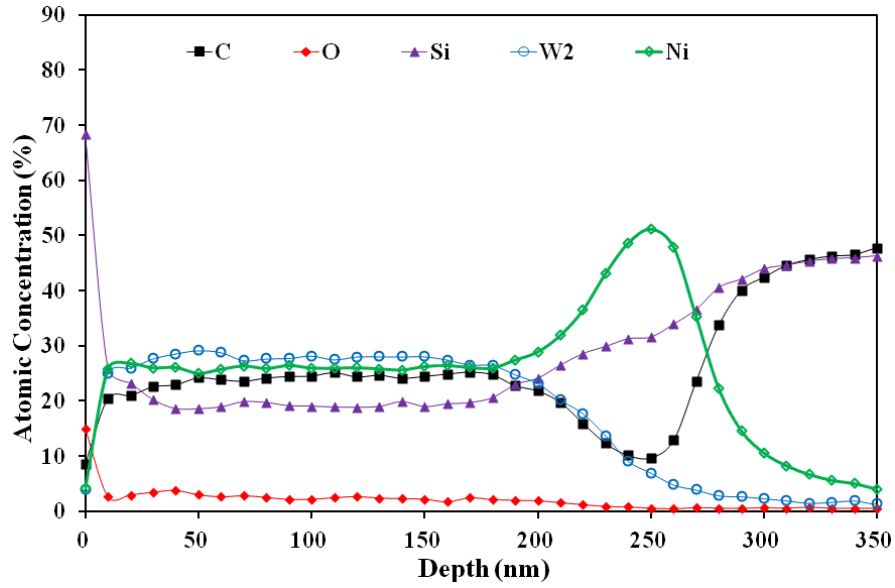


Figure 3–24. AES depth profile for W50:Ni50/*p*-SiC annealed at 1000 °C showing a metal carbide region with an increase in Ni adjacent to the SiC substrate.

The reactions between W:Ni and SiC into W_xNi_yC and WC as well as a silicide would involve the partial consumption of the SiC epilayers. The epilayer thickness under the contacts ($t_{\text{epi, contact}}$) would now be smaller than the epilayer in the gaps between the contacts ($t_{\text{epi, gap}}$). This change in epilayer would cause the sheet resistance under the contacts ($R_{\text{sh, contact}}$) to be higher than the sheet resistance between the contacts ($R_{\text{sh, gap}}$). Determining the penetration depth can allow a calculation of the new sheet resistance [35], as seen in Eq. 3–1. The new sheet resistance will affect the transfer length (L_T), and ultimately the specific contact resistance. Field-emission scanning electron microscopy was used to investigate the penetration depth of the W:Ni alloys into the *p*-SiC after milling out a wedge using a focused ion beam (FIB). In Figure 3–25, the polished wall (marked with an arrow) inside the removed wedge (the dashed box) can be seen on the

cartoon along with the SEM image showing the profile of an ohmic contact on a mesa.

The approximate penetration depth ($z \approx 88\text{--}108\text{ nm}$) of the W:Ni layer below the plane of the mesa has been measured in the SEM in order to obtain the actual sheet resistance underneath the contacts. The epilayer thicknesses ($t_{\text{epi, gap}}$) were $0.5\text{ }\mu\text{m}$ for $p\text{-SiC}$ and $2\text{ }\mu\text{m}$ for $n\text{-SiC}$. Thus, the specific contact resistance values may actually be about 20% lower than reported in this dissertation for contacts to $p\text{-SiC}$ and up to 10% lower for contacts to $n\text{-SiC}$, presuming the same depth of reaction.

$$R_{\text{sh,contact}} = R_{\text{sh,gap}} \frac{t_{\text{epi,gap}}}{t_{\text{epi,contact}}} = R_{\text{sh,gap}} \frac{t_{\text{epi,gap}}}{t_{\text{epi,gap}} - z} \quad (3-1)$$

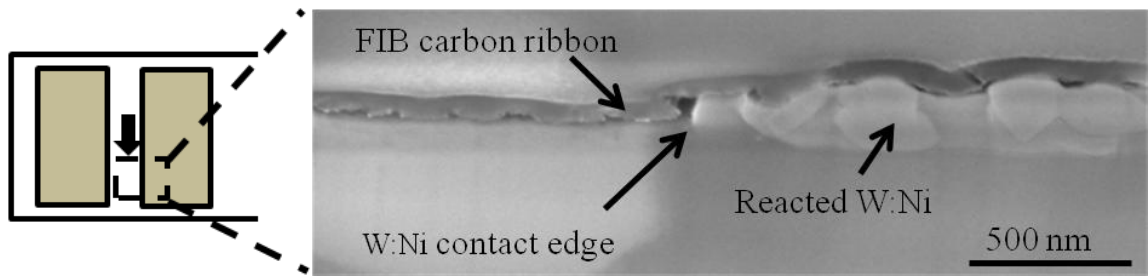


Figure 3–25. SEM image of a polished cross-section for W50:Ni50 reacted with $p\text{-SiC}$ after annealing at $1100\text{ }^{\circ}\text{C}$, showing the reaction depth into the mesa.

3.3 Literature on Aging and Diffusion Barriers for SiC

The previous section of this work focused on the formation of ohmic contacts, as has large sections of the SiC literature. After successful ohmic contact formation, however, the thermal stability of these contacts is another important area of research. Common approaches to diffusion barriers from Si technology have included using single crystal or amorphous films to prevent travel through grain boundaries; finding films to

limit mixing or thermodynamic reactions both with other layers and ambient oxygen; and stuffing the grain boundaries to prevent diffusion [144]. While some contacts alone are tested for thermal stability, others are tested with additional conductive layers to limit oxygen from reacting with the contact metal(s) and/or to prevent the contact metals from reacting with wire bonding materials [145], [146]. Single crystal layers would be difficult to deposit, and amorphous films would likely crystallize at the high annealing temperatures. Thus, the layers in SiC diffusion barriers have often been selected to limit chemical reactions and interdiffusion. Ultimately, using diffusion barriers can extend the lifetime of electrical operation without loss of electrical signal transmission.

Many of the same materials popular for ohmic contacts (e.g., Ni, Al, W) will also readily oxidize at higher temperatures. Thus, some studies aimed to test the ohmic contact stability in non-oxidizing environment (e.g., Ar or N₂) before developing the correct layers to limit material and chemical interactions for survival in air. A very recent review publication by Z. Wang *et al.* [145] has reviewed a large number of thermal aging reports conducted on ohmic contact materials and/or diffusion barriers for SiC. The following literature review will share a selection of both promising aging studies as well as those with relevant materials. Some ohmic contact studies on both formation and thermal stability may be reiterated as relevant from the prior section for clarity.

Various studies for Au- and Al-capped diffusion barriers have been performed in the multi-thousand hour range for lower aging temperatures ≤ 400 °C in air [145]. The lengthiest study has been for Ni₂Si contacts to *n*-4H-SiC, with Al-Si/Ta/TaN diffusion barriers stabilizing the ρ_c through 12,000 h at 385 °C [147]. At 400 °C and above, the research has mostly focused on shorter times for development (≤ 100 h) and stability

(≤ 1000 h). Ni_2Si simultaneous ohmic contacts were stable through 95 h in N_2 at 400°C [116]. $\text{W}/\text{Ni}/p\text{-SiC}$ [122] and $\text{W}/\text{Ti}/\text{Ni}/n\text{-SiC}$ [126] were both found favorable through 1000 h+ and 100 h+, respectively, at 400°C in Ar. Likewise, $\text{TiW}/\text{Ni}/\text{C-face } n\text{-SiC}$ was favorable through 100 h at 400°C in N_2 [148]. WSi_2 contacts to $n\text{-6H-SiC}$ saw $\rho_c \approx 10^{-4} \Omega\text{cm}^2$ after 150 h in air at 400°C , but only with Al-encapsulation [57]. The recent $\text{Al}/\text{Ti}/\text{Ni}/p\text{-SiC}$ contacts [102] were annealed with minimal change in ρ_c for 100 h at 300°C in N_2 and only a small ($\leq 2\times$) increase after 100 h at 600°C . The higher annealing temperature was associated with increased surface roughness and pitting [102].

A few studies have conducted thermal testing in high vacuum $\approx 10^{-8}\text{--}10^{-6}$ Torr. $\text{W}/\text{WC}/\text{TaC}$ on $n\text{-SiC}$ demonstrated $\rho_c \approx 10^{-5} \Omega\text{cm}^2$ through 1000 h at 600°C , as well as through 700 h at 1000°C [149]. An additional 300 h at 1000°C witnessed a dramatic ρ_c increase due to oxidation of the TaC from residual O, even under high vacuum [149]. Additional demonstrations of excellent thermal stability in vacuum include $\text{W}/\text{Cr}/\text{Ni}$ contacts to $n\text{-SiC}$ held at 650°C for 3000 h+ [127] and $\text{W}/\text{Ni}/\text{Al}$ on $p\text{-SiC}$ held at 600°C for 1000 h+ [123]. Annealing the same $\text{W}/\text{Ni}/\text{Al}$ contacts in air resulted in oxidation for 1 h alone at 600°C ; however, the addition of Au on top enabled 100 h+ of fairly steady ρ_c values—although with a much higher ρ_c than the vacuum anneal [123].

Many previous studies have focused on Pt/TaSi_2 as well as $\text{Pt}/\text{Ti}(\text{N})$, which have risen to the challenge of contacts surviving at 500°C and 600°C in air [145]. Pt/TaSi_2 on Ti contacts to $n\text{-6H-SiC}$ was annealed at 500°C and 600°C in air following ohmic contact formation in forming gas [150]. After 600 h at 500°C and 150 h at 600°C , ρ_c values $\approx 10^{-4} \Omega\text{cm}^2$ corresponded to platinum silicide formation but little oxidation [150]. Increasing the layer thicknesses to 200 nm Pt/400 nm TaSi_2 mostly prevented oxidation

of Ti/*n*-6H- and *n*-4H-SiC for 1000 h at 600 °C in air [15]. These contacts ultimately saw oxygen diffusing only laterally from the edges at 1000 h with $\rho_c \approx 10^{-5} \Omega\text{cm}^2$ [15]. This diffusion barrier scheme was also utilized in an *n*-6H-SiC junction field effect transistor (JFET) for thousands of hours in air at 500 °C [6]. With the same increased Pt/TaSi₂ thicknesses, these diffusion barriers for Ni contacts survived 300 h+ in air at 600 °C; however, oxygen was shown in AES to be creeping in by 36 h [17]. This combination of layers involved Pt restricting oxidation and TaSi₂ limiting Pt mixing with the contact metal. An important limitation, however, was that PtSi_x disrupts the Au wire bonding process. Consequently, Pt/Ir/Pt/TaSi₂/Ti/*n*-SiC was shown to allow strong Au wire bonding even after 1000 h in air at 500 °C [146]. Protective amorphous silicon oxide and silicon carbide coatings alongside Ti/TiN/Pt/Ti interconnects were used for Ti and Ni contacts to *n*-4H-SiC [16]. These contacts were aged in both dry and wet synthetic air for 500 h at 600 °C, with $\rho_c \approx 10^{-4} \Omega\text{cm}^2$ for the Ti contacts. Additional thermal cycling was performed between 100–700 °C, with the Ti contacts remaining ohmic through 100 cycles [16].

The inclusion of W in Pt-containing diffusion barriers has also shown some promise. TiW contacts on *n*-SiC protected by a Ti/Pt diffusion barrier lasted 520 h at 600 °C in air with continuous ohmic behavior [18]. The Pt/TiW bilayers are important as a composite, as Au/TiW/Ni₂Si/*n*-SiC degraded after only 4 h in oxygen at 600 °C [151] while exhibiting a stable structure through hundreds of hours in vacuum. Pt/Ti/WSi has also acted as a diffusion barrier for Ni contacts at 650 °C in N₂ for 100 h [74]. Previous research has also investigated stuffing TiW [152] with nitrogen to prevent diffusion pathways.

Overall, most of the studies presented here focused on diffusion barriers for ohmic contacts on *n*-SiC, and more compelling examinations of thermally stable contacts to *p*-SiC are also needed. One of the few studies conducted was for Au/Ti:Al, Au/AlSiTi, and Au/Al/Si, all on *p*-4H-SiC [153]. These contacts were aged in N₂ for 100 h at 500 °C, 600 °C, and 700 °C with only moderate increases in ρ_c , except for a larger ρ_c increase for Au/Al/Si at 700 °C [153]. While most aging studies for SiC are focused upon the upper bound of temperatures at 500 °C and 600 °C [145], very few researchers have investigated higher temperatures beyond 700 °C. A Ni/Ti/*n*-6H-SiC study aged the contacts for 10 h at 900 °C in H₂ with good stability [121]. The highest temperatures in any aging studies are for the W/WC/TaC study at 1000 °C in vacuum [149] and the Si/W:Ni at 1000 °C in Ar [5], both on *n*-SiC.

For SiC technology to continue advancing, diffusion barriers and ohmic contact thermal stability for SiC at 600 °C and higher temperatures will need further investigation to become mature solutions.

3.4 Aging and Diffusion Barriers for W:Ni/4H-SiC

In this section, the simultaneous W:Ni ohmic contacts were subjected to additional annealing for insight into their thermal stability via electrical characterization. Preliminary investigation was also made into using Pt+C/TaSi₂ layers as diffusion barriers—focusing on compositional characterization by AES.

3.4.1 Aging of W:Ni contacts

3.4.1.1 Aging for hypersonic flight (1000 °C+)

In the prior W:Ni aging study on *n*-4H-SiC [5], the W:Ni contacts were annealed at 1000 °C to simulate hypersonic flight for 15 h in Ar with stable ρ_c values. This study intended to explore the stability for the simultaneous ohmic contacts achieved in the previous section out to 16 h. Measurements would be taken for total annealing times as multiples of two (e.g., 0.5, 1, 2, 4, 8, 16 h). The simultaneous ohmic contacts were solvent cleaned and blown dry with N₂ gas before being loaded into the dedicated tube furnace described in Section 2.1.4. These samples were annealed for 0.5 h (1 h total) in Ar at their respective annealing temperatures: 1000–1150 °C. Current–voltage measurements were then collected with the same expectations of linearity; however, the number of TLM structures (*N*) had been reduced for various samples due to (destructive) materials characterization.

During formation, the lower ρ_c values were obtained from samples annealed for 0.5 h at 1100 and 1150 °C. These samples after annealing for 1 h total at their respective temperatures saw mostly dramatic increases in ρ_c , as detailed in Table 3–5. The ρ_c values increased an order of magnitude or more for all measurable contacts to *p*-SiC and most contacts to *n*-SiC. The contacts to *n*-SiC annealed at 1100 °C saw only a four-fold increase for W51:Ni49 and slight decline (with an increase in spread) for W50:Ni50. The optical microscope used during current–voltage measurements indicated a considerable darkening of many contact surfaces to near black.

Table 3–5. Average specific contact resistance ρ_c \pm standard error (σ/\sqrt{N}) in Ωcm^2 after aging in Ar. Shaded conditions had minimal changes between 1 st and 2 nd anneals.					
Temperature	Composition	ρ_c after 1 st anneal	N	ρ_c after 2 nd anneal	N
1000 °C	W51:Ni49	$(1.5 \pm 0.1) \times 10^{-5}$ p	13	$(2.5 \pm 0.3) \times 10^{-5}$ p	8
		$(1.4 \pm 0.1) \times 10^{-5}$ n	15	$(1.2 \pm 0.1) \times 10^{-5}$ n	15
1100 °C	W51:Ni49	$(1.1 \pm 0.3) \times 10^{-5}$ p	11	$(4.9 \pm 0.9) \times 10^{-4}$ p	11
		$(1.0 \pm 0.1) \times 10^{-5}$ n	15	$(3.4 \pm 0.6) \times 10^{-5}$ n	14
1150 °C	W51:Ni49	$(7.3 \pm 0.9) \times 10^{-6}$ p	13	N/A p	0
		$(9.2 \pm 1.3) \times 10^{-6}$ n	14	$(1.0 \pm 0.3) \times 10^{-4}$ n	7
1000 °C	W50:Ni50	$(9.5 \pm 1.6) \times 10^{-6}$ p	13	$(1.0 \pm 0.2) \times 10^{-5}$ p	13
		$(2.9 \pm 0.2) \times 10^{-5}$ n	14	$(1.7 \pm 0.2) \times 10^{-5}$ n	14
1100 °C	W50:Ni50	$(1.5 \pm 0.2) \times 10^{-5}$ p	13	$(2.8 \pm 0.5) \times 10^{-4}$ p	9
		$(1.7 \pm 0.1) \times 10^{-5}$ n	15	$(1.3 \pm 0.2) \times 10^{-5}$ n	14
1150 °C	W50:Ni50	$(2.4 \pm 0.4) \times 10^{-5}$ p	8	$(8.7 \pm 1.2) \times 10^{-4}$ p	8
		$(6.8 \pm 0.9) \times 10^{-6}$ n	13	$(6.4 \pm 1.5) \times 10^{-5}$ n	11

The TLM structures annealed for 1 h total at 1000 °C demonstrated more minor variations in values, which are shaded in Table 3–5. The ohmic contacts to *p*-SiC saw a slight increase in ρ_c values, $\sim 2 \times$ for W51:Ni49 and $\sim 5\%$ for W50:Ni50. Meanwhile, the contacts to *n*-SiC saw slight decreases in values. All of these changes can be seen in Table 3–5 and Figure 3–26. Despite these promising results, further cumulative annealing of these samples was discontinued in order to use the matched TLM samples annealed at 1000 °C for further aging tests at 600 °C.

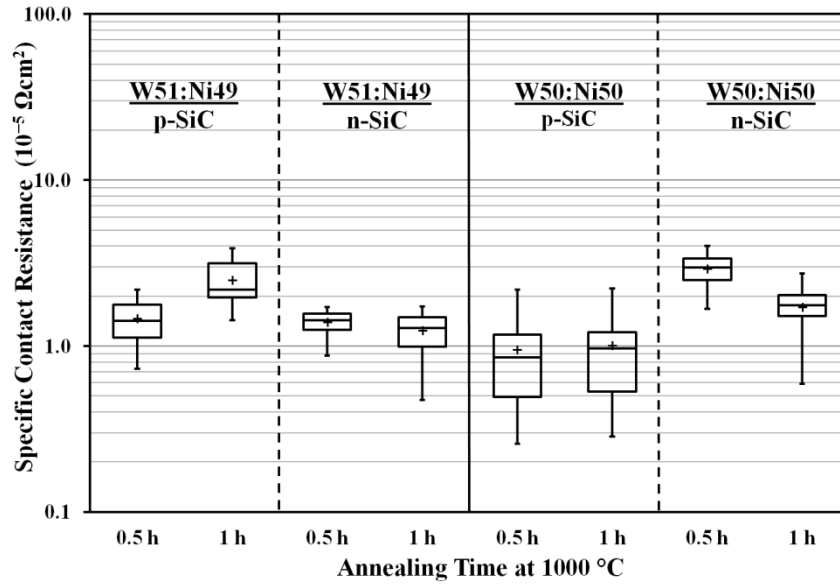


Figure 3–26. Specific contact resistances for W:Ni contacts on *p*-SiC with $N_A = 3 \times 10^{20} \text{ cm}^{-3}$ and *n*-SiC with $N_D = 2 \times 10^{19} \text{ cm}^{-3}$ after 1 h total annealing at 1000 °C. The boxplot shown has the averages marked with plus signs.

While additional TLM structures with contacts to *p*-SiC doped at $3 \times 10^{20} \text{ cm}^{-3}$ were unavailable, ohmic contacts to *p*-SiC were available at a lighter doping level. TLM structures on semi-insulating Si-face (0001) SiC with 2 μm of *p*-type epilayer doped at $1 \times 10^{20} \text{ cm}^{-3}$ had been fabricated at the same time as the *n*-type structures. These samples also proved to be ohmic after annealing at 1000–1150 °C, albeit with higher ρ_c values of $\approx 10^{-4}$ – 10^{-3} Ωcm^2 from the lower doping, as detailed in Table 3–6. The ρ_c values for these samples followed similar trends to the higher doping discussed in Section 3.2.2, with lower values after annealing at 1100 °C and 1150 °C as can be seen in Figure 3–27. The boxplot shows much tighter distributions in values for these contacts to more lightly-doped *p*-SiC, which is reflected in smaller standard errors in the subsequent tables.

Table 3–6. Average specific contact resistance ρ_c \pm standard error (σ/\sqrt{N}) in Ωcm^2 for $N_A = 1 \times 10^{20} \text{ cm}^{-3}$. Total annealing time was 0.5 h in Ar.				
	W51:Ni49	N	W50:Ni50	N
1000 °C	$(1.59 \pm 0.02) \times 10^{-3}$	15	$(6.1 \pm 0.2) \times 10^{-4}$	14
1100 °C	$(4.1 \pm 0.2) \times 10^{-4}$	15	$(2.8 \pm 0.1) \times 10^{-4}$	15
1150 °C	$(5.2 \pm 0.2) \times 10^{-4}$	14	$(2.6 \pm 0.1) \times 10^{-4}$	13

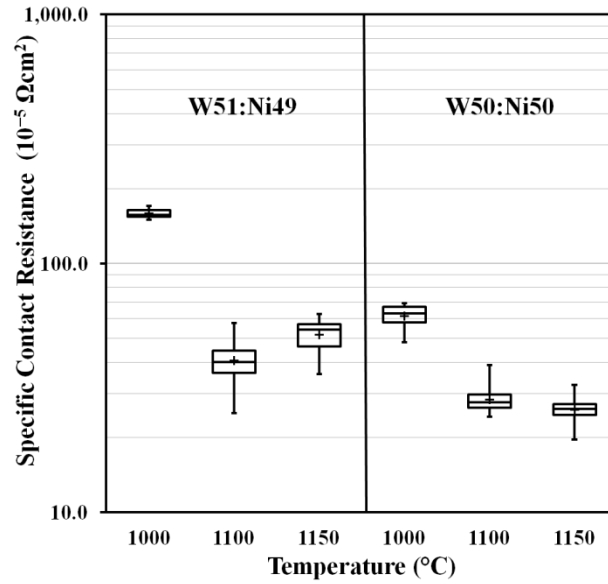


Figure 3–27. Specific contact resistances for W:Ni contacts on p -SiC with $N_A = 1 \times 10^{20} \text{ cm}^{-3}$ after 0.5 h total annealing at 1000–1150 °C, with similar trends but a different scale from the matched pairs. The boxplot shown has the averages marked with plus signs.

Further aging of these samples in the same furnace runs as those already discussed for an additional 0.5 h at their annealing temperatures 1000–1150 °C showed increases in the average ρ_c values except for W51:Ni49/ p -SiC at 1000 °C, which showed minor decreases. The behavior at higher temperatures was not as dramatic as the more

heavily-doped samples, with increases of $1.5\text{--}2.4 \times$ the values from the 1st anneal. These increases in the average ρ_c , however, were accompanied by considerable increases in spread. The summary of these values is shown in Table 3–7, and the more stable samples from 1000 °C were also saved for aging at 600 °C.

Table 3–7. Average specific contact resistance ρ_c \pm standard error (σ/\sqrt{N}) in Ωcm^2 for $N_A = 1 \times 10^{20} \text{ cm}^{-3}$. Total annealing time was 1 h in Ar.				
	W51:Ni49	N	W50:Ni50	N
1000 °C	$(1.46 \pm 0.02) \times 10^{-3}$	15	$(7.8 \pm 0.3) \times 10^{-4}$	14
1100 °C	$(7.0 \pm 0.4) \times 10^{-4}$	15	$(5.0 \pm 0.4) \times 10^{-4}$	11
1150 °C	$(7.9 \pm 1.8) \times 10^{-4}$	9	$(6.1 \pm 1.2) \times 10^{-4}$	7

Additional TLM pieces with contacts to n -SiC were available for further testing (e.g., from not being used at 1200 °C). Using the additional pieces from contacts to n -SiC and diced pieces from the more lightly-doped p -SiC ohmic samples, a furnace run was performed at 1000 °C for 2 h of continuous annealing. As seen in Table 3–8 and Figure 3–28, the ρ_c values were of comparable range to the values from 0.5 and 1 h, $\rho_c \approx 10^{-5} \Omega\text{cm}^2$ for n -SiC and $\rho_c \approx 10^{-3} \Omega\text{cm}^2$ for p -SiC. The exception to the stable ρ_c values out 2 h was W50:Ni50/ p -SiC, which showed a $\sim 2 \times$ increase from 0.5 h. These ρ_c values for 2 h were extracted from the average gap spacings (within 2 μm) from pieces of the same samples, which should result in an upper bound of 10% error. With this thermal stability, especially for W51:Ni49, out to 2 h, W:Ni contacts to SiC show promise for future studies at 1000 °C.

Table 3–8. Average specific contact resistance ρ_c \pm standard error (σ/\sqrt{N}) in Ωcm^2 . Total annealing time was 2 h in Ar at 1000 °C.				
	W51:Ni49	N	W50:Ni50	N
$N_A = 1 \times 10^{20} \text{ cm}^{-3}$	$(1.50 \pm 0.04) \times 10^{-3}$	15	$(1.22 \pm 0.02) \times 10^{-3}$	15
$N_D = 2 \times 10^{19} \text{ cm}^{-3}$	$(9.8 \pm 0.7) \times 10^{-6}$	14	$(2.1 \pm 0.1) \times 10^{-5}$	15

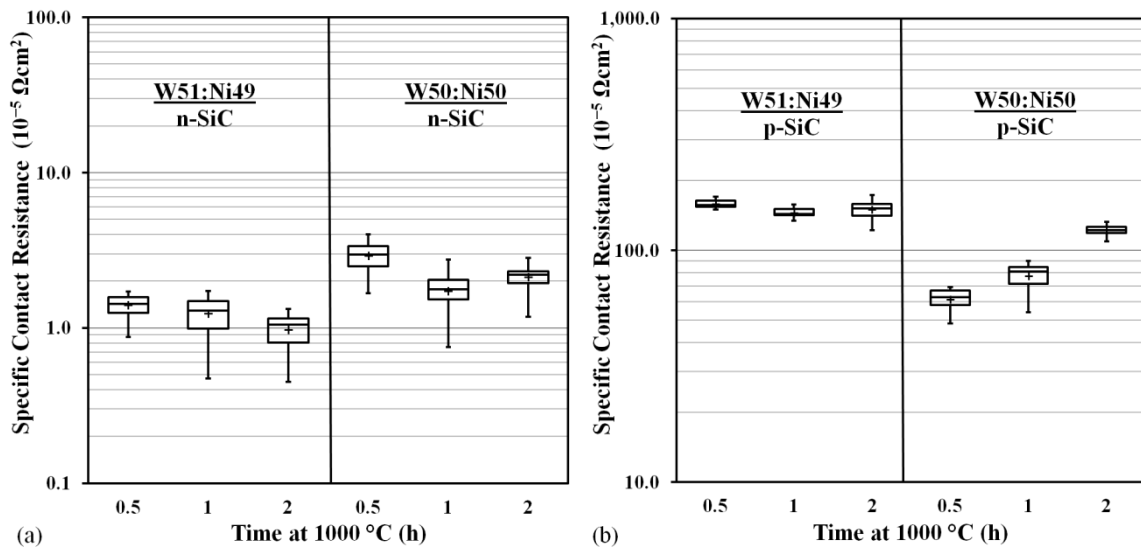


Figure 3–28. Specific contact resistances for W:Ni contacts on (a) n -SiC with $N_D = 2 \times 10^{19} \text{ cm}^{-3}$ and (b) p -SiC with $N_A = 1 \times 10^{20} \text{ cm}^{-3}$ out to 2 h total annealing at 1000 °C.

The boxplot shown has the averages marked with plus signs. Note: The plots in (a) and (b) have different scales.

3.4.1.2 Aging at 600 °C

Further annealing at 600 °C would provide benchmarking with previous studies in the literature for more terrestrial high-temperature applications. Annealing at 600 °C in Ar was conducted in the tube furnace at PSU described in Section 2.1.4 with an in-line gettering furnace. All samples previously annealed at 1000 °C through 1 h were annealed

in the same furnace run. Samples were loaded into the tube furnace and sufficiently purged before ramping up to temperature. The tube furnace was held at 600 °C for 100 h under 100 sccm of ultra-high purity Ar, and then allowed to cool over the course of several hours with continuous Ar flow. These samples were then measured with a reduced current range of ± 5 mA to avoid scorching.

The simultaneous W:Ni ohmic contacts on SiC with the highest doping levels saw increases of the average ρ_c values $\sim 4 \times$ for W51:Ni49/*p*-SiC, and $\sim 2 \times$ for W51:Ni49/*n*-SiC and W50:Ni50. The ρ_c values are detailed in Table 3–9 and plotted in Figure 3–29 which shows the solid range of values $\sim 10^{-5} \Omega\text{cm}^2$ with increases in spread. Despite the large increase for W51:Ni49 on *p*-SiC (likely due to unintentional oxidation), the W50:Ni50 contacts in this study show promise for thermally stable ohmic contacts to *p*-SiC over 100 h (without Al as used in [102]).

Table 3–9. Average specific contact resistance ρ_c \pm standard error (σ/\sqrt{N}) in Ωcm^2 . Total annealing time was 1 h at 1000 °C before 100 h of aging at 600 °C in Ar.				
	W51:Ni49	N	W50:Ni50	N
$N_A = 3 \times 10^{20} \text{ cm}^{-3}$	$(9.6 \pm 2.4) \times 10^{-5}$	8	$(2.1 \pm 0.4) \times 10^{-5}$	12
$N_D = 2 \times 10^{19} \text{ cm}^{-3}$	$(2.8 \pm 0.2) \times 10^{-5}$	15	$(4.6 \pm 0.5) \times 10^{-5}$	12
$N_A = 1 \times 10^{20} \text{ cm}^{-3}$	$(1.1 \pm 0.1) \times 10^{-3}$	9	$(5.5 \pm 0.6) \times 10^{-4}$	10

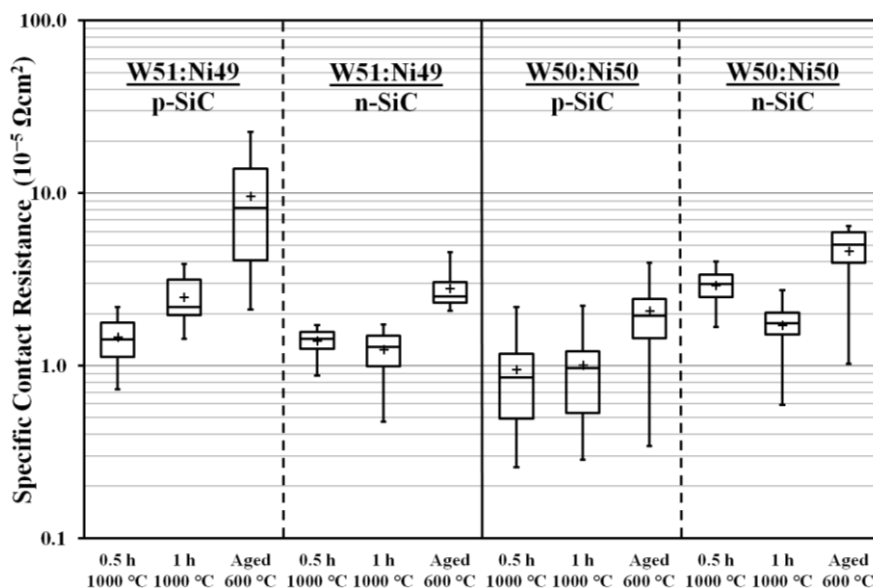


Figure 3–29. Specific contact resistances for W:Ni contacts on *p*-SiC with $N_A = 3 \times 10^{20} \text{ cm}^{-3}$ and *n*-SiC with $N_D = 2 \times 10^{19} \text{ cm}^{-3}$ after 1 h total annealing at 1000 °C and then 100 h at 600 °C. The boxplot shown has the averages marked with plus signs.

The ohmic contacts to *p*-SiC with $N_A = 1 \times 10^{20} \text{ cm}^{-3}$ showed small decreases in the ρ_c values after the 100 h aging run. Measurements from these TLM structures also demonstrated increases in spread, as can be seen in Table 3–9 and Figure 3–30. With the moderate decrease in these values together with the contacts to *n*-SiC and W50:Ni50/*p*-SiC depicted in Figure 3–29, the W:Ni contacts show further promise of being thermally stable on both conductivity types through 100 h at 600 °C. Further annealing for another 100 h was performed for all reported samples in the same manner, but current–voltage measurements have now become quite difficult to obtain without scorching the surfaces. As some of the surfaces have gained visible colors, enhanced oxidation has put an end to this aging study.

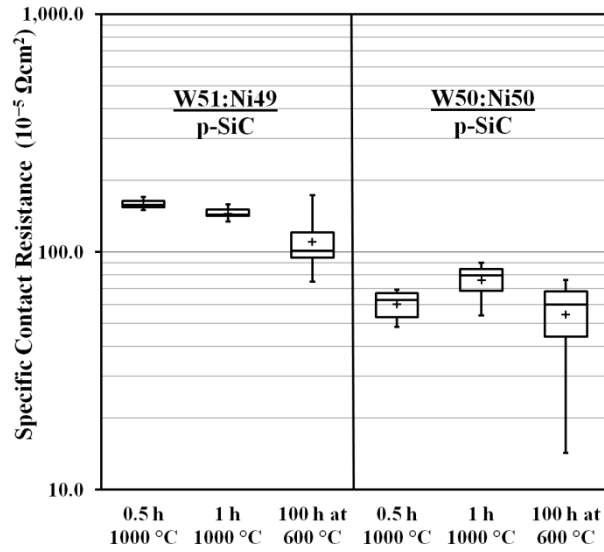


Figure 3–30. Specific contact resistances for W:Ni contacts on p -SiC with $N_A = 1 \times 10^{20} \text{ cm}^{-3}$ after 1 h total annealing at 1000 °C and then 100 h at 600 °C. The boxplot shown has the averages marked with plus signs.

3.4.2 Addition of Carbon in diffusion layers

As seen in the later aging at 600 °C, the thermal stability of W:Ni ohmic contacts can be dramatically inhibited by oxidation. As noted in the above literature review, the search for diffusion barriers has been complicated. Pt/TaSi₂ has been a promising choice for both Ti [15] and Ni [17] contacts to SiC. The offered AES depth profiles in these papers suggest interdiffusion as one possible reason for degradation. In this dissertation, preliminary examination of short time frame kinetics was used to study graphene as a barrier to both oxygen and interdiffusion of atoms. In graphene research, graphene has been formed from surface segregation out of bulk C-doped Pt [154] as well as from vapor-phase incorporated C both in Pt sheets [155] and in sputtered thin films [156].

While some of these studies involved higher temperatures (e.g., 1200 °C+) than desired for layers above the W:Ni ohmic contacts, these temperatures were employed during vapor incorporation and C redistribution. Co-sputtering of Pt and C in a thin film layer would allow for the C to be already incorporated into the film. This incorporation method should allow C to segregate from the films at lower annealing temperatures. The hypothesized change in film structure is shown in Figure 3–31. Subsequent metallization of additional noble metal layers would then limit graphene oxidation. The presence of C was pursued through the use of AES surface scans, with shifts expected in the characteristic C (KLL) peak shape [157].

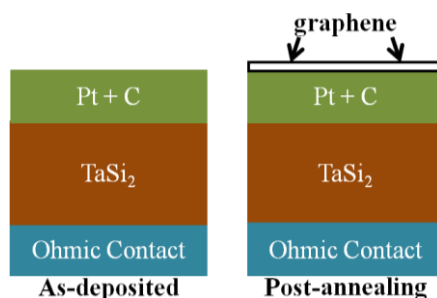


Figure 3–31. Representation of the hypothesized change in diffusion barrier structure after annealing. The C in the co-sputtered Pt+C layer would segregate to the surface and form graphene.

A composite target from Plasmaterials, Inc., was used to sputter 400 nm TaSi₂ at 0.7 Å/s and 6 mTorr in the DC Magnetron Sputtering System at PSU seen in Figure 2–1(b). In order to assure an appreciable quantity of C, Pt and C were co-sputtered on top of the TaSi₂ without breaking vacuum. Initial Pt+C co-sputtered layers had been placed on top of unannealed W:Ni layers in order to use the contact anneal to also form

graphene. After 15 min in a tube furnace at 1000 °C, all species mixed together without clear formation of any discernible structure in the W:Ni region (not shown). Additional samples were prepared as separate layers and on already annealed Si/W50:Ni50/SiC at 1150 °C. Further investigation failed to produce evidence of graphene on the surface (or any significant C at all). These studies were continued as the small size of C may stuff the Pt grain boundaries and limit oxygen diffusion in that way [144], [152].

During the 10.2 mTorr deposition of 205 nm Pt and C, the shutter was deliberately closed in front of the Pt at four points to ensure distributed layers of C. This sequence of Pt+C/C/Pt+C/C/Pt+C/C/Pt+C/C/Pt+C will be referred to as the PtC 9 layer. The deposition rates and thicknesses are detailed in Table 3–10. The AES depth profile seen in Figure 3–32 verified the presence of C in these layers after deposition. During AES depth profiles, Ta2 (MNN) and Pt3 (MNN) Auger elemental windows were added to the ones collected in the W:Ni study. Pt is known to preferentially sputter during AES depth profiling, with a result that the Pt thickness appears less than the actual value. Any abrupt termination of the AES depth profile upon reaching the SiC can be attributed to the nature of the substrate. These studies were performed on a test grade, undoped SiC wafer—and the semi-insulating nature of the substrate would charge in the Auger spectrometer after the substrate was encountered.

Table 3–10. Sputtering rates and thicknesses for the 9 layers of Pt+C and C. Layers are ordered from air down to TaSi ₂ .		
Layer	Rate (Å/s)	Thickness (Å)
Pt & C	0.8	514
C	0.1	100
Pt & C	0.8	300
C	0.1	51
Pt & C	0.8	300
C	0.1–0.2	86
Pt & C	0.8–0.9	302
C	0.1–0.2	100
Pt & C	0.9	300

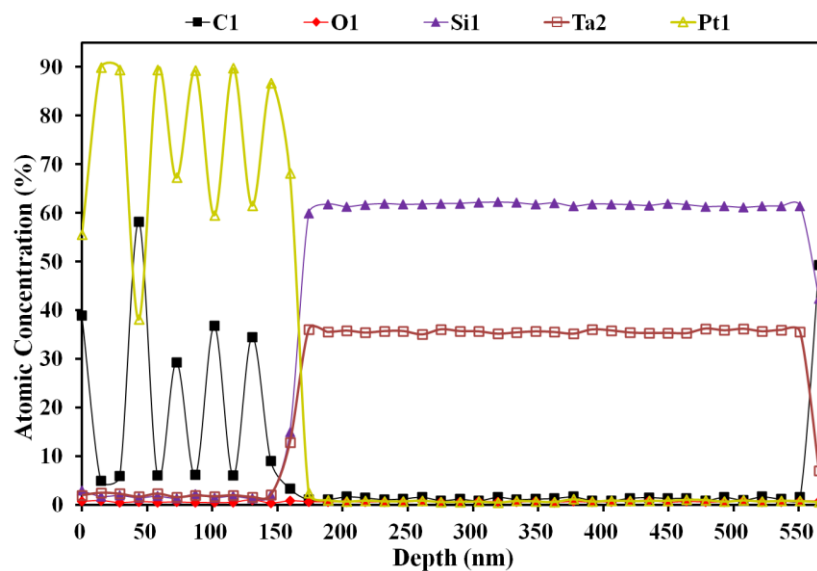


Figure 3–32. AES depth profile for the as-deposited PtC 9 layer on TaSi₂.

Annealing was performed using the vacuum AS-One rapid thermal annealing (RTA) system discussed in Section 2.1.4. Initial peak annealing times of 300 s were chosen in order to monitor early stages of any reactions or interdiffusion. Annealing at 900 °C (the upper trusted limit of the RTA) saw complete failure of the diffusion barriers to protect the ohmic contact as seen in Figure 3–33. The Ta reacted to form a tantalum carbide (TaC_x), as indicated from the C (KLL) peak shape (Figure 2–22(a)). The C peak shape actually indicates carbidic carbon throughout all of the metal layers. Meanwhile, the Pt formed a platinum silicide (PtSi_x) with the liberated Si, as indicated in the Pt peak shape. The W, Ni, and Pt diffused throughout the entire metal stack below the TaC_x through the SiC interface, disrupting the W:Ni ohmic contact phases.

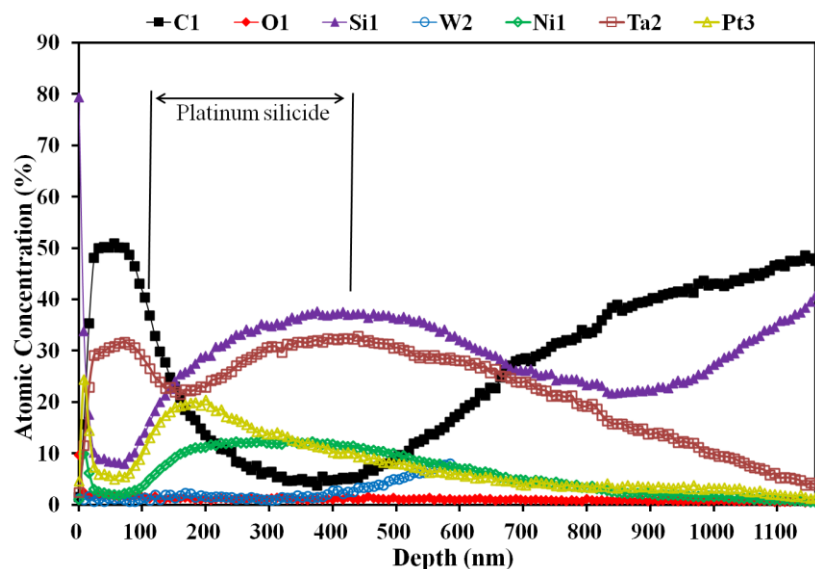


Figure 3–33. AES depth profile for PtC 9 layer/ TaSi_2 /Si/W:Ni/SiC annealed at 900 °C in the RTA for 300 s under Ar. PtSi_x has formed along with TaC_x above the region dominated by TaSi_2 . The TaC_x has nearly replaced the Pt as the upper layer. The Si/W:Ni contact had been previous annealed at 1150 °C.

The RTA annealing temperature was reduced to 600 °C for 300 s in Ar. This temperature demonstrated excellent stability for the ohmic contact layer as well as the TaSi₂. Annealing additional films to the RTA limit of 1 h at 600 °C demonstrated the same behavior, as seen in Figure 3–34. The Si/W:Ni contact had been previously annealed at 1150 °C for 0.5 h, resulting in carbidic carbon regions, which appear to be fields of W_xNi_yC and Ni+Si+C. The Pt has once again formed a silicide with non-carbidic C accumulating inside the layer (Figure 2–22(b)). The TaSi₂ has prevented diffusion of the Pt into the metal contact. Some slight Ta can be seen inside the ohmic contact region; however, Ta has been known to form substitutional carbides with W [158].

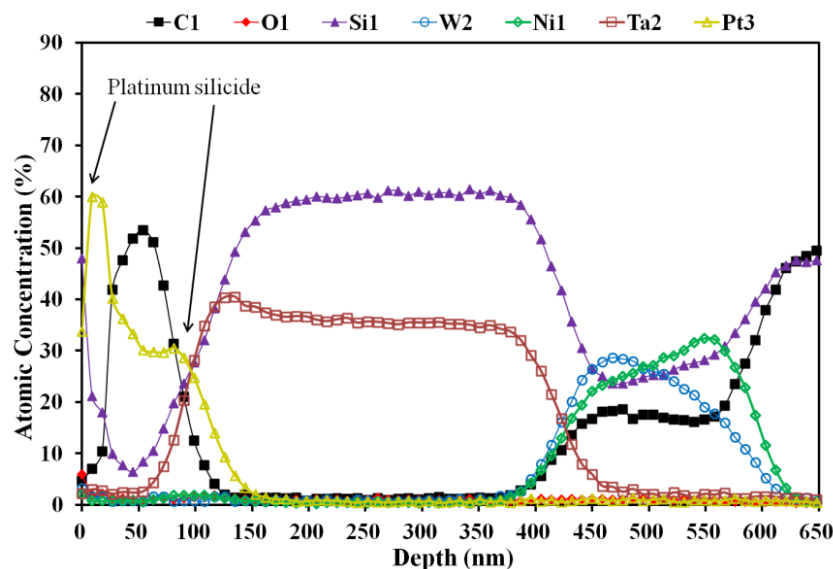


Figure 3–34. AES depth profile for PtC 9 layer/TaSi₂/Si/W:Ni/SiC annealed in the RTA for 1 h at 600 °C under Ar. PtSi_x has formed above the stable TaSi₂. The Si/W:Ni contact had been previous annealed at 1150 °C.

Additional annealing for 300 s suggested the transition point from stable diffusion barriers above the metal contact to complete interdiffusion occurs between 700 °C (similar to Figure 3–34) and 800 °C (similar to Figure 3–33). As can be seen in Figure 3–34 above, the Pt appears to have formed into a silicide as the uppermost layer. While this silicide may have promise for limiting O diffusion, the Ta is likely to oxidize upon encountering O as it approaches the top of the diffusion barrier [149]. Also, as noted in the Pt/Ir/Pt/TaSi₂ study [146], the Pt layer forming solely a silicide layer will limit the potential for wire bonding.

3.5 Conclusions

W:Ni alloys formed ohmic contacts on *p*-4H-SiC after annealing at temperatures from 1000–1200 °C, and on *n*-4H-SiC at temperatures from 1000–1150 °C. The simultaneous ohmic contact formation of W:Ni alloys resulted in comparable ρ_c values on both doping types after near identical fabrication and processing. Most ρ_c values for the nominally W51:Ni49 and W50:Ni50 contacts were $< 3 \times 10^{-5} \Omega\text{cm}^2$, with the lowest average values occurring at $(7.3 \pm 0.9) \times 10^{-6} \Omega\text{cm}^2$ for W51:Ni49/*p*-SiC and $(6.8 \pm 0.9) \times 10^{-6} \Omega\text{cm}^2$ for W50:Ni50/*n*-SiC after annealing in Ar at 1150 °C. These low specific contact resistances for refractory alloy contacts offer promise for SiC sensors and electronics for extremely high-temperature applications. Additionally, the similar ρ_c values for both compositions considering the ~5 at.% spread in film composition demonstrated the robustness of these materials for fabricating ohmic contacts.

After annealing at 1000 °C, W51:Ni49 and W50:Ni50 contacts formed a tungsten–nickel–carbide phase, W_xNi_yC , previously unreported in thin films on SiC. A significant amount of Si was detected in the W_xNi_yC phase with AES, likely altering the lattice parameter. After annealing at 1100 °C and above, W-rich structures corresponding to WC can be seen on Ni-rich fields corresponding to W_xNi_yC with dissolved Si—all above Ni+Si+C regions that might be amorphous or a poorly crystallized nickel silicide plus graphite. The XEDS mapping has demonstrated the continuous nature of W and Ni across the contact regions. Further study is required on the role of W_xNi_yC in ohmic contact formation on 4H-SiC, especially with the benefits of simplifying the fabrication processes of bipolar junction devices with comparable ρ_c values to both conductivity types.

Additional thermal aging was performed at 1000–1150 °C, wherein only the ohmic contacts annealed at 1000 °C retained low ρ_c values $\sim 10^{-5} \Omega\text{cm}^2$. All ohmic contacts did retain their ohmic behavior. Investigation of the ohmic contacts to *n*-SiC and *p*-SiC with lighter doping demonstrated thermal stability through 2 h at 1000 °C. All contacts annealed at 1000 °C were further examined for 100 h at 600 °C in Ar, with moderate increases in ρ_c but still $\approx 10^{-5} \Omega\text{cm}^2$ for the simultaneous contacts. The contacts to *p*-SiC with $N_A = 1 \times 10^{20} \text{ cm}^{-3}$ demonstrated small decreases in ρ_c after 100 h such that values were $\approx 10^{-4}$ – $10^{-3} \Omega\text{cm}^2$, but all $\lesssim 1 \times 10^{-3} \Omega\text{cm}^2$. Further aging was limited by oxidation in all samples. Pt and C co-sputtered layers along with TaSi₂ were investigated as a possible alternative to Pt/TaSi₂ as diffusion barriers. This work focused on limiting early interdiffusion between atomic species. While these layers demonstrated early thermal stability at 600 °C, they do not appear to constitute any significant

improvement over the already studied Pt/TaSi₂ scheme [15], [17] without characterizing the electrical behavior.

Chapter 4

Nickel Contacts to Polar Indium Nitride

This chapter discusses metal–semiconductor interfaces for polar semiconductors, focusing experimentally on metal–indium nitride interactions. The most promising results of this chapter have been published in K. C. Kragh-Buetow, X. Weng, E. D. Readinger, M. Wraback, and S. E. Mohny, “Effects of polarity on Ni/InN interfacial reactions,” *Appl. Phys. Lett.*, vol. 102, 021607 (2013), which should be cited as appropriate. The assistance of Dr. Xiaojun Weng is greatly appreciated for his tutelage, guidance, and help in conducting transmission electron microscopy. Gratitude is also expressed to Dr. E. D. Readinger and Dr. M. Wraback who provided the polar indium nitride for this work, as well as Jillian Woolridge for assistance in reading the German literature.

4.1 Semiconductor Polarity in the Literature

Various semiconductors have non-centrosymmetric hexagonal crystal structures, resulting in anisotropic polarity along the c -axis. A spontaneous polarization exists along the c -axis, resulting in two polar faces, (0001) and (000 $\bar{1}$). The (0001) face is negatively polar, and the polarization vector points away from this face. Known polar semiconductors include 4H- and 6H-silicon carbide (SiC); and members of the Group III–nitrides (III–N): aluminum nitride (AlN), gallium nitride (GaN), and indium nitride

(InN). The discussion of polarity involves crystal planes, which are separate discussions from which chemical species terminates the surface of the material [159]. While the crystal structure shown for InN in Figure 1–7 does have the same terminating species as species labeling faces, polarity is independent of species termination.

Both SiC and III–N semiconductors have great research interest and applications. As discussed elsewhere in this dissertation, SiC has great interest for high-temperature and high-power devices. Meanwhile, III–N semiconductors have numerous optoelectronic and sensor applications. Development of III–N semiconductors has progressed rapidly in the past two decades, driven in part by the tremendous commercial success of light-emitting diodes (LEDs) fabricated from these semiconductors. Laser diodes, solar cells, ultraviolet detectors, and high electron mobility transistors (HEMTs) have also been demonstrated.

The vast majority of research on polar semiconductors has involved (0001) or metal-face orientations of the wurtzite crystals. However, research interest has grown for (000 $\bar{1}$) or nonmetal-face orientations as well as nonpolar orientations. Researchers working with the nonpolar faces of III–Ns have demonstrated LEDs with greater external quantum efficiency compared to diodes with *c*-axis orientations [30]. Previous investigators have studied the influence of polarity on some intrinsic properties, fabrication procedures, and performance metrics. Even with generalizations from the literature to date, each material and situation still requires observations to learn the extent to which polarity affects processing and properties. A selection of the polarity literature focusing on SiC, III–Ns, and InN will follow.

The influence of polarity starts with growth. The seeded sublimation growth for SiC on a Si-face seed crystal encourages 6H-SiC, and growth on a C-face encourages 4H-SiC [12]. Even just studying surface reconstruction after etching [11] or surface graphitization after Si evaporation [160] reveals different configurations for {0001} 6H-SiC. Polarity impacts the growth of InN as well, with In-face growing on Si-face SiC and N-face growing on C-face SiC [161] [162]. This same impact on InN polarity can be seen with GaN templates: In-face InN on Ga-face GaN and N-face InN on N-face GaN [163].

N-face InN is considered more promising due to the higher growth temperature, which should result in a higher thermal stability [28]. N-face InN films also exhibit surfaces with less roughness during MOCVD growth compared to In-face InN due to the different configurations of dangling bonds [163]. Presuming N-terminated surfaces, the In atoms on N-face InN prefer to grow islands of InN together into continuous films; however, the bond arrangements in In-face InN encourage 3D growth on the islands that leaves the rough surfaces [163]. Both faces of InN do show high surface electron mobility, although this mobility is higher for N-face InN [28].

Beyond growth, the influence of surface polarity has been studied on both processing steps and device performance. The growth of silicon oxide on C-face 4H-SiC has been found to be not only rougher [164] than that of Si-face but also faster [4], [165]. Studies of Si-face SiC metal-oxide-semiconductor field effect transistors (MOSFETs) have demonstrated the problem of low channel mobility compared to Si-based devices [166]. Studies have now demonstrated superior channel mobility for C-face SiC [165], [167]. Subsequent aspects of C-face device fabrication being researched have included

device structure variations [168], post-deposition annealing [169], the effect of gate oxidation conditions on voltage parameters [170], and the impact of oxidation on trap densities [171], [172]. Previous III–N experiments have already demonstrated that the rate of chemical etching with potassium hydroxide [173] and hot phosphoric acid [174] are both faster on N-face GaN. Both studies indicated significant etching of the N-face, with only mild surface morphology changes to the Ga-face. The polar faces of GaN also exhibited differences in the adsorption of oxygen [175] and the response time of GaN Schottky diode H₂ sensors [176].

Metal–semiconductor interfaces are another area of device fabrication showing effects from polarity. For Si-face 6H-SiC, the Schottky barrier heights are generally lower than the C-face for both the same metal and overall—except for Au [11],[177]. Schottky contacts of Ni, Ti, and Al were separately studied on *n*-type 6H-SiC [178]. This study indicated the same phases formed for Ti and Al on both faces, albeit with different extents; furthermore, the Ni formed a silicide only on C-face SiC [178]. Al–Ti ohmic contacts to {0001} 6H-SiC showed differences in metal–semiconductor reactivity, forming Al₃Ti on both faces but Al₂Ti and Ti₃SiC₂ only on the Si-face [179]. Studying a variety of metals as metal/carbon/*n*-4H-SiC resulted in ohmic contacts from Ni and Co for both faces, along with Cr and NiCr only on Si-face [180]. A more recent side-by-side study of Ni ohmic contacts to *n*-4H-SiC demonstrated slightly lower specific contact resistances for Si-face after annealing for 1 min between 950–1050 °C [181]. In direct opposition to SiC, Schottky contacts of Pt on {0001} GaN have resulted in higher barrier heights for Ga-face GaN as compared to N-face GaN [182]. Lower ohmic contact resistance has also been shown for N-face GaN HEMTs as compared to Ga-face GaN

HEMTs [183]. *In-situ* photoelectron spectroscopy studies on MBE-grown InN planes showed differences in both the surface states and band alignments for N-face and In-face InN, which in turn alter the semiconductor work functions [184]. With variations between material systems, further experimental research is necessary to understand the specific effects from polar semiconductor faces.

The effect of crystallographic orientation and polarity on phase reactions in metal contacts has not yet been fully explored for III–N semiconductors. This dissertation will focus on a side-by-side investigation of Ni–InN interfaces. The thermal stability of nickel contacts on the polar $\{0001\}$ orientations of InN has been investigated. The phases formed with annealing have been monitored using X-ray diffraction (XRD) and a transmission electron microscope (TEM). In the TEM, both images and selected area diffraction (SAD) patterns have been collected as well as images and X-ray energy dispersive spectrometry (XEDS) in scanning transmission electron microscopy (STEM) mode. This research focuses on the materials characterization, as contacts would likely be ohmic due to Fermi-level pinning above the conduction band [19].

4.2 Experimental Procedures for InN

The InN films were grown by plasma-assisted molecular beam epitaxy (PA-MBE) in the (0001) and (000 $\bar{1}$) orientations on templates of GaN upon sapphire substrates, as seen in Figure 4–1. Further discussions about In-face and N-face from the same lab can be found in publications about In-face [161] and N-face growth [34], [162].

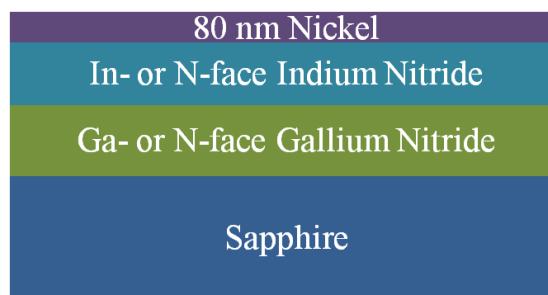


Figure 4–1. Representation of the distinct material layers involved in the polar face study: Ni deposited on InN films that were grown on GaN layers of the same polarity.

The nickel films were deposited using e-beam evaporation. Before annealing, the samples were degreased in acetone, isopropanol, and DI water before being blown dry with N_2 . Samples were annealed at 400 °C in a tube furnace with ultra-high purity N_2 gas that had passed through a gettering furnace to dry the gas even further.

Grazing Incidence XRD (GIXRD) geometry allowed for stronger signals from the thin film layers, with any substrate peaks present being diminished in intensity. All GIXRD patterns were collected with a PANalytical X’Pert Pro MPD θ – θ goniometer with Cu $K\alpha$ radiation. Data were collected between $2\theta = 20$ – 70° for durations of ~16 min. The minimum omega angle $\omega = 0.2^\circ$ was employed because of how thin the Ni films were.

Cross-sectional TEM specimens were prepared by mechanical polishing followed by Ar ion milling. Electron diffraction, conventional and STEM imaging, and XEDS were performed on a JEOL 2010F field-emission TEM equipped with an EDAX® XEDS system. Spectra were collected in STEM mode using an electron probe with a nominal

size of 1 nm. High-angle annular dark-field (HAADF) STEM images were collected with an inner detector radius of 63.5 mrad. The accelerating voltage was 200 kV.

4.3 Ni/InN Results and Discussion

The TEM images of the as-deposited Ni/InN samples are shown in Figure 4–2 for (a) In-face and (b) N-face films, which reveal sharp Ni/InN interfaces for both structures. Figures 4–2(c) and (d) are SAD patterns for Ni/In-InN and Ni/N-InN structures, respectively, collected from regions containing both the Ni film and the InN layer. In each SAD pattern, the three rings correspond to (111), (002), and (220) reflections of Ni. Reflections in addition to those from Ni and InN were not found. Therefore, reactions were not detected between the as-deposited Ni films and the InN layers with different polarities.

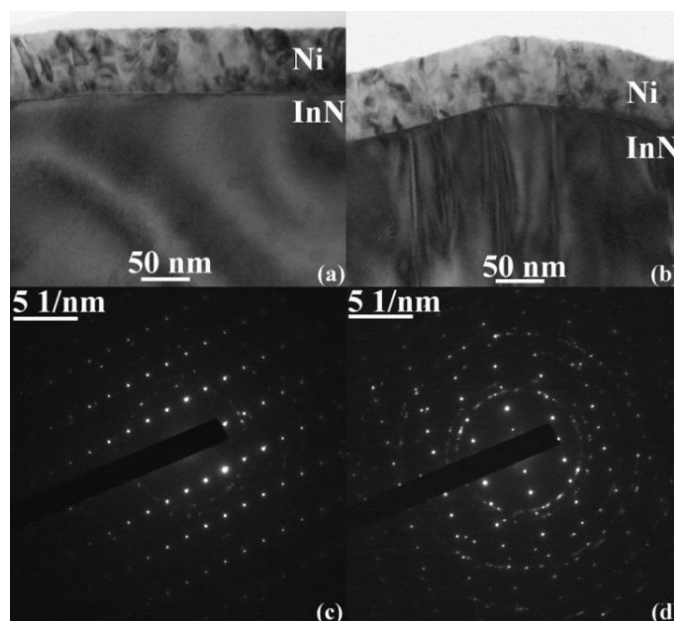


Figure 4–2. TEM bright-field images of Ni films on (a) In-face and (b) N-face InN with SAD of (c) In-face and (d) N-face InN for as-deposited samples. Each diffraction pattern consists of a set of diffraction spots from the single crystalline InN and diffraction rings from the polycrystalline Ni film.

The GIXRD patterns seen in Figures 4–3(a) and (b) were collected with the same conditions for the as-deposited and annealed samples. The sample position in the instrument affected the presence or absence of low-intensity substrate peaks in each pattern. For both polar orientations, the as-deposited patterns showed prominent Ni peaks, with the appearance of peaks from underlying layers dependent on sample position during data collection. In-face and N-face samples from the same Ni deposition run were annealed in N₂ together in a quartz boat within a tube furnace for 1 h at 400 °C. Thermodynamic predictions of metal–InN ternary phase diagrams [185] predicted the formation of nickel indides. As seen in Figure 4–3(a), only Ni peaks were visible for the

annealed In-face sample at 400 °C, suggesting no reaction at the Ni/InN interface. For the annealed N-face sample shown in Figure 4–3(b), however, the Ni peaks diminished alongside the appearance of peaks from a different phase.

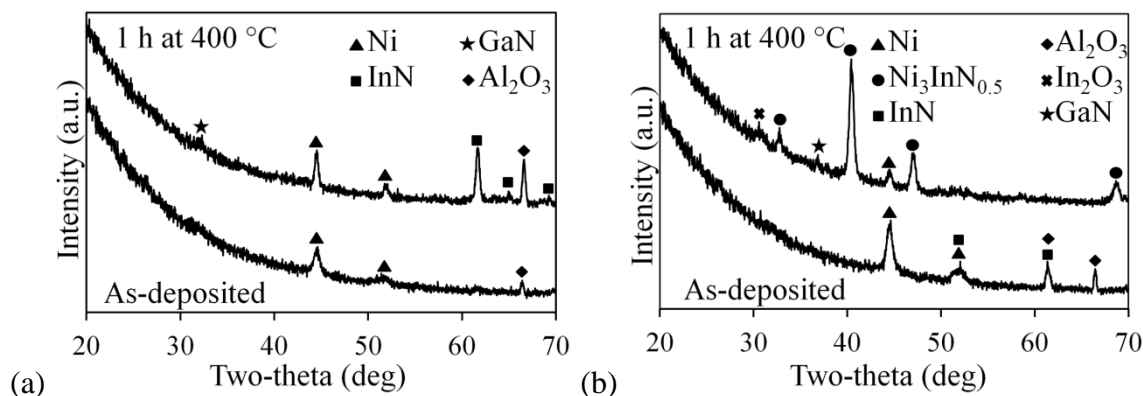


Figure 4–3. GIXRD plots collected from (a) In-face Ni/InN samples and (b) N-face Ni/InN samples both as-deposited and after 1 h at 400 °C.

The peaks from the emergent phase closely match those of $\text{Ni}_3\text{InN}_{0.5}$. The $\text{Ni}_3\text{InN}_{0.5}$ ternary phase was previously identified in a bulk alloy annealed in N_2 at 600 °C [186]. The cubic nickel–indium–nitride ternary phase possessed an anti-perovskite structure ($Pm\bar{3}m$) with a lattice constant of 0.384 nm [186]. The E1_2 perovskite structure has also been referenced as the $\text{L}'1_2$ structure to emphasize the nitrogen addition to the middle of the ordered face-centered cubic Ni_3In [186], [187], as seen in Figure 4–4. Therefore, the GIXRD results suggest the formation of a Ni_3InN_x ternary phase upon the annealing of Ni on N-face InN. This phase identification is supported by the SAD and XEDS results discussed below.

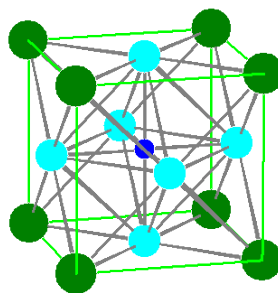


Figure 4–4. The anti-perovskite structure of the nickel–indium–nitride ($\text{Ni}_3\text{InN}_{0.5}$) ternary phase. Green circles at the corners are In atoms, light blue circles are Ni atoms, and the smaller blue circle is a N atom. *Made in PowderCell* [22].

TEM images of the Ni/InN structures annealed at 400 °C for 1 h are shown in Figures 4–5(a) and (b) for Ni on In-face and N-face InN, respectively. A microstructural difference was observed for the two samples after annealing. Significant microstructural change was not observed for the Ni film on In-face InN after annealing. However, the top of the film on N-face InN became porous upon the 400 °C annealing. Furthermore, the Ni/In-face InN interface remains sharp after annealing, yet the interface between the Ni film and the N-face InN layer appears to be wavy. Figure 4–5(c) is the SAD pattern of the annealed Ni/In-face InN structure, collected from a region near both the metal film and InN. The pattern is similar to that of the as-deposited structure, in which only Ni and InN reflections were observed. On the other hand, the Ni diffraction rings vanished in the SAD pattern of the annealed Ni/N-face InN structure, as shown in Figure 4–5(d). Instead, diffraction rings from a separate phase were identified. Indexing of these rings indicates that this distinct phase has a face-centered cubic symmetry, with a lattice parameter of ~0.39 nm. This measured lattice constant of the emergent phase from

electron diffraction is similar to the previously reported bulk lattice constant (0.384 nm) of $\text{Ni}_3\text{InN}_{0.5}$ [186], suggesting that the phase is likely Ni_3InN_x . These results are consistent with the GIXRD results and indicate that In-face and N-face InN have different thermal stabilities in contact with Ni.

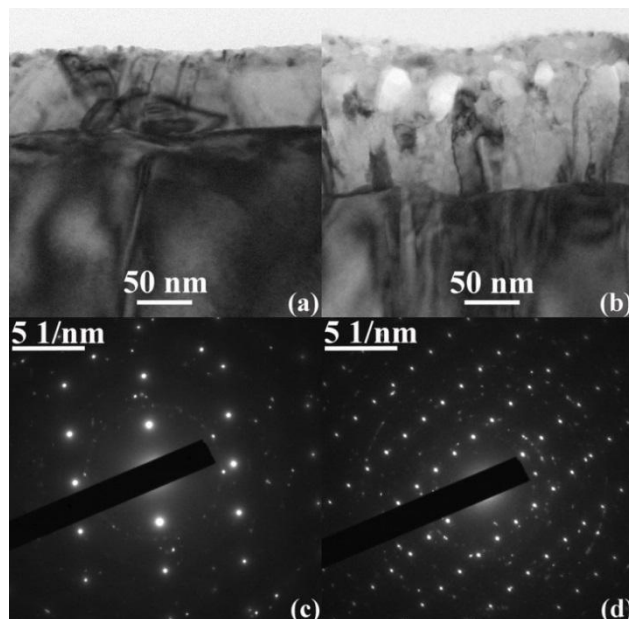


Figure 4–5. TEM bright-field images of Ni films annealed at 400 °C for 1 h on (a) In-face and (b) N-face InN along with SAD of the (c) In-face and (d) N-face InN samples. Diffraction spots are from InN, and rings are from the Ni-bearing layers.

The differences in the microstructural and chemical evolution of the Ni films on InN layers with different polarities were further confirmed by STEM and XEDS characterization. As shown in Figure 4–6(a), the Z-contrast HAADF STEM image of the Ni/In-face InN structure reveals a nearly homogeneous contrast for the Ni film. Furthermore, the Ni/InN interface appears sharp. These features suggest insignificant reaction between the Ni film and the In-face InN layer upon annealing at 400 °C. In

contrast, the STEM image of the Ni/N-face InN structure shown in Figure 4–6(b) reveals porosity near the top of the Ni-bearing film as well as the wavy Ni/N-face InN interface, indicating again that a reaction occurred during annealing. The film porosity may have arisen from uneven fluxes of different atoms in opposite directions creating vacancies in the film that coalesced to form voids. Another possibility for the origin of the film porosity is nitrogen evolution during annealing.

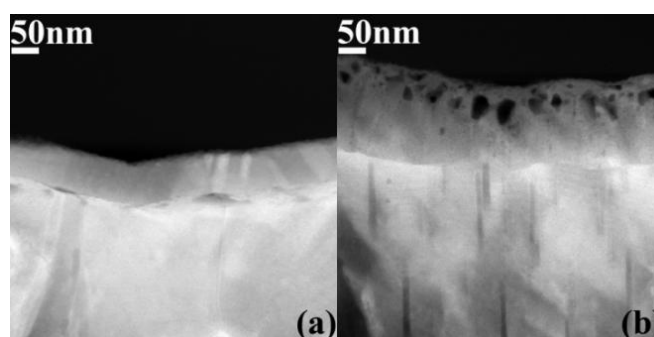


Figure 4–6. HAADF images for Ni films annealed for 1 h at 400 °C on (a) In-face and (b) N-face InN highlight the difference in microstructure.

While in STEM mode, XEDS was collected across the metal–InN interfaces. Figures 4–7(a) and (b) depict the site-specific XEDS location and counts for In-face InN while Figures 4–7(c) and (d) display the XEDS location and counts from the N-face InN interface. Figure 4–7(e) compares XEDS spectra collected from the metal films in the two annealed samples. Only Ni peaks were observed in the spectrum from the metal film on the In-face InN layer. The spectra for the In-face further support that N is not detected in the Ni film and not merely omitted from the counts of Figure 4–7(b). However, both N and In peaks were identified besides Ni for the metal film on the N-face layer. The

spectrum from the annealed N-face sample further confirms the presence of the Ni_3InN_x ternary phase seen in the XRD and SAD patterns.

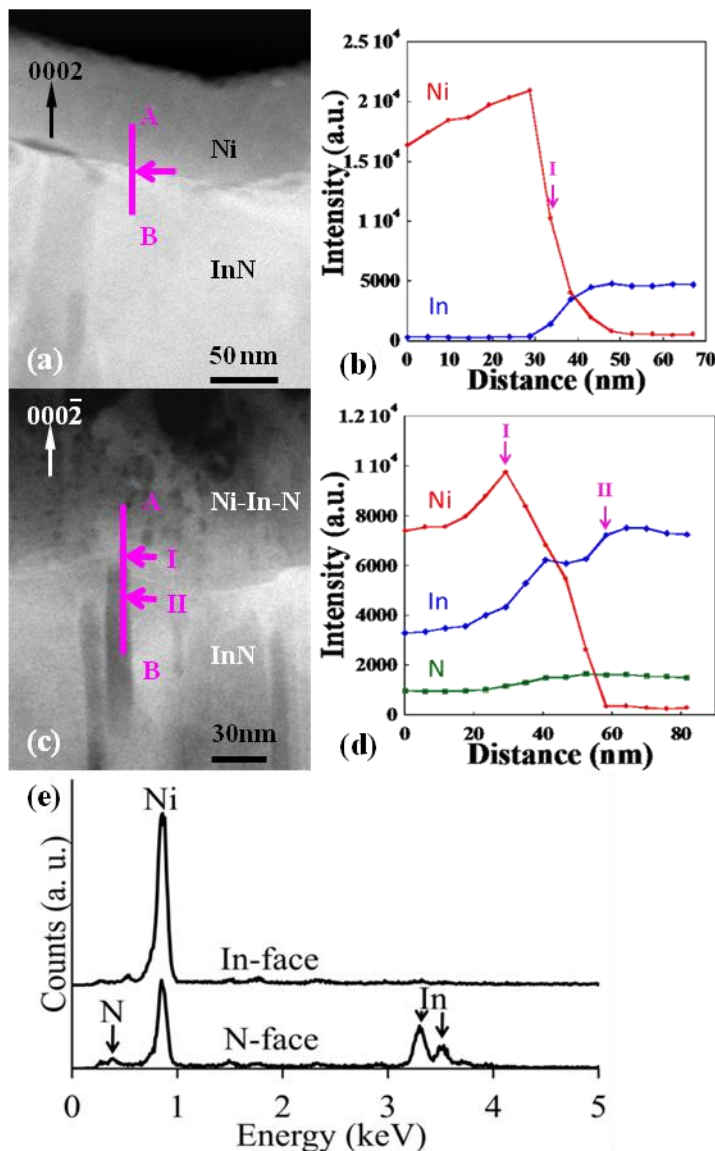


Figure 4–7. HAADF images for (a) In-face and (c) N-face, with site-specific XEDS line profiles through (b) Ni/InN and (d) $\text{Ni}_3\text{InN}_x/\text{InN}$ on the respective images. Lastly, (e) the XEDS spectra from the annealed Ni films reveal only a Ni peak for the In-face sample while N and In peaks are also observed for the N-face sample.

Characterization of the Ni/InN interface was also performed at different conditions than those already presented here. Ni films on N-face InN were annealed for 1 h at 350 °C in N₂. The XRD plot shown in Figure 4–8 only shows the presence of unreacted Ni. When this same sample was annealed again at 375 °C for 1 h, the Ni₃InN_x phase can be found as well as unreacted Ni as seen in Figure 4–8. Thus, the Ni/N-face InN begins to form Ni₃InN_x at a temperature between 350 °C and 375 °C.

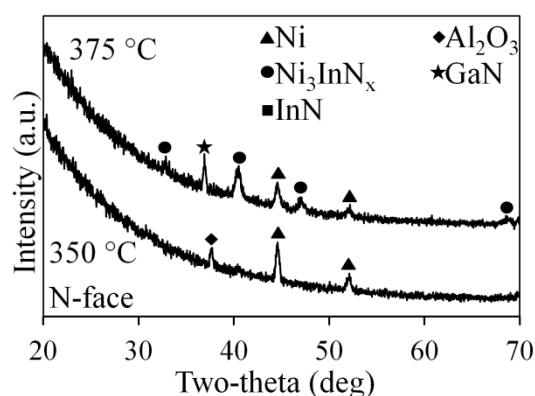


Figure 4–8. GIXRD plot of Ni on (000 $\bar{1}$) InN annealed at 350 °C and 375 °C for 1 h in N₂, revealing a reaction phase between the Ni and InN beginning at the higher temperature.

Further Ni/InN samples of the same thickness were prepared by sputtering to investigate the effects of longer time and higher temperature on both faces together. During the longest time for annealing tested here, the Ni₃InN_x phase persisted for 4 h at 400 °C—still present only on the N-face InN as seen in Figure 4–9(a). After annealing for 1 h at 450 °C, Ni on the In-face sample remained unreacted. For the N-face sample, the Ni layer was completely reacted into Ni₃InN_x as seen in Figure 4–9(b). All samples annealed at 450 °C, however, experienced oxidation. In Figure 4–9(b), GIXRD shows

the formation of indium oxide (In_2O_3) in both In-face and N-face samples. The formation of nickel oxide (NiO) was also suggested, as no InN or Al_2O_3 peak had been seen previously next to the Ni (111) peak ($2\theta \approx 44.6^\circ$).

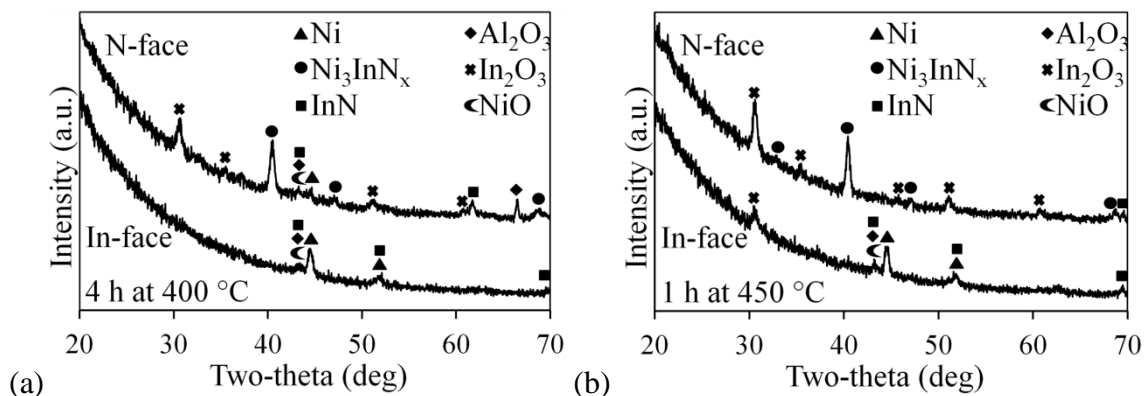


Figure 4–9. GIXRD plots of Ni on {0001} InN annealed (a) at 400 °C for 4 h in N_2 , and (b) 450 °C for 1 h in N_2 , revealing that In_2O_3 and NiO were among the phases formed.

The surface texture became porous in the inhomogeneous Ni containing layers, as seen in the HAADF images in Figure 4–10(a) and (d) for both In-face and N-face InN. XEDS line profiles through the HAADF images in Figure 4–10(b) and (e) show significant Ni, In, and O presence for In-face and the presence of Ni, In, N, and O for N-face. The estimated atomic concentrations shown in Figure 4–10(c) and (f) have large uncertainties in the N and O concentrations due to overlapping peaks. The N is overstated in the films and the O overstated in the InN. The oxygen may stem from incomplete cleaning of the InN surfaces, or trapped residual gas during sputtering. The SAD (not shown) also demonstrated the presence of the cubic In_2O_3 and NiO for both samples. Such samples were not investigated further. Higher temperatures than 450 °C

were not attempted due to approaching the decomposition temperature of InN near 500 °C [188].

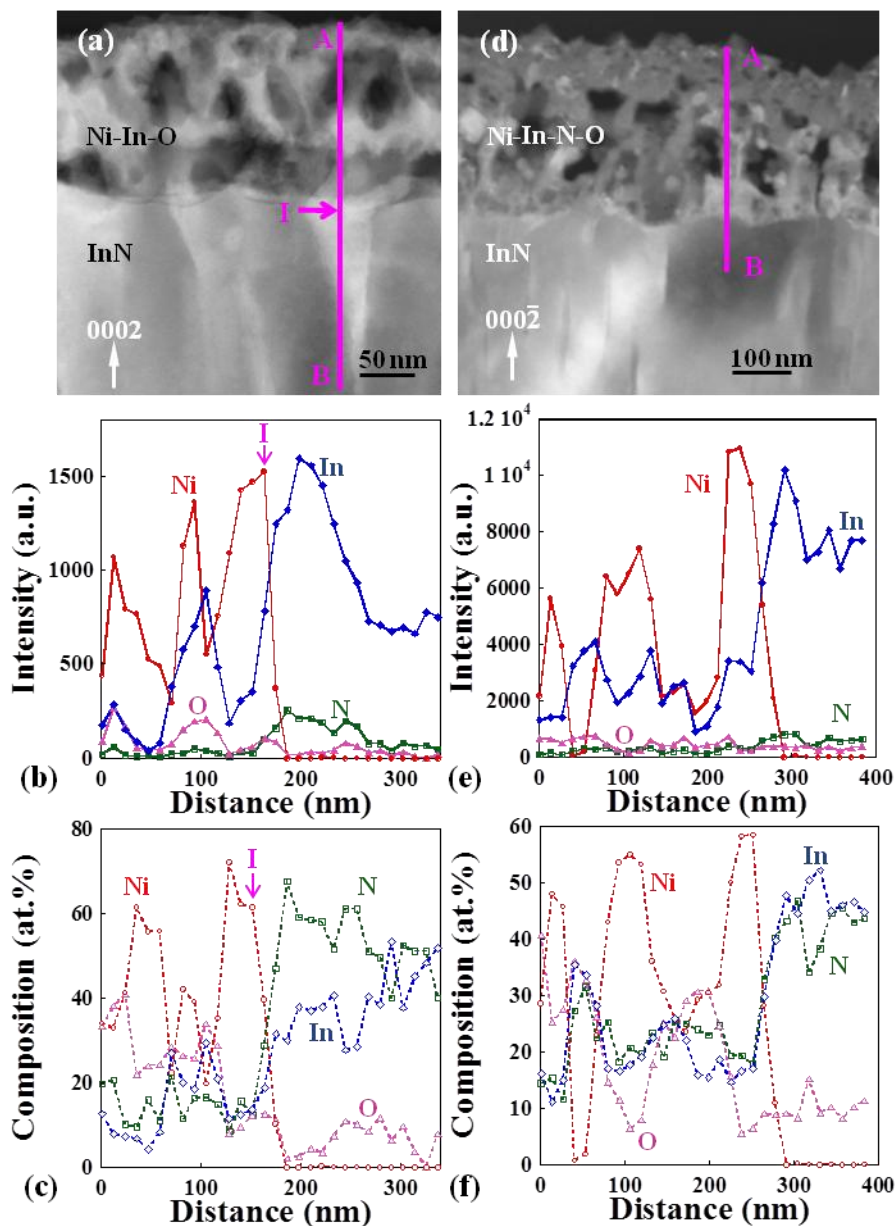


Figure 4–10. HAADF images for (a) In-face and (d) N-face InN annealed at 450 °C, with site-specific XEDS line profiles through (b) Ni–In–O and (e) Ni–In–N–O on the respective images. The estimated compositions from the XEDS are seen in (c) and (f), respectively; however, the N is overstated in the films and the O overstated in the InN.

4.4 Conclusions

This dissertation supports the hypothesis that distinct faces of {0001} InN demonstrate different thermal stability with Ni after annealing at 400 °C. The N-face of InN displayed greater reactivity in forming a Ni_3InN_x ternary phase, whilst the In-face remained unreacted and did not form the ternary phase. The N-face InN may be more reactive due to a favorable configuration of bonds at the InN surface, as explained elsewhere for GaN in the context of etching [173]. One might also speculate that the greater density of crystal defects in the N-face InN (see Figure 4–2(b)) contributes to its enhanced reactivity; however, the reaction was no more advanced at defect sites than elsewhere. In addition to understanding further why polarity controls reactivity, future work should also explore whether the effect of polarity on phase formation can be clarified or generalized to other metal–polar semiconductor material systems.

Chapter 5

Summary and Future Work

This chapter serves to summarize the experimental work and conclusions performed in this dissertation. Future work for all sections will also be proposed.

5.1 Summary

Numerous industries have interest in the development of high-temperature electronics. From spaceflight to drilling to power plants, a critical need exists for new materials and techniques to deliver high-temperature electronics and sensors. As a wide bandgap semiconductor, SiC is an attractive material for such applications; however, low-resistance thermally stable ohmic contacts are amongst the microfabrication techniques that must be improved for long-term operation. In addition, ohmic contacts to SiC presently require different materials for each conductivity type, complicating the microfabrication process.

In this dissertation, W:Ni thin films were investigated as simultaneous ohmic contacts to both *p*- and *n*-4H-SiC. During initial testing, *p*-SiC epilayers with various dopant concentrations were studied with four metal contact compositions. With W as a control, alloys with nominal compositions in at.% of W90:Ni10, W51:Ni49, and W50:Ni50 were also tested. The near equi-atomic compositions demonstrated a ~5 at.% spread in measured film compositions and provided the most promising results. Linear

TLM structures were fabricated and annealed at 1000–1200 °C for 0.5 h in Ar. The *p*-SiC epilayers with the highest doping of $3 \times 10^{20} \text{ cm}^{-3}$ demonstrated ohmic behavior for all annealing temperatures using the metal alloys with near equi-atomic compositions. TLM structures on *n*-SiC doped at $2 \times 10^{19} \text{ cm}^{-3}$ were fabricated only for these compositions.

The near equi-atomic nominal compositions of W51:Ni49 and W50:Ni50 displayed simultaneous ohmic contact behavior with similar electrical resistances after annealing at 1000–1150 °C. The comparable ρ_c values $\sim 10^{-6}$ – $10^{-5} \text{ } \Omega\text{cm}^2$ for W:Ni alloys to both *p*- and *n*-4H-SiC are also lower than any other known simultaneous ohmic contacts to both conductivity types. The lowest ρ_c values occurred after annealing at 1150 °C. The lowest ρ_c values were $(7.3 \pm 0.9) \times 10^{-6} \text{ } \Omega\text{cm}^2$ for *p*-SiC and $(6.8 \pm 0.9) \times 10^{-6} \text{ } \Omega\text{cm}^2$ for *n*-SiC. Using the FIB and the SEM to examine cross-sections of the W:Ni contacts indicated the ρ_c values may actually be up to 20% lower for *p*-SiC and up to 10% lower for *n*-SiC based on the penetration depth of the W:Ni into the SiC epilayers. The results offer promise of enabling SiC sensors and electronics for extremely high-temperature applications, in addition to further simplifying the fabrication processes of bipolar junction devices.

Both structural and compositional materials characterization was performed on the phases formed in the films after annealing. XRD with a microdiffractometer revealed a cubic tungsten–nickel–carbide ternary phase $\text{W}_x\text{Ni}_y\text{C}$ after annealing at all temperatures for the nominal W51:Ni49 and W50:50 compositions. The phase also appeared for W90:Ni10 compositions, along with tungsten silicide and tungsten carbide. The $\text{W}_x\text{Ni}_y\text{C}$ phase was the predominant phase present in the XRD patterns for the near equi-atomic

compositions. In fact, W_xNi_yC was the only metal-bearing phase present after annealing at 1000 °C for the nominal W51:Ni49 and W50:Ni50 compositions. AES later confirmed this phase as having dissolved Si, which helps explain the mass balance expected from W:Ni reacting with SiC. Micrographs from the SEM demonstrated this surface morphology to be smooth and mostly devoid of surface features.

The samples annealed at 1100–1200 °C demonstrated a distinct surface morphology in the electron microscopy. Lath-like structures of thin parallelograms as well as larger plate-like structures of both triangles and irregular polygons were clearly visible amongst more featureless ‘field’ regions. In XEDS mapping in the SEM, the plate- and lath-like structures were W-rich, while the field regions were Ni-rich. XRD indicated the clear formation of WC alongside the W_xNi_yC in samples annealed at 1150 °C and 1200 °C, and possibly after annealing at 1100 °C. AES indicated that the laths and plates were composed of WC, while the fields consisted of W_xNi_yC with Si. The AES also demonstrated possible nickel silicides buried at the interface with SiC, along with considerable dissolved C.

Additional thermal aging of the ohmic contacts was carried out at 1000–1150 °C and 600 °C. The TLM structures annealed at 1100 °C and 1150 °C remained ohmic with considerable increase in ρ_c after a second 0.5 h of annealing (1 h total). The samples annealed for an additional 0.5 h at 1000 °C demonstrated considerable stability. Further aging of the TLM structures annealed at 1000 °C was conducted for 100 h at 600 °C in Ar. The ρ_c values had increased, but were still low, approaching mid $10^{-5} \Omega\text{cm}^2$ range for both conductivity types. The decay of samples may have been aggravated by

repeated probing of the samples and aggressive cleaning from adhesives used in electron microscopy.

TLM structures on *p*-SiC epilayer doped at $1 \times 10^{20} \text{ cm}^{-3}$ had been fabricated at the same time as the *n*-type structures. These samples also proved to be ohmic after 0.5 h annealing at 1000–1150 °C, albeit with higher $\rho_c \approx 10^{-4}$ – $10^{-3} \Omega\text{cm}^2$. Additional aging of these contacts for a second 0.5 h resulted in stable values for TLMs annealed at 1000 °C and smaller increases (1.5 – $2.4 \times$) in ρ_c for those annealed at higher temperatures. As-deposited TLMs from these samples were annealed with TLMs on *n*-SiC for a 2 h continuous anneal, further showing promise of W:Ni/SiC thermal stability for hypersonic flight (1000 °C+). The TLMs on the more lightly-doped *p*-SiC annealed for 1 h total were also aged for 100 h at 600 °C, showing a moderate decrease in ρ_c values.

Although Pt/TaSi₂ diffusion barriers have previously been used for contacts to SiC, in this study C was added to Pt in an attempt to either stuff grain boundaries in Pt (a path for short-circuit diffusion) or precipitate graphene as an additional diffusion barrier. Although stable in Ar for both 1 h at 600 °C and 300 s at 700 °C above the annealed W:Ni contacts, the layers reacted significantly with W:Ni after short times at 800 °C. The results did not suggest that they would provide an improvement over otherwise identical barriers without C.

Another materials property with great impact on future electronics is polarity in semiconductors. Non-centrosymmetric crystal structures, such as wurtzite, have polar faces, with a spontaneous polarization. Polar semiconductors include 4H- and 6H-SiC, along with the Group III–nitrides. Polarity along the *c*-axis has caused the different {0001} crystal faces to exhibit distinct behavior from growth to processing to devices.

Generalizations of these properties, however, beyond ‘polarity causes different behavior’ seem to vary between material systems. Thus, further research is necessary to understand the impact of polarity on electronic device properties.

While conventional SiC research has been mostly performed on Si-face SiC, interest in the C-face has grown since the measurement of higher mobilities than in Si-face MOSFETs [165], [167]. With interest in C-face devices, the impact of polarity on metal–semiconductor interfaces must be understood. Unfortunately, high-quality, doped C-face SiC epilayers are still difficult to obtain. In this dissertation, metal contacts were investigated on a different polar semiconductor, indium nitride (InN), which offers promise for optoelectronics.

The work here hypothesized that Ni deposited on the two different {0001} polar faces of InN might exhibit different thermal stability after annealing. 80 nm thin films of Ni were evaporated in the same deposition run for In-face and N-face InN. These samples were annealed in a tube furnace under N₂ gas flow at 400 °C for 1 h. The materials characterization was carried out using GIXRD as well as SAD, STEM imaging, and XEDS in a TEM. The GIXRD showed Ni/N-face InN reacted into a Ni₃InN_x ternary phase after annealing. Meanwhile, Ni/InN on In-face remained unreacted. TEM samples analyzed using SAD supported the findings from XRD. XEDS through the interface in STEM mode indicated the presence of In and N only in the film on N-face InN. This dichotomy has confirmed the greater reactivity of the N-face for InN. Additional annealing demonstrated the formation of Ni₃InN_x at a temperature between 350 °C and 375 °C. The Ni remained unreacted for In-face InN for separate samples annealed at 1 h at 450 °C and even 4 h at 400 °C. The formation of In₂O₃ and NiO, however, occurred

during the 450 °C analysis, as seen in GIXRD, SAD, and XEDS. The Ni-bearing films also underwent various changes in microstructure with annealing at both 400 °C and 450 °C, as seen in the STEM mode HAADF images.

5.2 Future Work

5.2.1 Future work for contacts to Silicon Carbide

While the phase identification and the surface morphology have been studied in this dissertation, future W:Ni ohmic contact work should investigate the nature of electrical conduction and the role of each phase formed during annealing. Further exploration using tunneling AFM should be performed from a larger set of samples in order draw statistical conclusions about the pathways of current through the W:Ni contacts and to eliminate the confounding artifact of topography.

Further investigation into understanding the W:Ni ohmic contacts must seek out the mechanism behind such behavior, especially for *p*-SiC. Prevalent theories for ohmic contact formation to SiC have been very material specific. Learning more about the band structure of W_xNi_yC (metal or semiconductor) would be worthy of investigation. If W_xNi_yC is a metal, the Schottky barrier height formed on lightly-doped SiC could be measured. If it is a semiconductor, its role in lowering the resistance of the ohmic contact and band alignments between W_xNi_yC and SiC could also be explored. Furthermore the

band structure of W_xNi_yC must be understood both as the only phase present (at 1000 °C) and as part of a multi-phase structure (1100–1200 °C).

In the simultaneous study, contacts to p -SiC with the highest doping of $N_A = 3 \times 10^{20} \text{ cm}^{-3}$ were demonstrated. Contacts to p -SiC with $N_A = 1 \times 10^{20} \text{ cm}^{-3}$ were also shown to be ohmic for 1000–1150 °C. These samples have lowered the threshold of p -type doping for ohmic contact formation to N_A between $7 \times 10^{19} \text{ cm}^{-3}$ and $1 \times 10^{20} \text{ cm}^{-3}$ for the processes discussed in this dissertation. Further experimentation could more accurately determine the necessary doping for low ρ_c values on p -SiC (and n -SiC). Additional studies of the barrier heights (Φ_B) for W:Ni contacts to even more lightly-doped SiC would help discern the current transport mechanisms as well (e.g., field emission vs. thermionic field emission).

The distinct W:Ni surface morphology demonstrated considerable variation mentioned only briefly in this dissertation. Some contacts have exhibited tightly-knit networks of laths, while others have large amalgamations of triangular plates. Other successful ohmic contacts reported in this work have larger W_xNi_yC (field) regions with fewer WC regions. Further study could understand the factors behind these varied extents of WC reaction and any correlations to the electrical behavior. The possibility of local variations in chemical composition could also be investigated.

For hypersonic flight applications, anticipating short-term temperatures of 1000 °C [5], the results in this study have shown promise through 1 h annealing of W:Ni on both p - and n -SiC. Further thermal stability out to 2 h at 1000 °C was seen for contacts to n -SiC and the additional p -SiC samples ($N_A = 1 \times 10^{20} \text{ cm}^{-3}$). These results suggest testing future W:Ni contacts to p -SiC for longer durations would be quite

promising—especially if the comparable low contact resistances on SiC with conductivity types persists with high enough N_A levels.

While results for 100 h of aging at 600 °C were presented here, testing at 1000 h would be a considerable benchmark, especially for contacts to p -SiC. Fabrication of new TLM test structures would be important, as the aged contacts in this study had already been aged at 1000 °C before use and may show smaller (or larger) increases in ρ_c . Future plans for preserving ohmic contact behavior would be best tested in a sealed glass ampoule, back-filled with Ar gas.

As discussed in this dissertation, the W:Ni ohmic contacts will need diffusion barriers to ensure their survival in high-temperature oxidizing environments. While Pt/TaSi₂ may be one such barrier to study, further exploration should only be done with the Pt/Ir overlayers [146] to allow for wire bonding. Pt/TiN bilayers [16] in air should also be explored for the W:Ni ohmic contacts. Once barrier layers have been developed, thermal stability testing for W:Ni/SiC should also include harsh environment testing. In particular, surviving the toxic gas environments found on other planets such as Venus would be an important achievement for SiC electronics.

5.2.2 Future work for polar semiconductors

The Ni/InN reaction into the Ni₃InN_x phase studied in this dissertation should affect the electrical properties of any Ni/InN ohmic contacts. Future work should study the impact of polar faces on the specific contact resistances using linear TLM structures. These electrical properties can also be studied after annealing.

Both materials and electrical characterization can be extended to other metal–InN interfaces. Preliminary investigation of Ta on N-face and In-face InN with XRD demonstrated the same phases were formed; however, oxidation of these samples was not definitively ruled out. Further exploration of metals and polarity was investigated for Ni–GaIn in an undergraduate student mentored by this author for a senior thesis [185] and found the formation of different nickel gallides on the two polar faces. From these limited investigations, exploration of other metals with semipolar and polar InN must be considered before generalizing rules about polarity for InN and other III–N semiconductors. Research on metal–InN interfaces must also investigate possible mechanisms responsible for any differences, such as band structure [184] and bonding configurations in polar semiconductors [163], [173].

The greater reactivity in terms of phase formation for N-face InN stands in contrast to the trend of greater Si-face reactivity for SiC [179], [180]. As more researchers investigate C-face SiC for device applications, stable ohmic contacts to the C-face may necessitate different materials than for the Si-face. While W:Ni alloys have been studied as successful simultaneous ohmic contacts to Si-face SiC, the resulting contacts may be different for W:Ni alloys on C-face SiC. The potentially delayed (or accelerated) reaction kinetics could affect the phases formed as well as the contact resistance. While the Si-face was shown to have lower ρ_c [181] for one study, this observation may not be universal. While N-face InN has shown greater reactivity in this dissertation, the results also point towards the necessity of further study concerning the effect of polarity on other metal contacts for a variety of polar semiconductors.

References

- [1] G. E. Moore, "Cramming more components onto integrated circuits," *Electronics*, vol. April 19, [Reprint Proc. IEEE 1998], pp. 114–117, 1965.
- [2] T. Balint, T. Thompson, J. Cutts, and J. Robinson, "Venus Exploration Opportunities within NASA's Solar System Exploration Roadmap," *Venus Entry Probe Workshop*. [Online]. Available: <http://hdl.handle.net/2014/38734>.
- [3] P. Neudeck, R. Okojie, and L. Chen, "High-temperature electronics—a role for wide bandgap semiconductors?," *Proc. IEEE*, vol. 90, no. 6, pp. 1065–1076, 2002.
- [4] R. Maboudian, C. Carraro, D. G. Senesky, and C. S. Roper, "Advances in silicon carbide science and technology at the micro- and nanoscales," *J. Vac. Sci. Technol. A Vacuum, Surfaces, Film.*, vol. 31, no. 5, 050805, 2013.
- [5] L. Evans, R. Okojie, and D. Lukco, "Development of an Extreme High Temperature *n*-Type Ohmic Contact to Silicon Carbide," *Mater. Sci. Forum*, vol. 717–720, pp. 841–844, 2012.
- [6] P. G. Neudeck, S. L. Garverick, D. J. Spry, L.-Y. Chen, G. M. Beheim, M. J. Krasowski, and M. Mehregany, "Extreme temperature 6H-SiC JFET integrated circuit technology," *Phys. Status Solidi*, vol. 206, no. 10, pp. 2329–2345, Oct. 2009.
- [7] C.-M. Zetterling, Ed., *Process Technology for Silicon Carbide Devices*. INSPEC, 2002.
- [8] G. W. Hunter, P. G. Neudeck, R. S. Okojie, G. M. Beheim, V. Thomas, L. Chen, D. Lukco, C. C. Liu, B. Ward, and D. Makel, "Development of SiC Gas Sensor Systems," in *State-of-the-Art Program on Compound Semiconductors XXXVI and Wide Bandgap Semiconductors for Photonic and Electronic Devices and Sensors II (Electrochemical Society Proceedings Volume 2002-3)*, R. F. Kopf, F. Ren, E. B. Stokes, H. M. Ng, A. G. Baca, S. J. Pearton, and S. N. G. Chu, Eds., The Electrochemical Society, Inc., 2002, pp. 93–111.
- [9] L. Porter and R. Davis, "A critical review of ohmic and rectifying contacts for silicon carbide," *Mater. Sci. Eng. B*, vol. 34, pp. 83–105, 1995.
- [10] J. Crofton, L. Porter, and J. Williams, "The Physics of Ohmic Contacts to SiC," *Phys. status solidi*, vol. 202, pp. 581–603, 1997.
- [11] Z. C. Feng and J. H. Zhao, Eds., *Silicon carbide : materials, processing, and devices*. Taylor & Francis, 2004.
- [12] Z. C. Feng, Ed., *SiC power materials : devices and applications*. Springer, 2004.
- [13] T. V. Blank and Y. A. Goldberg, "Mechanisms of current flow in metal–semiconductor ohmic contacts," *Semiconductors*, vol. 41, no. 11, pp. 1263–1292, Nov. 2007.
- [14] D. K. Schroder, *Semiconductor Material and Device Characterization*, 3rd ed. IEEE Press, 2006.

- [15] R. S. Okojie, D. Lukco, Y. L. Chen, and D. J. Spry, "Reliability assessment of Ti/TaSi₂/Pt ohmic contacts on SiC after 1000 h at 600 °C," *J. Appl. Phys.*, vol. 91, no. 10, pp. 6553–6559, 2002.
- [16] W. Daves, A. Krauss, V. Häublein, A. J. Bauer, and L. Frey, "Structural and Reliability Analysis of Ohmic Contacts to SiC with a Stable Protective Coating for Harsh Environment Applications," *ECS J. Solid State Sci. Technol.*, vol. 1, no. 1, pp. P23–P29, Jan. 2012.
- [17] A. Virshup, F. Liu, D. Lukco, K. Buchholt, A. Lloyd Spetz, and L. M. Porter, "Improved thermal stability observed in Ni-based ohmic contacts to n-type SiC for high-temperature applications," *J. Electron. Mater.*, vol. 40, no. 4, pp. 400–405, 2011.
- [18] S.-K. Lee, E.-K. Suh, N.-K. Cho, H.-D. Park, L. Uneus, and A. Lloyd Spetz, "Comparison study of ohmic contacts to 4H-silicon carbide in oxidizing ambient for harsh environment gas sensor applications," *Solid. State. Electron.*, vol. 49, no. 8, pp. 1297–1301, Aug. 2005.
- [19] J. Wu, "When group-III nitrides go infrared: New properties and perspectives," *J. Appl. Phys.*, vol. 106, no. 1, 011101, 2009.
- [20] B. G. Streetman and S. Banerjee, *Solid State Electronic Devices*, 6th ed. Prentice Hall, 2005.
- [21] G. Y. Robinson, "Schottky Diodes and Ohmic Contacts for the III–V Semiconductors," in *Physics and Chemistry of III-V Compound Semiconductor Interfaces*, C. Wilmsen, Ed., Springer, 1985, pp. 73–163.
- [22] W. Kraus and G. Nolze, "POWDER CELL – a program for the representation and manipulation of crystal structures and calculation of the resulting X-ray powder patterns," *Journal of Applied Crystallography*, 1996. [Online]. Available: http://www.ccp14.ac.uk/ccp/web-mirrors/powdcell/a_v/v_1/powder/e_cell.html.
- [23] G. L. Harris, Ed., *Properties of Silicon Carbide*. INSPEC, 1995.
- [24] T. T. Mnatsakanov, L. I. Pomortseva, and S. N. Yurkov, "Semiempirical Model of Carrier Mobility in Silicon Carbide for Analyzing Its Dependence on Temperature and Doping Level," *Semiconductors*, vol. 35, no. 4, pp. 394–397, 2001.
- [25] T. T. Mnatsakanov, M. E. Levinshtein, L. I. Pomortseva, and S. N. Yurkov, "Carrier mobility model for simulation of SiC-based electronic devices," *Electr. Eng.*, vol. 17, pp. 974–977, 2002.
- [26] A. G. Bhuiyan, A. Hashimoto, and A. Yamamoto, "Indium nitride (InN): A review on growth, characterization, and properties," *J. Appl. Phys.*, vol. 94, no. 5, pp. 2779–2808, 2003.
- [27] N. Miller, J. W. Ager III, R. E. Jones, H. M. Smith, M. A. Mayer, K. M. Yu, M. E. Hawkrige, Z. Liliental-Weber, E. E. Haller, W. Walukiewicz, W. J. Schaff, C. Gallinat, G. Koblmüller, and J. S. Speck, "Electrical and electrothermal transport in InN: The roles of defects," *Phys. B Condens. Matter*, vol. 404, no. 23–24, pp. 4862–4865, 2009.
- [28] T. B. Fehlbeg, G. Koblmüller, G. A. Umana-Membreno, C. S. Gallinat, B. D. Nener, J. S. Speck, and G. Parish, "Multiple carrier transport in N-face indium nitride," *Phys. Status Solidi*, vol. 245, no. 5, pp. 907–909, 2008.
- [29] T. B. Fehlbeg, C. S. Gallinat, G. A. Umana-Membreno, G. Koblmüller, B. D.

- Nener, J. S. Speck, and G. Parish, "Effect of MBE Growth Conditions on Multiple Electron Transport in InN," *J. Electron. Mater.*, vol. 37, no. 5, pp. 593–596, 2007.
- [30] J. S. Speck and S. F. Chichibu, "Nonpolar and Semipolar Group III Nitride-Based Materials," *MRS Bull.*, vol. 34, no. 05, pp. 304–312, 2009.
- [31] M. Ohring, *Materials Science of Thin Films: Deposition and Structure*, 2nd ed. Academic Press, 2002.
- [32] Kurt J. Lesker Company, "Technical Information: Vacuum Technology." [Online]. Available: http://www.lesker.com/newweb/menu_techinfo.cfm?section=tech&init=skip.
- [33] T. M. Christensen, "Physics of Thin Films," *University of Colorado at Colorado Springs*, 2000. [Online]. Available: <http://www.uccs.edu/~tchrste/courses/PHYS549/549lectures/sputtertech.html>.
- [34] X. Q. Shen, T. Ide, S. H. Cho, M. Shimizu, S. Hara, H. Okumura, S. Sonoda, and S. Shimizu, "Realization of Ga-polarity GaN films in radio-frequency plasma-assisted molecular beam epitaxy," *J. Cryst. Growth*, vol. 218, pp. 155–160, 2000.
- [35] R. Dormaier and S. E. Mohny, "Factors controlling the resistance of Ohmic contacts to *n*-InGaAs," *J. Vac. Sci. Technol. B*, vol. 30, no. 3, 031209, 2012.
- [36] C. Hammond, *The basics of crystallography and diffraction*, 2nd ed. Oxford University Press, 2001.
- [37] S. A. Speakman, "Basics of X-ray Powder Diffraction," *Massachusetts Institute of Technology*. [Online]. Available: <http://prism.mit.edu/xray/oldsite/tutorials.htn>.
- [38] E. Ryba, "X-ray Crystallography and Diffraction," Fall Semester Lectures, The Pennsylvania State University, 2012.
- [39] T. Mitsunaga, "X-ray thin-film measurement techniques: II. Out-of-plane diffraction measurements," *Rigaku J.*, vol. 25, no. 1, pp. 7–12, 2009.
- [40] B. B. He, *Two-dimensional x-ray diffraction*. Wiley, 2009.
- [41] "D/max-RAPID: Fast X-ray Diffractometer with Area Detector," *Rigaku J.*, vol. 16, no. 1, pp. 51–57, 1999.
- [42] *D/MAX RAPID II (RINT RAPID II) Instruction Manual*, 1st ed. Rigaku Corporation, 2005.
- [43] *D/MAX RAPID II Control Software RAPID/XRD Instruction Manual.*, 1st ed. Rigaku Corporation, 2005.
- [44] W. Stroud, *Rigaku AreaMax 2.0 Summary*, 1st ed. Rigaku Corporation, 2005.
- [45] D. B. Williams and C. B. Carter, *Transmission Electron Microscopy*, 2nd ed. Springer, 2009.
- [46] J. C. Vickerman and I. S. Gilmore, Eds., *Surface Analysis—The Principal Techniques*, 2nd ed. Wiley, 2009.
- [47] *Handbook of Auger Electron Spectroscopy*, 3rd ed. Physical Electronics Industries, 1995.
- [48] N. Lundberg and M. Östling, "CoSi₂ ohmic contacts to *n*-type 6H-SiC," *Solid. State. Electron.*, vol. 38, no. 12, pp. 2023–2028, 1995.
- [49] N. Lundberg and M. Östling, "Thermally stable low ohmic contacts to *p*-type 6H-SiC using cobalt silicides," *Solid. State. Electron.*, vol. 39, no. 11, pp. 1559–1565, 1996.
- [50] K. Geib, J. Mahan, and C. Wilmsen, "W/SiC Contact Resistance at Elevated

- Temperatures,” in *Amorphous and Crystalline Silicon Carbide and Related Materials II*, M. M. Rahman, C. Y.-W. Wang, and G. L. Harris, Eds., Heidelberg: Springer-Verlag, 1989, pp. 224–228.
- [51] K. M. Geib, C. Wilson, R. G. Long, and C. W. Wilmsen, “Reaction between SiC and W, Mo, and Ta at elevated temperatures,” *J. Appl. Phys.*, vol. 68, no. 6, pp. 2796–2800, 1990.
 - [52] M. I. Chaudhry, W. B. Berry, and M. V. Zeller, “Ohmic Contacts on β -SiC,” *Mater. Res. Soc. Symp. Proc.*, vol. 162, pp. 507–512, 1990.
 - [53] L. Baud, C. Jaussaud, R. Madar, C. Bernard, S. Chen, and M.-A. Nicolet, “Interfacial reactions of W thin film on single-crystal (001) β -SiC,” *Mater. Sci. Eng. B*, vol. 29, pp. 126–130, 1995.
 - [54] N. Lundberg, C.-M. Zetterling, and M. Östling, “Temperature stability of cobalt Schottky contacts on n - and p -type 6H silicon carbide,” *Appl. Surf. Sci.*, vol. 73, pp. 316–321, Nov. 1993.
 - [55] A. Kakanakova-Georgieva, Ts. Marinova, O. Noblanc, C. Arnodo, S. Cassette, and C. Brylinski, “Characterization of ohmic and Schottky contacts on SiC,” *Thin Solid Films*, vol. 343–344, pp. 637–641, 1999.
 - [56] L. Baud, T. Billion, P. Lassagne, C. Jaussaud, and R. Madar, “Low contact resistivity W ohmic contacts to n -type 6H-SiC,” in *Inst. Physics Conference Series No. 142*, 1996, pp. 597–600.
 - [57] J. Kriz, T. Scholz, K. Gottfried, J. Leibelt, C. Kaufmann, and T. Gessner, “Metal Disilicide Contacts to 6H-SiC,” *Mater. Sci. Forum*, vol. 264–268, pp. 775–778, 1998.
 - [58] A. A. Iliadis, S. N. Andronescu, W. Yang, R. D. Vispute, A. Stanishevsky, J. H. Orloff, R. P. Sharma, T. Venkatesan, M. C. Wood, and K. A. Jones, “Pt and W Ohmic Contacts to p -6H-SiC by Focused Ion Beam Direct-Write Deposition,” *J. Electron. Mater.*, vol. 28, no. 3, pp. 136–140, Mar. 1999.
 - [59] F. Goesmann and R. Schmid-Fetzer, “Stability of W as electrical contact on 6H-SiC: phase relations and interface reactions in the ternary system W–Si–C,” *Mater. Sci. Eng. B*, vol. 34, no. 2–3, pp. 224–231, 1995.
 - [60] W. F. Seng and P. A. Barnes, “Calculations of tungsten silicide and carbide formation on SiC using the Gibbs free energy,” *Mater. Sci. Eng. B*, vol. 72, pp. 13–18, 2000.
 - [61] J. Rogowski and A. Kubiak, “Effects of annealing temperature on the structure and electrical properties of tungsten contacts to n -type silicon carbide,” *Mater. Sci. Eng. B*, vol. 191, pp. 57–65, 2015.
 - [62] I. P. Nikitina, K. V. Vassilevski, N. G. Wright, A. B. Horsfall, A. G. O’Neill, and C. M. Johnson, “Formation and role of graphite and nickel silicide in nickel based ohmic contacts to n -type silicon carbide,” *J. Appl. Phys.*, vol. 97, 083709, 2005.
 - [63] J. Crofton, P. G. McMullin, J. R. Williams, and M. J. Bozack, “High-temperature ohmic contact to n -type 6H-SiC using nickel,” *J. Appl. Phys.*, vol. 77, no. 3, pp. 1317–1319, 1995.
 - [64] B. Pécz, “Contact formation in SiC devices,” *Appl. Surf. Sci.*, vol. 184, pp. 287–294, 2001.
 - [65] Ts. Marinova, A. Kakanakova-Georgieva, V. Krastev, R. Kakanakov, M. Neshev,

- L. Kassamakova, O. Noblanc, C. Arnodo, S. Cassette, C. Brylinski, B. Pecz, G. Radnoczi, and Gy. Vincze, "Nickel based ohmic contacts on SiC," *Mater. Sci. Eng. B*, vol. 46, no. 1–3, pp. 223–226, Apr. 1997.
- [66] F. Roccaforte, F. La Via, and V. Raineri, "Ohmic contacts to SiC," *Int. J. High Speed Electron. Syst.*, vol. 15, no. 4, pp. 781–820, 2005.
- [67] S. Y. Han, K. H. Kim, J. K. Kim, H. W. Jang, K. H. Lee, N.-K. Kim, E. D. Kim, and J.-L. Lee, "Ohmic contact formation mechanism of Ni on *n*-type 4H-SiC," *Appl. Phys. Lett.*, vol. 79, no. 12, pp. 1816–1818, 2001.
- [68] A. Kuchuk, V. Kladko, M. Guzewicz, A. Piotrowska, R. Minikayev, A. Stonert, and R. Ratajczak, "Fabrication and characterization of nickel silicide ohmic contacts to *n*-type 4H silicon carbide," *J. Phys. Conf. Ser.*, vol. 100, no. 4, 042003, Mar. 2008.
- [69] S. Tanimoto, M. Miyabe, T. Shiiyama, T. Suzuki, H. Yamaguchi, S. Nakashima, and H. Okumura, "Toward a better understanding of Ni-based ohmic contacts on SiC," *Mater. Sci. Forum*, vol. 679–680, pp. 465–468, Mar. 2011.
- [70] M. Wzorek, A. Czerwinski, A. Kuchuk, J. Ratajczak, A. Piotrowska, and J. Kącki, "TEM Characterisation of Silicide Phase Formation in Ni-Based Ohmic Contacts to 4H *n*-SiC," *Mater. Trans.*, vol. 52, no. 3, pp. 315–318, 2011.
- [71] M. Wzorek, A. Czerwiński, A. V. Kuchuk, J. Ratajczak, A. Piotrowska, and J. Kącki, "Ni-based ohmic contacts to silicon carbide examined by electron microscopy," *Solid State Phenom.*, vol. 186, pp. 82–85, Mar. 2012.
- [72] A. Kuchuk, V. Kladko, Z. Adamus, M. Wzorek, M. Borysiewicz, P. Borowicz, A. Barcz, K. Gołaszewska, and A. Piotrowska, "Influence of Carbon Layer on the Properties of Ni-Based Ohmic Contact to *n*-Type 4H-SiC," *ISRN Electron.*, 271658, 2013.
- [73] T. Uemoto, "Reduction of Ohmic Contact Resistance on *n*-Type 6H-SiC by Heavy Doping," *Jpn. J. Appl. Phys.*, vol. 34, pp. L7–L9, 1995.
- [74] M. W. Cole, P. C. Joshi, C. Hubbard, J. D. Demaree, and M. Ervin, "Thermal stability and performance reliability of Pt/Ti/WSi/Ni ohmic contacts to *n*-SiC for high temperature and pulsed power device applications," *J. Appl. Phys.*, vol. 91, no. 6, pp. 3864–3868, 2002.
- [75] M. Li, A. C. Ahyi, X. Zhu, Z. Chen, T. Isaacs-Smith, J. R. Williams, and J. Crofton, "Nickel Ohmic Contacts to N-Implanted (0001) 4H-SiC," *J. Electron. Mater.*, vol. 39, no. 5, pp. 540–544, Mar. 2010.
- [76] C.-C. Dai, X.-C. Liu, T.-Y. Zhou, S.-Y. Zhuo, H.-K. Kong, J.-H. Yang, and E.-W. Shi, "Effect of annealing temperature on the contact properties of Ni/V/4H-SiC structure," *AIP Adv.*, vol. 4, no. 4, 047125, 2014.
- [77] M. Wzorek, A. Czerwinski, M. A. Borysiewicz, K. Gołaszewska, M. Myśliwiec, J. Ratajczak, A. Piotrowska, and J. Kącki, "Amorphous Ni-Zr layer applied for microstructure improvement of Ni-based ohmic contacts to SiC," *Mater. Sci. Eng. B*, vol. 199, pp. 42–47, 2015.
- [78] J. Crofton, P. A. Barnes, J. R. Williams, and J. A. Edmond, "Contact resistance measurements on *p*-type 6H-SiC," *Appl. Phys. Lett.*, vol. 62, no. 4, pp. 384–386, 1993.
- [79] J. Crofton, L. Beyer, J. R. Williams, E. D. Luckowski, S. E. Mohny, and J. M.

- DeLucca, "Titanium and aluminum-titanium ohmic contacts to p-type SiC," *Solid. State. Electron.*, vol. 41, no. 11, pp. 1725–1729, 1997.
- [80] J. Crofton, L. Beyer, T. Hogue, R. R. Siergiej, S. Mani, J. B. Casady, T. N. Oder, J. R. Williams, E. D. Luckowski, T. Isaacs-Smith, V. R. Iyer, and S. E. Mohny, "High temperature ohmic contacts to p-type SiC," *Trans. Fourth High Temp. Electron. Conf.*, pp. 84–87, 1998.
- [81] S. Tanimoto, N. Kiritani, M. Hoshi, and H. Okushi, "Ohmic Contact Structure and Fabrication Process Applicable to Practical SiC Devices," *Mater. Sci. Forum*, vol. 389–393, pp. 879–884, 2002.
- [82] J. Crofton, S. E. Mohny, J. R. Williams, and T. Isaacs-Smith, "Finding the optimum Al–Ti alloy composition for use as an ohmic contact to p-type SiC," *Solid. State. Electron.*, vol. 46, no. 1, pp. 109–113, Jan. 2002.
- [83] S. E. Mohny, B. A. Hull, J. Y. Lin, and J. Crofton, "Morphological study of the Al–Ti ohmic contact to p-type SiC," *Solid. State. Electron.*, vol. 46, no. 5, pp. 689–693, May 2002.
- [84] B. J. Johnson and M. A. Capano, "Mechanism of ohmic behavior of Al/Ti contacts to p-type 4H-SiC after annealing," *J. Appl. Phys.*, vol. 95, no. 10, pp. 5616–5620, 2004.
- [85] S. Tsukimoto, K. Nitta, T. Sakai, M. Moriyama, and M. Murakami, "Correlation between the electrical properties and the interfacial microstructures of TiAl-based ohmic contacts to p-type 4H-SiC," *J. Electron. Mater.*, vol. 33, no. 5, pp. 460–466, May 2004.
- [86] M. Gao, S. Tsukimoto, S. H. Goss, S. P. Tumakha, T. Onishi, M. Murakami, and L. J. Brillson, "Role of Interface Layers and Localized States in TiAl-Based Ohmic Contacts to p-Type 4H-SiC," *J. Electron. Mater.*, vol. 36, no. 4, pp. 277–284, Feb. 2007.
- [87] Z. Wang, S. Tsukimoto, M. Saito, K. Ito, M. Murakami, and Y. Ikuhara, "Ohmic contacts on silicon carbide: The first monolayer and its electronic effect," *Phys. Rev. B*, vol. 80, no. 24, 245303, Dec. 2009.
- [88] K. Buchholt, R. Ghandi, M. Domeij, C.-M. Zetterling, J. Lu, P. Eklund, L. Hultman, and A. Lloyd Spetz, "Ohmic contact properties of magnetron sputtered Ti_3SiC_2 on n- and p-type 4H-silicon carbide," *Appl. Phys. Lett.*, vol. 98, no. 4, 042108, 2011.
- [89] T. Abi-Tannous, M. Soueidan, G. Ferro, M. Lazar, B. Toury, M. F. Beaufort, J. F. Barbot, J. Penuelas, and D. Planson, "Parametric investigation of the formation of epitaxial Ti_3SiC_2 on 4H-SiC from Al-Ti annealing," *Appl. Surf. Sci.*, vol. 347, pp. 186–192, 2015.
- [90] H. Fashandi, M. Andersson, J. Eriksson, J. Lu, K. Smedfors, C.-M. Zetterling, A. Lloyd Spetz, and P. Eklund, "Single-step synthesis process of Ti_3SiC_2 ohmic contacts on 4H-SiC by sputter-deposition of Ti," *Scr. Mater.*, vol. 99, pp. 53–56, 2015.
- [91] R. Pérez, N. Mestres, D. Tournier, P. Godignon, and J. Millán, "Ni/Ti ohmic and Schottky contacts on 4H-SiC formed with a single thermal treatment," *Diam. Relat. Mater.*, vol. 14, no. 3–7, pp. 1146–1149, Mar. 2005.
- [92] B. Krishnan, S. P. Kotamraju, G. Melnychuk, H. Das, J. N. Merrett, and Y.

- Koshka, "Heavily Aluminum-Doped Epitaxial Layers for Ohmic Contact Formation to *p*-Type 4H-SiC Produced by Low-Temperature Homoepitaxial Growth," *J. Electron. Mater.*, vol. 39, no. 1, pp. 34–38, Oct. 2009.
- [93] J. H. Park and P. H. Holloway, "Effects of nickel and titanium thickness on nickel/titanium ohmic contacts to *n*-type silicon carbide," *J. Vac. Sci. Technol. B Microelectron. Nanom. Struct.*, vol. 23, no. 2, pp. 486–494, 2005.
- [94] I. P. Nikitina, K. V. Vassilevski, A. B. Horsfall, N. G. Wright, A. G. O'Neill, C. M. Johnson, T. Yamamoto, and R. K. Malhan, "Structural pattern formation in titanium–nickel contacts on silicon carbide following high-temperature annealing," *Semicond. Sci. Technol.*, vol. 21, no. 7, pp. 898–905, Jul. 2006.
- [95] K. V. Vassilevski, I. P. Nikitina, A. B. Horsfall, N. G. Wright, C. M. Johnson, R. K. Malhan, and T. Yamamoto, "Structural properties of titanium-nickel films on silicon carbide following high temperature annealing," *Mater. Sci. Forum*, vol. 527–529, pp. 871–874, 2006.
- [96] P. Macháč, B. Barda, and J. Maixner, "Structural characterization of nickel–titanium film on silicon carbide," *Appl. Surf. Sci.*, vol. 254, no. 6, pp. 1691–1693, Jan. 2008.
- [97] B. Barda, P. Macháč, M. Hubičková, and J. Náhlík, "Comparison of Ni/Ti and Ni ohmic contacts on *n*-type 6H–SiC," *J. Mater. Sci.: Mater. Electron.*, vol. 19, no. 11, pp. 1039–1044, 2007.
- [98] M. Siad, C. Pineda Vargas, M. Nkosi, D. Saidi, N. Souami, N. Daas, and A. C. Chami, "Characterisation of Ni and Ni/Ti contact on *n*-type 4H–SiC," *Appl. Surf. Sci.*, vol. 256, no. 1, pp. 256–260, Oct. 2009.
- [99] P. Macháč, B. Barda, and M. Kudrnová, "Role of titanium in Ti/Ni ohmic contact on *n*-type 6H–SiC," *Microelectron. Eng.*, vol. 87, no. 3, pp. 274–277, Mar. 2010.
- [100] F. Laariedh, M. Lazar, P. Cremillieu, J. Penuelas, J.-L. Leclercq, and D. Planson, "The role of nickel and titanium in the formation of ohmic contacts on *p*-type 4H–SiC," *Semicond. Sci. Technol.*, vol. 28, 045007, Apr. 2013.
- [101] N. Thierry-Jebali, A. Vo-Ha, D. Carole, M. Lazar, G. Ferro, D. Planson, A. Henry, and P. Brosselard, "Very low specific contact resistance measurements made on a highly *p*-type doped 4H–SiC layer selectively grown by vapor-liquid-solid transport," *Appl. Phys. Lett.*, vol. 102, no. 21, 212108, 2013.
- [102] H. Yu, X. Zhang, H. Shen, Y. Tang, Y. Bai, Y. Wu, K. Liu, and X. Liu, "Thermal stability of Ni/Ti/Al ohmic contacts to *p*-type 4H–SiC," *J. Appl. Phys.*, vol. 117, no. 2, 025703, 2015.
- [103] L. Fursin, J. Zhao, and M. Weiner, "Nickel ohmic contacts to *p*- and *n*-type 4H–SiC," *Electron. Lett.*, vol. 37, no. 77, pp. 1092–1093, 2001.
- [104] R. N. Hall, "Electrical Contacts to Silicon Carbide," *J. Appl. Phys.*, vol. 29, no. 6, pp. 914–917, 1958.
- [105] J. S. Shier, "Ohmic Contacts to Silicon Carbide," *J. Appl. Phys.*, vol. 41, no. 2, pp. 771–773, 1970.
- [106] S.-K. Lee, C.-M. Zetterling, M. Östling, J.-P. Palmquist, H. Hogberg, and U. Jansson, "Low resistivity ohmic titanium carbide contacts to *n*- and *p*-type 4H-silicon carbide," *Solid. State. Electron.*, vol. 44, pp. 1179–1186, 2000.
- [107] S.-K. Lee, C.-M. Zetterling, M. Östling, J.-P. Palmquist, and U. Jansson, "Low

- resistivity ohmic contacts on 4H-silicon carbide for high power and high temperature device applications,” *Microelectron. Eng.*, vol. 60, pp. 261–268, 2002.
- [108] S. Tsukimoto, T. Sakai, T. Onishi, K. Ito, and M. Murakami, “Simultaneous formation of *p*- and *n*-type ohmic contacts to 4H-SiC using the ternary Ni/Ti/Al system,” *J. Electron. Mater.*, vol. 34, no. 10, pp. 1310–1312, Oct. 2005.
 - [109] H. Guo, Y. Zhang, and Y. Zhang, “Ti–Al based ohmic contacts to *n*-type 6H-SiC with P⁺ ion implantation,” *Chinese Phys.*, vol. 15, no. 9, pp. 2142–2145, 2006.
 - [110] J. Crofton, J. R. Williams, A. V. Adediji, J. D. Scofield, S. Dhar, L. C. Feldman, and M. J. Bozack, “Ohmic Contacts to *p*-Type Epitaxial and Implanted 4H-SiC,” *Mater. Sci. Forum*, vol. 527–529, pp. 895–898, 2006.
 - [111] K. Ito, T. Onishi, H. Takeda, K. Kohama, S. Tsukimoto, M. Konno, Y. Suzuki, and M. Murakami, “Simultaneous Formation of Ni/Al Ohmic Contacts to Both *n*- and *p*-Type 4H-SiC,” *J. Electron. Mater.*, vol. 37, no. 11, pp. 1674–1680, Aug. 2008.
 - [112] K. Ito, H. Takeda, Y. Shirai, and M. Murakami, “Effects of Reducing Annealing Temperature on Ni/Al Ohmic Contacts to *n*- and *p*-Type 4H-SiC,” *Trans. JWRI*, vol. 41, no. 2, pp. 33–38, 2012.
 - [113] R. Okojie, L. Evans, D. Lukco, and J. P. Morris, “A Novel Tungsten–Nickel Alloy Ohmic Contact to SiC at 900 °C,” *IEEE Electron Device Lett.*, vol. 31, no. 8, pp. 791–793, 2010.
 - [114] H. Tamaso, S. Yamada, H. Kitabayashi, and T. Horii, “Ti/Al/Si Ohmic Contacts for Both *n*-Type and *p*-Type 4H-SiC,” *Mater. Sci. Forum*, vol. 778–780, pp. 669–672, 2014.
 - [115] S.-J. Joo, S. Baek, S.-C. Kim, and J.-S. Lee, “Simultaneous Formation of Ohmic Contacts on *p*⁺- and *n*⁺-4H-SiC Using a Ti/Ni Bilayer,” *J. Electron. Mater.*, vol. 42, no. 10, pp. 2897–2904, Jul. 2013.
 - [116] M. Vivona, G. Greco, F. Giannazzo, R. Lo Nigro, S. Rascunà, M. Saggio, and F. Roccaforte, “Thermal stability of the current transport mechanisms in Ni-based Ohmic contacts on *n*- and *p*-implanted 4H-SiC,” *Semicond. Sci. Technol.*, vol. 29, no. 7, 075018, 2014.
 - [117] X. Zhang, Y. Tang, H. Shen, Y. Bai, R. Huo, W. Wang, and S. Liu, “Study on simultaneous formation of ohmic contacts on *p*- and *n*-type 4H-SiC using Ni/Ti/Al Ternary System,” *2014 12th IEEE Inter. Conf. Solid-State Integr. Circuit Technol. (Guilin, China)*, 7021382, 2014.
 - [118] M. F. Zhu, I. Suni, M.-A. Nicolet, and T. Sands, “Reaction of amorphous Ni-W and Ni-N-W films with substrate silicon,” *J. Appl. Phys.*, vol. 56, no. 10, pp. 2740–2745, 1984.
 - [119] C. S. Pai, S. S. Lau, D. B. Poker, and L. S. Hung, “A comparison between thermal annealing and ion mixing of alloyed Ni-W films on Si. I,” *J. Appl. Phys.*, vol. 58, no. 11, pp. 4172–4177, 1985.
 - [120] C. S. Pai, S. S. Lau, D. B. Poker, and L. S. Hung, “A comparison between thermal annealing and ion mixing of multilayered Ni-W films on Si. II,” *J. Appl. Phys.*, vol. 58, no. 11, pp. 4178–4185, 1985.
 - [121] S. Liu, K. Reinhardt, C. Severt, and J. D. Scofield, “Thermally stable ohmic contacts on *n*-type 6H- and 4H-SiC based on silicide and carbide,” in *Inst. Physics Conference Series No. 142*, 1996, pp. 589–592.

- [122] S. Z. Liu and J. D. Scofield, "Ohmic Contacts to *p*-Type SiC with Improved Thermal Stability," *Mater. Sci. Forum*, vol. 264–268, pp. 791–794, 1998.
- [123] S. Liu, G. Potts, and J. D. Scofield, "Thermal Stability in Vacuum and in Air of Al/Ni/W Based Ohmic Contacts to *p*-Type SiC," *Mater. Sci. Forum*, vol. 338–342, pp. 1021–1024, 2000.
- [124] B. H. Tsao, S. Liu, and J. D. Scofield, "Improved AlNi Ohmic Contacts to *p*-Type SiC," *Mater. Sci. Forum*, vol. 457–460, pp. 841–844, 2004.
- [125] B. H. Tsao, J. Lawson, and J. D. Scofield, "Ti/AlNi/W and Ti/Ni₂Si/W Ohmic Contacts to *p*-Type SiC," *Mater. Sci. Forum*, vol. 527–529, pp. 903–906, 2006.
- [126] S. Adams, C. Severt, J. Leonard, S. Liu, and S. R. Smith, "Ohmic contacts to 6H-SiC Semiconductors," in *Transactions Second International High Temperature Electronics Conference (Charlotte, North Carolina)*, 1994, pp. XIII–9–14.
- [127] S. Liu, K. Reinhardt, C. Severt, J. Scofield, M. Ramalingam, and C. Tunstall, "Long-Term Thermal Stability of Ni/Cr/W Ohmic Contacts on *n*-Type SiC," in *Transactions Third International High Temperature Electronics Conference (HiTEC) (Albuquerque, New Mexico)*, 1996, pp. VII–9–13.
- [128] N. Bochvar and L. Rokhlin, "Carbon–Nickel–Tungsten," in *Volume 11 Ternary Alloy Systems: Phase Diagrams, Crystallographic and Thermodynamic Data, Subvolume E "Refractory Metal Systems", of Landolt-Börnstein - Group IV Physical Chemistry*, G. Effenberg and S. Ilyenko, Eds., SpringerMaterials, 2010, pp. 579–594.
- [129] S. V. Nagender Naidu, A. M. Sriramamurthy, and P. Rama Rao, "Ni-W (Nickel-Tungsten)," in *Phase Diagrams of Binary Nickel Alloys*, P. Nash, Ed., ASM International, 1991, pp. 367–373.
- [130] ASM Alloy Phase Diagram Database, "Diagram No. 101181, Data from Turchi P.E.A., Kaufman L., Liu Z.K.; Modelling of Ni-Cr-Mo based alloys: part I - phase stability, Calphad, Vol. 30, 2006, pp. 70-87," 2007.
- [131] D. Vujic, S. Whang, and S. Cytron, "Microstructure of Rapidly Solidified W–Ni Alloys," *Mater. Res. Soc. Symp. Proc.*, vol. 80, pp. 307–315, 1987.
- [132] N. S. Mishra and S. Ranganathan, "Electron microscopy and diffraction of ordering in Ni–W alloys," *Acta Metall. Mater.*, vol. 43, no. 6, pp. 2287–2302, Jun. 1995.
- [133] A. J. Detor and C. A. Schuh, "Microstructural evolution during the heat treatment of nanocrystalline alloys," *J. Mater. Res.*, vol. 22, no. 11, pp. 3233–3248, Jan. 2007.
- [134] R. Cury, J.-M. Joubert, S. Tusseau-Nenez, E. Leroy, and A. Allavena-Valette, "On the existence and the crystal structure of Ni₄W, NiW and NiW₂ compounds," *Intermetallics*, vol. 17, no. 3, pp. 174–178, Mar. 2009.
- [135] J. Lee, C. R. Lear, X. Zhang, P. Bellon, and R. S. Averback, "Irradiation-Induced Nanoprecipitation in Ni-W Alloys," *Metall. Mater. Trans. A*, vol. 46A, pp. 1046–1061, 2015.
- [136] C. J. Marvel, P. R. Cantwell, and M. P. Harmer, "The critical influence of carbon on the thermal stability of nanocrystalline Ni–W alloys," *Scr. Mater.*, vol. 96, pp. 45–48, 2015.
- [137] K. Whitehead and L. Brownlee, "Ternäre Phasen im System Nickel-Wolfram-

- Kohlenstoff,” *Planseeberichte für Pulvermetallurgie*, vol. 4, no. 3, pp. 62–71, 1956.
- [138] ASM Alloy Phase Diagram Database, “Diagram No. 207660, Data from English J.J., Tungsten-Nickel system, Binary and Ternary Phase Diagrams of Cb, Mo, Ta, and W, J.J. English, DMIC Rep., Vol. , 1961, pp. 86,” 2007.
- [139] P. Ettmayer and R. Suchentrunk, “Über die thermische Stabilität der Eta-Carbide,” *Monatshefte für Chemie*, vol. 101, no. 4, pp. 1098–1103, 1970.
- [140] M. Fiedler and H. H. Stadelmaier, “The Ternary System Nickel-Tungsten-Carbon,” *Z. Metallkde*, vol. 66, pp. 402–404, 1975.
- [141] O. Knotek, P. Lohage, and H. Reimann, “Nickel-based wear-resistant coatings by vacuum melting,” *Thin Solid Films*, vol. 108, pp. 449–458, 1983.
- [142] Y. Du and J. C. Schuster, “Experimental Investigations and Thermodynamic Descriptions of the Ni-Si and C-Ni-Si Systems,” *Metall. Mater. Trans. A*, vol. 30, no. 9, pp. 2409–2418, 1999.
- [143] M. Naka, T. Fukai, and J. C. Schuster, “Interface structures and diffusion paths in SiC/metal couples,” in *Interfaces, and the Science of Ceramic Joining: Proc. 106th Annual Meeting of the American Ceramic Society (Indianapolis, Indiana, USA 2004) (Ceramic Transactions vol 158)*, K. S. Weill, I. E. Reimanis, and C. A. Lewinsohn, Eds., American Ceramic Society, 2005, pp. 19–27.
- [144] M.-A. Nicolet, “Diffusion barriers in thin films,” *Thin Solid Films*, vol. 52, pp. 415–443, 1978.
- [145] Z. Wang, W. Liu, and C. Wang, “Recent Progress in Ohmic Contacts to Silicon Carbide for High-Temperature Applications,” *J. Electron. Mater.*, vol. 45, no. 1, pp. 267–284, 2016.
- [146] D. J. Spry and D. Lukco, “A Bondable Metallization Stack That Prevents Diffusion of Oxygen and Gold into Monolithically Integrated Circuits Operating Above 500 °C,” *J. Electron. Mater.*, vol. 41, no. 5, pp. 915–920, 2012.
- [147] S. Tanimoto and H. Oohashi, “High-Temperature Reliable Ni₂Si-based Contacts on SiC Connected to Si-Doped Al Interconnect via Ta/TaN Barrier,” *Mater. Sci. Forum*, vol. 617, pp. 561–564, 2009.
- [148] S. Liu, Z. He, L. Zheng, B. Liu, F. Zhang, L. Dong, L. Tian, Z. Shen, J. Wang, Y. Huang, Z. Fan, X. Liu, G. Yan, W. Zhao, L. Wang, G. Sun, F. Yang, and Y. Zeng, “The thermal stability study and improvement of 4H-SiC ohmic contact,” *Appl. Phys. Lett.*, vol. 105, no. 12, 122106, 2014.
- [149] T. Jang, B. Odekirk, L. D. Madsen, and L. M. Porter, “Thermal stability and contact degradation mechanisms of TaC ohmic contacts with W/WC overlayers to *n*-type 6H SiC,” *J. Appl. Phys.*, vol. 90, no. 9, pp. 4555–4559, 2001.
- [150] R. S. Okojie, D. J. Spry, J. Krotine, C. Salupo, and D. R. Wheeler, “Stable Ti/TaSi₂/Pt Ohmic Contacts on *n*-Type 6H-SiC Epilayer at 600 °C in Air,” *Mater. Res. Soc. Symp. Proc.*, vol. 622, no. 216, pp. T8.3.1–T8.3.7, 2000.
- [151] A. Baeri, V. Raineri, F. La Via, V. Puglisi, and G. G. Condorelli, “Environment influence on Ti diffusion and layer degradation of a SiC/Ni₂Si/TiW/Au contact structure,” *J. Vac. Sci. Technol. B Microelectron. Nanom. Struct.*, vol. 22, no. 3, pp. 966–970, 2004.
- [152] M.-A. Nicolet and M. Bartur, “Diffusion barriers in layered contact structures,” *J.*

- Vac. Sci. Technol.*, vol. 19, no. 3, pp. 786–793, 1981.
- [153] R. Kakanakov, L. Kasamakova-Kolaklieva, N. Hristeva, G. Lepoweveva, J. B. Gomes, I. Avramova, and Ts. Marinova, “High temperature and high power stability investigation of Al-based ohmic contacts to *p*-type 4H-SiC,” *IEEE 27th Int’l Spring Semin. Electron. Technol.*, pp. 543–546, 2004.
 - [154] J.-H. Gao, K. Sagisaka, M. Kitahara, M.-S. Xu, S. Miyamoto, and D. Fujita, “Graphene growth on a Pt(111) substrate by surface segregation and precipitation,” *Nanotechnology*, vol. 23, no. 5, 055704, 2012.
 - [155] B.-J. Lee and G.-H. Jeong, “Comparative study on graphene growth mechanism using Ni films, Ni/Mo sheets, and Pt substrates,” *Appl. Phys. A*, vol. 116, no. 1, pp. 15–24, 2014.
 - [156] B. J. Kang, J. H. Mun, C. Y. Hwang, and B. J. Cho, “Monolayer graphene growth on sputtered thin film platinum,” *J. Appl. Phys.*, vol. 106, no. 10, 104309, 2009.
 - [157] M. Xu, D. Fujita, J. Gao, and N. Hanagata, “Auger Electron Spectroscopy: A Rational Method for Determining Thickness of Graphene Films,” *ACS Nano*, vol. 4, no. 5, pp. 2937–2945, 2010.
 - [158] K. Frisk, L. Dumitrescu, M. Ekroth, B. Jansson, O. Kruse, and B. Sundman, “Development of a Database for Cemented Carbides: Thermodynamic Modeling and Experiments,” *J. Phase Equilibria*, vol. 22, no. 6, pp. 645–655, 2001.
 - [159] M. Sumiya and S. Fuke, “Review of polarity determination and control of GaN,” *MRS Internet J. Nitride Semicond. Res.*, vol. 9, pp. 1–34, 2004.
 - [160] A. J. Van Bommel, J. E. Crombeen, and A. Van Tooren, “LEED and Auger electron observations of the SiC (0001) surface,” *Surf. Sci.*, vol. 48, pp. 463–472, 1975.
 - [161] C. S. Gallinat, G. Koblmüller, J. S. Brown, S. Bernardis, J. S. Speck, G. D. Chern, E. D. Readinger, H. Shen, and M. Wraback, “In-polar InN grown by plasma-assisted molecular beam epitaxy,” *Appl. Phys. Lett.*, vol. 89, no. 3, 032109, 2006.
 - [162] G. Koblmüller, C. S. Gallinat, S. Bernardis, J. S. Speck, G. D. Chern, E. D. Readinger, H. Shen, and M. Wraback, “Optimization of the surface and structural quality of N-face InN grown by molecular beam epitaxy,” *Appl. Phys. Lett.*, vol. 89, no. 7, 071902, 2006.
 - [163] A. Jain, X. Weng, S. Raghavan, B. L. VanMil, T. Myers, and J. M. Redwing, “Effect of polarity on the growth of InN films by metalorganic chemical vapor deposition,” *J. Appl. Phys.*, vol. 104, no. 5, 053112, 2008.
 - [164] K. Fukuda, S. Suzuki, J. Senzaki, W. J. Cho, T. Tanaka, and K. Arai, “Interface Properties of MOS Structures Formed on 4H-SiC C(000 $\bar{1}$) Face,” *Mater. Sci. Forum*, vol. 353–356, pp. 631–634, 2001.
 - [165] K. Fukuda, M. Kato, J. Senzaki, K. Kojima, and T. Suzuki, “4H-SiC MOSFETs on C(000 $\bar{1}$) Face with Inversion Channel Mobility of 127cm²/Vs,” *Mater. Sci. Forum*, vol. 457–460, pp. 1417–1420, 2004.
 - [166] R. Singh, “Reliability and performance limitations in SiC power devices,” *Microelectron. Reliab.*, vol. 46, no. 5–6, pp. 713–730, May 2006.
 - [167] K. Fukuda, J. Senzaki, K. Kojima, and T. Suzuki, “High Inversion Channel Mobility of MOSFET Fabricated on 4H-SiC C(000 $\bar{1}$) Face Using H₂ Post-Oxidation Annealing,” *Mater. Sci. Forum*, vol. 433–436, pp. 567–570, 2003.

- [168] S. Harada, M. Kato, K. Suzuki, M. Okamoto, T. Yatsuo, K. Fukuda, and K. Arai, "1.8 mΩcm², 10 A Power MOSFET in 4H-SiC," *Tech. Dig. Int. Electron Devices Meet. 2006*, pp. 1–4, 2006.
- [169] M. Okamoto, M. Iijima, T. Yatsuo, T. Nagano, K. Fukuda, and H. Okumura, "Fabrication of p-Channel MOSFETs on 4H-SiC C-Face," *Mater. Sci. Forum*, vol. 679–680, pp. 653–656, 2011.
- [170] M. Okamoto, Y. Makifuchi, M. Iijima, Y. Sakai, N. Iwamuro, H. Kimura, K. Fukuda, and H. Okumura, "Coexistence of Small Threshold Voltage Instability and High Channel Mobility in 4H-SiC(000 $\bar{1}$) Metal–Oxide–Semiconductor Field-Effect Transistors," *Appl. Phys. Express*, vol. 5, 041302, Apr. 2012.
- [171] T. Umeda, M. Okamoto, R. Kosugi, S. Harada, R. Arai, Y. Sato, T. Makino, and T. Ohshima, "SiC MOS Interface States: Difference Between Si Face and C Face," *ECS Trans.*, vol. 58, no. 7, pp. 55–60, 2013.
- [172] K.-Y. Lee, Y.-H. Chang, Y.-H. Huang, S.-D. Wu, C. Y. Chung, C.-F. Huang, and T.-C. Lee, "Influence of low temperature oxidation and nitrogen passivation on the MOS interface of C-face 4H-SiC," *Appl. Surf. Sci.*, vol. 282, pp. 126–132, Oct. 2013.
- [173] D. Li, M. Sumiya, S. Fuke, D. Yang, D. Que, Y. Suzuki, and Y. Fukuda, "Selective etching of GaN polar surface in potassium hydroxide solution studied by x-ray photoelectron spectroscopy," *J. Appl. Phys.*, vol. 90, no. 8, pp. 4219–4223, 2001.
- [174] P. Visconti, D. Huang, M. A. Reshchikov, F. Yun, R. Cingolani, D. J. Smith, J. Jasinski, W. Swider, Z. Liliental-Weber, and H. Morkoç, "Investigation of defects and surface polarity in GaN using hot wet etching together with microscopy and diffraction techniques," *Mater. Sci. Eng. B Solid-State Mater. Adv. Technol.*, vol. 93, no. 1–3, pp. 229–233, 2002.
- [175] T. Zywiets, J. Neugebauer, and M. Scheffler, "Adatom diffusion at GaN (0001) and (000 $\bar{1}$) surfaces," *Appl. Phys. Lett.*, vol. 73, no. 4, pp. 487–489, 1998.
- [176] Y. L. Wang, B. H. Chu, C. Y. Chang, K. H. Chen, Y. Zhang, Q. Sun, J. Han, S. J. Pearton, and F. Ren, "Hydrogen sensing of N-polar and Ga-polar GaN Schottky diodes," *Sensors and Actuators B-Chemical*, vol. 142, no. 1, pp. 175–178, 2009.
- [177] J. R. Waldrop, R. W. Grant, Y. C. Wang, and R. F. Davis, "Metal Schottky barrier contacts to alpha 6H-SiC," *J. Appl. Phys.*, vol. 72, no. 10, pp. 4757–4760, 1992.
- [178] J. R. Waldrop and R. W. Grant, "Schottky contacts barrier height and interface chemistry of annealed to alpha 6H-SiC : Crystal face dependence metal," *Appl. Phys. Lett.*, vol. 62, no. 21, pp. 2685–2687, 1993.
- [179] B. Veisz and B. Pécz, "Polarity dependent Al–Ti contacts to 6H-SiC," *Appl. Surf. Sci.*, vol. 233, pp. 360–365, 2004.
- [180] W. Lu, W. C. Mitchel, G. R. Landis, T. R. Crenshaw, and W. E. Collins, "Catalytic graphitization and Ohmic contact formation on 4H-SiC," *J. Appl. Phys.*, vol. 93, no. 9, pp. 5397–5403, 2003.
- [181] R. Ghandi, H.-S. Lee, M. Domeij, C.-M. Zetterling, and M. Östling, "Backside Nickel Based Ohmic Contacts to n-type Silicon Carbide," *Mater. Sci. Forum*, vol. 600–603, pp. 635–638, 2009.
- [182] U. Karrer, O. Ambacher, and M. Stutzmann, "Influence of crystal polarity on the

- properties of Pt/GaN Schottky diodes,” *Appl. Phys. Lett.*, vol. 77, no. 13, pp. 2012–2014, 2000.
- [183] S. Dasgupta, Nidhi, D. F. Brown, F. Wu, S. Keller, J. S. Speck, and U. K. Mishra, “Ultralow nonalloyed Ohmic contact resistance to self aligned N-polar GaN high electron mobility transistors by In(Ga)N regrowth,” *Appl. Phys. Lett.*, vol. 96, 143504, 2010.
 - [184] A. Eisenhardt, S. Krischok, and M. Himmerlich, “Surface states and electronic structure of polar and nonpolar InN – An in situ photoelectron spectroscopy study,” *Appl. Phys. Lett.*, vol. 102, no. 23, 231602, 2013.
 - [185] J. J. Glickstein, “Investigation of Metal Contacts to Group III-Nitride Semiconductors,” Undergraduate Thesis, The Pennsylvania State University, 2012.
 - [186] H. H. Stadelmaier and A. C. Fraker, “Stickstofflegierungen der T-Metalle Mangan, Eisen, Kobalt und Nickel mit Gallium, Germanium, Indium und Zinn,” *Z. Metallkde*, vol. 53, pp. 48–52, 1962.
 - [187] H. H. Stadelmaier and T. S. Yun, “Stickstofflegierungen der T-Metalle Mangan, Eisen, Kobalt und Nickel mit Magnesium, Aluminium, Zink und Kadmium,” *Z. Metallkde*, vol. 52, pp. 477–480, 1961.
 - [188] B. Onderka, J. Unland, and R. Schmid-Fetzer, “Thermodynamics and phase stability in the In–N system,” *J. Mater. Res.*, vol. 17, no. 12, pp. 3065–3083, 2002.

VITA

Katherine Cora Kragh-Buetow

Education

Ph.D. in Materials Science and Engineering

The Pennsylvania State University, University Park, PA

Dissertation: “Robust Electrical Contacts for Sensors and Electronics in Space Flight”

Defense: December 18, 2015

B.S. in Engineering Physics (2010), *summa cum laude*

Rose-Hulman Institute of Technology, Terre Haute, IN

Minors: Electrical Engineering, Chemistry, and Astronomy; Semiconductors Certificate

Fellowships

NASA Space Technology Research Fellowship, Inaugural Class (2011–2015)

3M Graduate Fellowship in Materials Science and Engineering (2010–2013)

University Graduate Fellowship (2010–2011)

Selected Publications

K. C. Kragh-Buetow, R. S. Okojie, D. Lukco, S. E. Mohny, “Characterization of Tungsten-Nickel Simultaneous Ohmic Contacts to *p*- and *n*-type 4H-SiC,” *Semicond. Sci. Technol.*, Volume 30, 105019 (2015) DOI: 10.1088/0268-1242/30/10/105019

A. S. Raghavan, T. A. Palmer, K. C. Kragh-Buetow, A. C. Domask, E. W. Reutzel, S. E. Mohny, T. DebRoy, “Employing microsecond pulses to form laser-fired contacts in photovoltaic devices,” *Prog. Photovoltaics: Res. Appl.* (2014) DOI: 10.1002/pip.2523

K. C. Kragh-Buetow, X. Weng, E. D. Readinger, M. Wraback, S. E. Mohny, “Effects of polarity on Ni/InN interfacial reactions,” *Appl. Phys. Lett.*, Volume 102, 021607 (2013) DOI: 10.1063/1.4781768

Awards

Electronic Materials Conference NIST Uncertainty Analysis Award 2015

Coppola Graduate Student Excellence Award for Student Service and Leadership 2015

Penn State Materials Visualization Competition, 1st place Visual Category 2015

Penn State Materials Science and Engineering Safety Award 2014

Rodney Erickson Outstanding Dedication to Penn State Award 2014